THE UNIVERSITY OF CHICAGO

CLIMATE DYNAMICS OF CONDENSIBLE-RICH ATMOSPHERES

A DISSERTATION SUBMITTED TO
THE FACULTY OF THE DIVISION OF THE PHYSICAL SCIENCES
IN CANDIDACY FOR THE DEGREE OF
DOCTOR OF PHILOSOPHY

DEPARTMENT OF THE GEOPHYSICAL SCIENCES

BY
FENG DING

CHICAGO, ILLINOIS
AUGUST 2017

TABLE OF CONTENTS

LIST OF FIGURES

LIST OF TABLES

ACKNOWLEDGMENTS

First, I would like to thank my advisor, Raymond Pierrehumbert, for his great generosity, patience and enthusiasm. Ray has always been a great source of inspiration.

I would also like to thank my committee members for their advice and suggestions, especially during the last few years after Ray moved to Oxford. Particularly I thank Dorian Abbot and Noboru Nakamura for taking care of my administrative affairs in these years.

I thank my co-students from whom I learnt a great deal, especially Daniel Koll for the fruitful discussions over the years when he shared the office with me.

Much of this work required significant computer resources. I thank the Research Computing Center at the University of Chicago for providing me with the computation time on the Midway cluster, and Richard Dahringer for helping me run climate models on the cluster when he was the system administrator in the Department of Geophysical Sciences.

Support for this work was provided by the NASA Astrobiology Institutes Virtual Planetary Laboratory Lead Team, under the National Aeronautics and Space Administration solicitation NNH12ZDA002C and Cooperative Agreement Number NNA13AA93A. This support is greatly acknowledged.

Finally, I would like to thank my family and friends for all their support and encouragement.

ABSTRACT

We present simulations of the climate dynamics of condensible-rich atmospheres using a hierarchy of planetary climate models. A key different feature in our model compared to other models studying the moist climates is that we especially develop a simple parameterization of moist convection valid in the nondilute as well as dilute limits. The new convection scheme is used to discuss the basic character of nondilute convection. The energy conservation properties of the scheme are discussed in detail, and are verified in one-dimensional radiative-convective simulations. As a further illustration of the behavior of the scheme, results for a runaway greenhouse atmosphere for seasonally varying instellation corresponding to a highly eccentric orbit are presented. This case illustrates that the high thermal inertia associated with latent heat in nondilute atmospheres can damp out the effects of even extreme seasonal forcing.

We then develop a 3D idealized general circulation model that incorporates the 1D single column model, and use it to study condensible-rich atmospheres. We find that nondilute atmospheres have weak horizontal temperature gradients even for rapidly rotating planets, and that their circulations are largely barotropic. The relative humidity of the condensible component tends towards 100% as the atmosphere becomes more nondilute, which has important implications for runaway greenhouse thresholds.

We then shift our focus to condensible-rich atmospheres on slowly and synchronously rotating planets, because the atmospheres on such terrestrial exoplanets would be characterized by near-future telescopes, and fruitful observation results are expected to come out in the coming decade. We first study the moist climate governed by an overturning circulation with a weak cold trap. The simulation suggests high-level cloud formation near the substellar region and build up of condensible substance on the nightside. We next use a one-dimensional energy budget model to study the more strongly nondilute atmosphere governed by low-level evaporation-driven flow, and derive a non-dimensional parameter that determines whether the atmosphere is global or local. We discuss the possibility to discriminate the circulation regimes of condensible-rich atmospheres by using the broadband phase curve. Our finding will facilitate characterizing condensible atmospheres on tidally locked terrestrial exoplanets in the near future, including the habitable worlds when the condensible substance is water vapor.

CHAPTER 1

INTRODUCTION

1.1 Motivation

Condensible substances are ubiquitous in planetary atmospheres. The most familiar case is water vapor in Earth's present climate. This condensible gas is dilute in Earth's atmosphere, in the sense that its concentration is everywhere small relative to the background non-condensible gases. However, a wide variety of important planetary climate problems involve condensible-rich atmospheres with non-dilute condensible substances. These include but are not limited to the topic on planetary habitability such as characterizing both the inner and outer edge of the habitable zone and the abiotic oxygen build-up in water-rich atmospheres. Besides, a great deal of fertile new territory for geophysical fluid dynamics (GFD) is opened up when the fluid flow is coupled to the novel thermodynamics in condensible-rich atmospheres. Therefore studying the climate dynamics of condensible-rich atmospheres brings new opportunity for understanding the condensible planetary atmospheres and also gives a new insight to our understanding of basic GFD.

1.2 Planetary Climate Problems Related to Condensible-Rich Atmospheres

Most planetary atmospheres contain one or more condensible substances, which can undergo phase transitions from vapor to liquid or solid form within the atmosphere. The most familiar condensible is water vapor, which plays a key role in Earth's climate, and in the runaway water vapor greenhouse which is central to the past climate evolution of Venus and also determines the inner edge of the habitable zone (Ingersoll, 1969; Kasting, 1988; Nakajima et al., 1992; Kasting et al., 1993; Kopparapu et al., 2013). CO_2 condensation is of importance on both present and Early Mars, and plays a similar role to water vapor in determining the outer edge of the habitable zone (Pierrehumbert, 2010, Chapter 4). Additional examples include CH_4 on Titan, SO_2 on Io, N_2 on Triton and possibly in Titan's past climates, NH_3 and NH_4SH on Jupiter and Saturn, and CH_4 on Uranus and Neptune. On hot Jupiters and other strongly irradiated planets condensibles can even include a variety of substances more commonly thought of as rocks and minerals in Earthlike conditions, such as enstatite ($MgSiO_3$) or iron. In the thesis, the term "moist" will be used to refer to any condensible substance, not just water vapor. The diversity of climate phenomena associated with the choice of condensible is augmented by the variety of relevant noncondensible background gases. For example, planets with an H_2 background gas are of considerable interest, and even Earth and Super-Earth sized planets can retain an H_2 atmosphere if they are in sufficiently distant orbits (Pierrehumbert and Gaidos, 2011). Here we review the condensible-rich atmospheres that have been observed or proposed to be important for planetary climate dynamics.

H_2O-Rich Atmospheres In the present Earth's climate, water vapor is a dilute condensible, in the sense that water vapor makes up a small portion of any parcel of air. For example, saturated air at a Tropical surface temperature of 300 K contains about 3.5% water vapor, measured as a molar (also called volumetric) concentration. The convection parameterizations in use in conventional terrestrial general circulation models rely on a number of approximations appropriate to the dilute limit.

If the planet in question has a large condensed reservoir, such as an ocean or an icy crust, then nondiluteness increases with temperature because, according to the Clausius-Clapeyron relation, the saturation vapor pressure for any substance increases approximately exponentially with the air temperature. Although a variety of dynamical and microphysical effects prevent real atmospheres from attaining saturation, the actual condensible content nonetheless tends to scale with saturation vapor pressure (Pierrehumbert et al., 2007). The diluteness of condensible atmospheres can be measured by the molar mixing ratio of the condensible substance which is the ratio of the partial pressure of the condensible gas to that

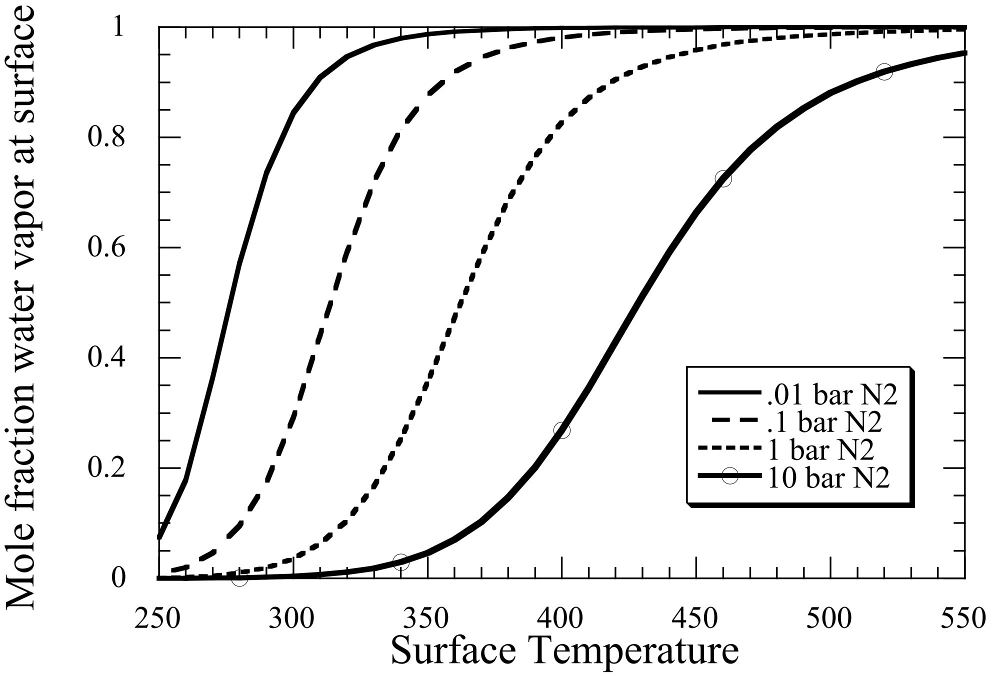

Figure 1.1: The molar concentration of water vapor at the surface as a function of the surface temperature. The calculation assumes that the atmosphere is fully saturated following the moist adiabat. The calculation is done for an atmosphere consisting of water vapor and noncondensible N_2, holding the total atmospheric mass of N_2 fixed as surface temperature is changed. The amount of N_2 in the atmosphere for each curve shown is given in terms of the surface pressure the N_2 would have if it were present in the atmosphere alone (i.e. $g \cdot M_{N2}$, where g is the acceleration of gravity and M_{N2} is the mass of N_2 per square meter of surface).

of the non-condensible gas in the air parcel. Hence the nondiluteness for a given temperature also depends on the mass of the noncondensible background gas in the atmosphere, since a massive atmosphere can dilute a greater quantity of the condensible substance. The way these two factors play out for the case of condensible water vapor in noncondensible N_2 is illustrated in Figure 1.1. In the nondilute case, one must take care with the way the quantity of the noncondensible gas in the atmosphere is specified, as the noncondensible partial pressure becomes dependent on altitude and – for a fixed mass of noncondensible – varies with temperature as the amount of condensible gas in the atmosphere changes. In this graph, we measure the amount of N_2 in terms of the surface pressure the N_2 would exert if it were present in the atmosphere alone, and carry out the calculation in such a way that this quantity (and hence the mass of noncondensible N_2) remains fixed as temperature changes. We call this quantity the N_2 *inventory*, and refer to it by the symbol $p_{N_2,I}$ (with analogous notation for other gases). For a given noncondensible inventory, the temperature at which the atmosphere becomes nondilute is independent of the planet's surface gravity. The corresponding mass of the noncondensible gas A per square meter of the planet's surface, $p_{A,I}/g$, is higher for planets with lower gravity, though.

The condensible fraction is greatest at the ground, so the atmosphere first becomes nondilute there. Hence in Figure 1.1 we show the ground level molar concentration of the condensible H_2O. When the N_2 inventory is 0.01 bar, the low level atmosphere is already roughly half water at temperatures of 270 K, whereas with a 1 bar N_2 inventory (somewhat greater than the present Earth's) this concentration isn't attained until the surface temperature exceeds 350 K. With a 10 bar inventory, the atmosphere is still dilute at 350 K, and doesn't become strongly nondilute until 425 K. Thus, the noncondensible inventory of an atmosphere is a crucial factor in determining the character of moist convection. This result underscores the importance of the factors governing the noncondensible inventory on a planet. Wordsworth and Pierrehumbert (2013b) found that a high noncondensible inventory can also inhibit loss of water, and the reasoning in that paper applies to other condensible substances as well.

Temperature decreases with height on the adiabat, approaching zero as the pressure approaches zero, so within the convective region of an atmosphere – the troposphere – the atmosphere will become more dilute with height even if it is highly nondilute near the surface. Even in the radiative-equilibrium portion of the atmosphere – loosely speaking, the stratosphere – in the absence of atmospheric absorption of incoming stellar radiation temperature decreases with altitude where the atmosphere is optically thick in some portion of the infrared spectrum. However, the temperature decrease ceases where the atmosphere becomes optically thin in the infrared, and suitably strong absorption of incoming stellar radiation can cause the temperature to increase with height, as in Earth's stratosphere (Pierrehumbert, 2010, Chapter 4). Either effect can keep a nondilute lower atmosphere from being capped by a dilute upper troposphere or dilute stratosphere. The factors governing the diluteness of the stratosphere were discussed in detail in Wordsworth and Pierrehumbert (2013b), in connection with the loss of volatiles to space.

H_2O Runaway Greenhouse The most familiar case in which nondilute physics becomes important is in the water vapor runaway greenhouse when the absorbed stellar radiation exceeds the maximum outgoing longwave radiation (OLR) of the climate system. This maximum value of OLR is usually referred to as the 'Kombayashi-Ingersoll limit' (Pierrehumbert, 2010, Chapter 4). The reason that the OLR stops increasing with the surface temperature in an optically-thick moist atmosphere is related to the strong connection between the vapor pressure and the air temperature by the Clausius-Clapeyron relation in the non-dilute atmosphere. The runaway greenhouse phenomenon has been extensively studied in one-dimensional radiative-convective models, but there is an increasing need to explore three dimensional simulations of this phenomenon. Phenomena related to clouds, subsaturation and geographical temperature and constituent variations can only be adequately treated in the context of a three-dimensional general circulation model (GCM). Ishiwatari et al. (2002) carried out pioneering three-dimensional GCM studies of the runaway greenhouse using gray-gas radiation, and found that sub-saturation in the atmosphere played an important role in determining the runaway greenhouse threshold. More recently Leconte et al. (2013) and Yang et al. (2013) carried out simulations incorporating clouds and real-gas radiation, finding that clouds as well as sub-saturation played a critical role. Wolf and Toon (2015) carried out 3D simulations of a hot, moist atmosphere up to temperatures of 360 K, which brings the lower troposphere well into the nondilute regime; convection in this case is treated through a modification of the Zhang-Macfarlane convection scheme, but the nature of the modifications were not discussed.

Nondilute dynamics also generally prevails during the window of time when a planet is actually undergoing a runaway, but before it has lost its surface condensate reservoir to the atmosphere. There is only a narrow window of time of some thousands of years during which this situation persists, but it is still important to understand the dynamics in this regime, since clouds or sub-saturation could in principle act to arrest the runaway.

Nondilute behavior can also occur aloft without a surface reservoir of condensible; this would be the typical situation in a post-runaway atmosphere in which the surface ocean or glacier has been depleted so that the lower atmosphere becomes hot and unsaturated. Nondilute condensing dynamics aloft does not even require the presence of a distinct planetary surface at all. This is important because of the prevalence of fluid super-Earths such as GJ 1214b. One of the conjectured compositions for GJ 1214b is nearly pure water vapor, and while GJ 1214b itself is too hot for water vapor to condense to any appreciable degree within the atmosphere, a similar planet in a somewhat more distant orbit would inevitably have a nondilute condensing layer. Under some circumstances, the layer could remain nondilute even in the face of admixture of some noncondensible background gas such as H_2 or N_2.

The condensing layer can be eliminated if the temperature of the upper atmosphere – presumed to be in radiative equilibrium – is sufficiently hot that the atmosphere never intersects the condensation threshold. This would typically happen as a result of strong absorption of shortwave stellar radiation, but even if the upper atmosphere is in pure infrared radiative equilibrium, the radiative equilibrium temperature of the upper atmosphere can be approximately uniform in height in the optically thin portion of atmospheres with broadband absorbers (Pierrehumbert, 2010, Chapter 4), and it is possible for this temperature to be above the condensation threshold.

Abiotic Oxygen Buildup in H_2O-rich Atmospheres The accumulation of molecular oxygen (O_2) in the Earth's atmosphere has had a profound effect on the subsequent evolution of the biosphere – e.g., the rise in complexity of life to incorporate macroscopic organisms and energetically expensive metabolisms (Catling et al., 2005). On modern Earth, O_2 is produced primarily biologically as the waste product of 'oxygenic photosynthesis'. However, abiotic processes are proposed to be of equal importance for the rise of O_2 in the atmosphere on the Palaeoproterozoic Earth (Claire et al., 2006), and on planets around different type of host stars (Tian et al., 2014; Harman et al., 2015). Under certain circumstances, O_2 may build up to an exceptional abundance in the atmosphere without a biotic source (Wordsworth and Pierrehumbert, 2014; Luger and Barnes, 2015). As is evident from Figure 1.1, a low noncondensible inventory can cause water vapor to be nondilute even at temperatures comparable to the present Earth; as such atmospheres are prone to losing water to space and generating abiotic oxygen (Wordsworth and Pierrehumbert, 2014), the dynamical features that could affect water loss are of considerable interest.

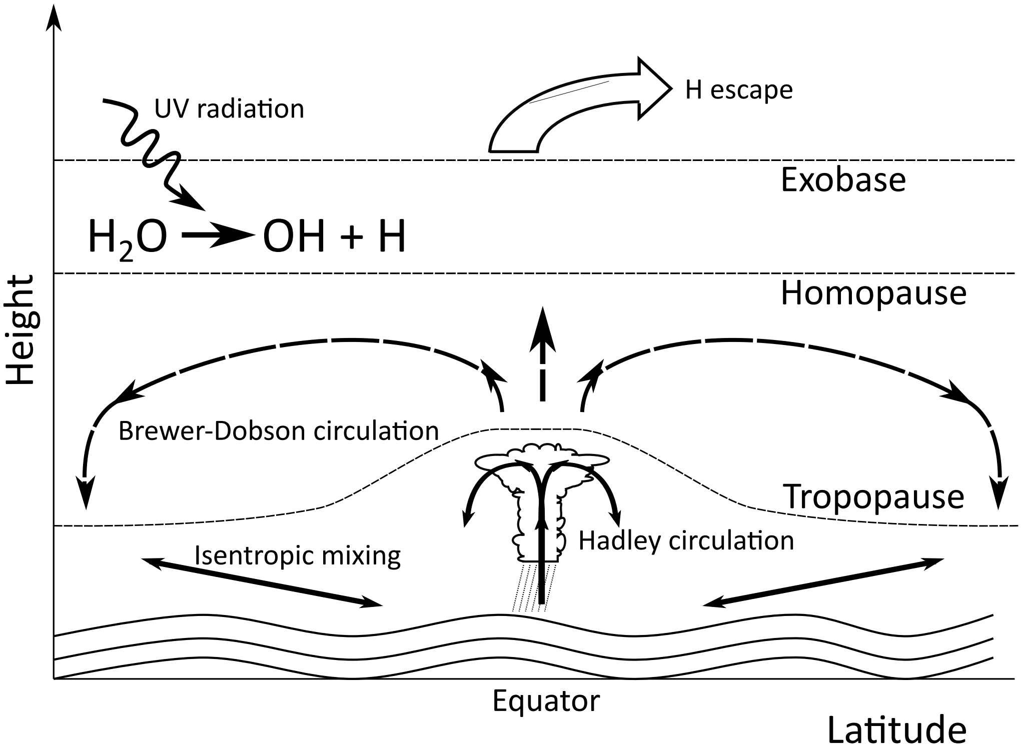

Figure 1.2: A height-latitude schematic of the large-scale moisture transport in the troposphere and how the moisture enters the upper atmosphere passing through the cold tropical tropopause or the cold trap. At high altitudes, water molecules are broken up by ultraviolet radiation, and the escape of hydrogen to space will oxidize the remaining atmosphere..

On the present-day Earth, the rate of water loss and the associated hydrogen escape flux to space (or the equivalent oxidation flux in the atmosphere) is negligible, mainly because of the low water vapor abundance in the upper atmosphere where water molecules are broken up by ultraviolet (UV) radiation. The low water vapor mixing ratio there is the consequence of the dynamical fact that most of the air entering the upper atmosphere has to pass through the frigid tropical tropopause – the coldest region in the global atmosphere – driven by a global scale extratropical 'fluid-dynamical suction pump' (Holton et al., 1995), as illustrated in Figure 1.2. The tropical troposphere thus behaves as a cold trap, limiting moisture transport from the humid surface (a few percent by volume) to high altitudes (a few ppmv). It therefore confines abiotic oxidization in the present Earth's atmosphere to about 10^{10} mol O_2 year^{-1}; a trivial amount compared to the biological source, which is around 10^{13} mol O_2 year^{-1} (Catling, 2014).

This cold trapping mechanism can become less effective under certain conditions (summarized in Figure 1.3), e.g., at high surface temperatures when the saturation water vapor pressure is comparable to the background partial pressure of the non-condensible components, mostly molecular nitrogen (N_2) on modern Earth. Then the moist upper atmosphere will speed up the photolysis rate of water molecules and therefore enhances the hydrogen escape flux and the oxidation state of the atmosphere. The high surface temperature condition has been extensively studied considering the Earth receiving enhanced insolation (Kasting, 1988; Wolf and Toon, 2015; Kasting et al., 2015). The loss rate of water is essential for estimating the lifetime of the surface water inventory on a potentially habitable planet, and is an important factor that determines the inner edge of habitable zone.

However, raising the surface temperature is not the only way to moisten the upper atmosphere. Decreasing the background partial pressure will act in similar way to make the cold trap less effective and enhance the water content in the upper atmosphere (Wordsworth and Pierrehumbert, 2014; Ding and Pierrehumbert, 2016; Pierrehumbert and Ding, 2016), as shown by comparing the blue profile with the yellow one in Figure 1.3. Wordsworth and

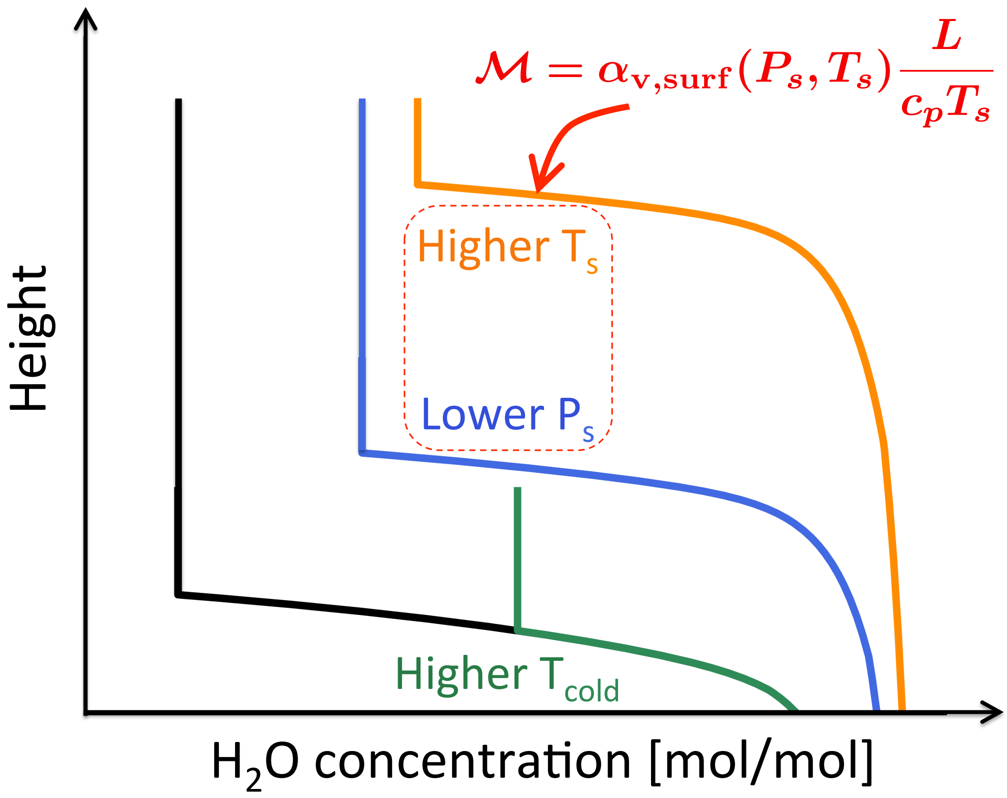

Figure 1.3: Schematic illustrating factors that control the effectiveness of the cold trap. An increase in the air temperature at the cold trap (T_{cold}, green line) or the surface air temperature (T_s, yellow line), or a decrease in surface background partial pressure ($p_{s,d}$, blue line) tends to increase the water vapor mixing ratio in the upper atmosphere. The effect of the surface air temperature and pressure can be summarized by a non-dimensional parameter discussed in Wordsworth and Pierrehumbert (2013b) that is shown as $\mathcal{M}$ in the figure.

Pierrehumbert (2013b) separated the effect of surface temperature and background partial pressure, and defined a non-dimensional parameter that measures when the 'moist stratosphere' situation occurs with a fixed cold trap temperature. As the consequence of no limitation on the surface temperature, the Earth's atmosphere with reduced N_2 content is expected to lose water rapidly even at current surface temperature. In the extreme case, without any background component in the atmosphere, the rapid water loss on an Earth-like terrestrial planet may produce an oxygen-rich atmosphere even in a very cold state (i.e., global glaciation) until the buildup of O_2 forms an effective cold trap again. This scenario is qualitatively discussed in Wordsworth and Pierrehumbert (2014), but has not yet been studied in more realistic models.

As summarized in Figure 1.2 and 1.3, the water vapor mixing ratio in the upper atmosphere is only related to the climate conditions at specific location on the planet. Hence it is affected by not only the radiative transfer in the atmosphere but also the large-scale atmospheric dynamics. Take the air temperature at the cold trap in Earth's atmosphere as an example. It is affected by not only the radiatively active components in the atmosphere (greenhouse gases, clouds and aerosols, etc.) but also the vertical advective cooling induced by the stratospheric circulation, and is significantly different from the result in one-dimensional radiative-convective equilibrium (1D RCE) calculation (Haqq-Misra et al., 2011). Due to the limitation of 1D simulations, 3D simulation is required to explore the water vapor concentration in the upper atmosphere within 3D general circulation models (GCMs), taking the effect of atmospheric circulation into account.

CO_2-Rich Atmospheres and CO_2 Runaway Greenhouse CO_2 is the nondilute condensible constituent on Early Mars (Kasting, 1991; Forget et al., 2013), and more generally near the outer edge of the conventional habitable zone where habitability is supported by the greenhouse effect of a thick CO_2 atmosphere whose mass is limited by CO_2 condensation onto the surface (Wordsworth et al., 2010). This would typically occur on planets illuminated somewhat more faintly than current Mars, but which (unlike current Mars) are sufficiently carbonate-rich and which have sufficiently active tectonics to support substantial outgassing of CO_2 from decomposition of carbonates in the deep interior of the planet. Similar to the discussion on H_2O runaway greenhouse, the outgassed CO_2 from the interior cannot accumulate in the atmosphere arbitrarily unless the CO_2 runaway greenhouse state is reached and the absorbed stellar flux of the climate system exceeds the the Kombayashi-Ingersoll limit of CO_2 ($\sim 70\,\mathrm{W\,m^{-2}}$).

On the warm side of the outer edge of the habitable zone, one would get nondilute layers which do not reach the surface, as in the post-runaway greenhouse state. This situation would be expected in the CO_2-rich atmospheres of a warm, wet Early Mars, or on a Super-Earth like GJ 581d (Wordsworth et al., 2011) if made habitable by a massive CO_2 atmosphere. If somewhat beyond the cold edge of the conventional habitable zone, such planets would instead develop CO_2 oceans or glaciers at the surface, with a nondilute layer extending all the way to the condensible reservoir at the ground. In either case, nondiluteness would survive in the face of the addition of a moderate amount of noncondensible background gas such as N_2 or H_2.

Pure-Condensible Atmospheres Observations suggest on some of icy satellites in the Solar system the atmosphere is dominated by condensible components and most of the surface covered by the condensate is in vapor equilibrium with the above air (e.g., Io with condensing SO_2 atmosphere and Triton with condensing N_2 atmosphere). This kind of atmosphere, referred to as the pure condensible atmosphere or pure steam atmosphere in the thesis, has a completely different circulation regime compared to atmospheres with the dilute condensible component. As the consequence of the strong connection between the surface temperature and pressure via the Clausius-Clapeyron relation, the surface pressure gradient points from the cold region to the hot region in the pure condensible atmosphere. Therefore the atmospheric circulation is characterized by a strong low-level flow from warm region that carries both momentum and energy fluxes to cold places, and is referred to as 'sublimation-driven flow' in Ingersoll et al. (1985). As a comparison, atmospheres with dilute condensible component are similar to dry atmosphere with surface pressure gradient pointing from the hot substellar region to other places, if the rotation effect of the planet is weak. Then the atmosphere is characterized by an overturning circulation rising from the warm region so that the potential energy of atmosphere built up by radiation is released and is converted to the kinetic energy. The Hadley cell and Walker cell in the Earth's tropics are examples of this type of atmospheric circulation. In terms of mass balance, in dilute atmospheres, the convergence of the low-level flow is balanced by the divergence of the high-level return flow, while in pure condensible atmosphere, it is balanced by the local evaporation minus precipitation flux at the surface without any return flow in the upper atmosphere.

A unique feature of pure-condensible atmospheres is that the saturated moist adiabat giving temperature as a function of pressure has no free parameters. The saturated moist adiabat in pure-condensible atmospheres can be derived directly from the Clausius-Clapeyron relation, in which the only constants describe thermodynamic properties of the gas. For mixed atmospheres containing noncondensible components, the saturated moist adiabat contains a free parameter, namely the mass concentration q_a of the noncondensible gas at some given pressure level. This allows the temperature at a reference pressure level p_0 to be chosen freely, subject to the constraint that $T(p_0)$ be less than $T_{sat}(p_0)$, at which temperature $q_a = 0$. As $T \rightarrow 0$, $q_a \rightarrow 1$. Once $q_a(p_0)$ is known, the saturated moist adiabat is uniquely determined. For mixed atmospheres the saturated moist adiabat is thus a one-parameter family of curves. q_a is constrained by the total mass of noncondensible gas in the atmosphere, which must remain fixed, but this is a global constraint obtained by integrating over the entire atmosphere, and cannot be applied locally. In contrast, within any saturated layer of a pure-condensible atmosphere, the temperature is known once the pressure is known without any need to supply additional information.

Pure condensible atmospheres were also proposed to form under various scenarios with different kinds of volatiles, e.g., dense condensing CO_2 atmosphere on Early Mars (Forget et al., 2013) and on planets near the outer edge of the habitable zone (Wordsworth et al., 2010), condensing N_2 atmosphere on Pluto (Zalucha, 2016) and on Early Titan (Charnay et al., 2014), and the extreme hot rocky vapor atmosphere on close-in rocky exoplanets with permanent dayside magma oceans (Castan and Menou, 2011).

Compositional Effect on Buoyancy For non-dilute atmospheres that are not yet dominated by the condensible component, the behavior of moist convection is strongly influenced by the compositional effect on buoyancy in the atmosphere. Consider a saturated air parcel from the surface reservoir that is lifted through the unsaturated surroundings. It will be positively buoyant if the molecular weight of the condensible constituent is lower than that of the non-condensible background, as is the case for H_2O in Earth's air (Pierrehumbert, 2010).

On the contrary, moist convection tends to be inhibited if the condensible constituent has a higher molecular weight. The condensible constituent therefore can only reside near the surface reservoir and is difficult to be transported upward. One could imagine the case of moist CO_2 convection in a N_2 background atmosphere. In fact, this phenomenon is often seen and of great importance for moist convections in the hydrogen-helium atmospheres on giant planets, since H_2 and He are the lightest components in planetary atmospheres. As the consequence of large difference in molecular weight between the condensible and non-condensible components, the buoyancy effect becomes important even when the mass mixing ratio of the condensible constituent is smaller than order of unity. Study by Guillot (1995) suggested that moist convection tends to be inhibited on Uranus and Neptune if the abundance of CH_4 is higher than 15 times the solar value and on Jupiter and Saturn if the abundance of H_2O is higher than 5 times the solar value. Although moist convection is usually inhibited, it can still be triggered if enough available potential energy has been built up typically by radiative cooling in the upper atmosphere. As the heavier condensible constituent condenses and leaves the convecting plume, the air parcel is positively buoyant again and thus the moist convection is enhanced. This mechanism is proposed to be responsible for the recurrence of the planet-encircling storms on Saturn every 20$\sim$ 30 years that have been observed since 1876 (Li and Ingersoll, 2015).

1.3 Fundamental Questions and Methodology

All of the issues discussed in the thesis are independent of the choice of condensible and noncondensible gases, though the choice of gases does affect the surface temperature at which the atmosphere begins to become nondilute, for any given inventory of noncondensible gas. For example, given a 1 bar inventory of noncondensible gas, CO_2 condensing in an N_2 atmosphere reaches 50% molar concentration at the ground for a surface temperature of 195 K, and CH_4 condensing in N_2 reaches that molar concentration at 110 K. For N_2 condensing in an H_2 background, the threshold is 95 K. Here we have taken a molar concentration of 50% as an arbitrary boundary beyond which the nondilute effect is expected to be important. For some effects, notably effect of the condensible content on the surface pressure, it is the mass fraction that is most directly relevant. The mass fraction differs greatly from the molar concentration for species with very different molecular weight. For N_2 condensing in an 1 bar H_2 background, the mass fraction is 93.3% at 50% molar concentration, so that 50% mass concentration would be attained at a much lower temperature than 95K.

The studies introduced in Section 1.2 cover a wide variety of condensible-rich atmospheres. A general understanding of condensible-rich atmospheres is required to explore the difference from dilute atmospheres. Moreover, none of these studies explicitly discussed the novel aspects of convection in the nondilute case, or the physics involved in maintaining energy conservation. Generally speaking, there is a need for convection parameterizations that cover the non-dilute limit accurately and are suitable for incorporation in GCMs. There is also a broad need for a better understanding of how moist convection operates in nondilute systems.

The dilute approximation enters into the formulation of convection parameterizations used in conventional GCMs in several ways. First, it is used in the approximate form of moist enthalpy to enforce energy conservation in physical processes involving condensation. Second, it is invoked in order to neglect the energy carried away by precipitation. Third, it is used to justify the neglect of pressure changes that occur when condensate mass is added to the atmosphere by evaporation or taken away by precipitation . When the convection is nondilute, the pressure effect can be important in driving atmospheric circulations. Moreover removing mass from a layer of the atmosphere by precipitation unburdens the layers below, causing them to expand and do pressure work. Finally, in the nondilute case there is a need to carefully take into account the effect of changing atmospheric composition on mean thermodynamic quantities such as specific heats or gas constants (though some existing parameterizations already take such things into account, at least approximately).

Many of the novel aspects of nondilute convection affect energy conservation properties. In situations where it is necessary to accurately track transient behavior (e.g. in seasonal or diurnal cycles) or in which energy is transported from one geographical location to another (as in a GCM), energy conservation becomes crucial. Even in a steady state in a single-column model, energy conservation is important in models that explicitly resolve the surface energy balance, since energy deposited at the surface is transferred to the lowest model layer, whereafter it needs to be communicated upward by convection without loss or gain. The only situation in which energy conservation in the course of convective adjustment is unimportant is that in which detailed modeling of energy transfer between surface and atmosphere is replaced by an assumption that the surface temperature equals the immediately overlying air temperature, provided that only the steady state with infrared radiation to space balancing net absorbed stellar radiation is of interest. This is a fairly common approach in radiative-convective models, which has allowed many studies (e.g., Kasting, 1991) to avoid the necessity of confronting energy conservation in nondilute convection.

In the following chapters, we progressively construct a physical understanding of the climate in condensible-rich atmospheres from simple 1D radiative-convective equilibrium calculations to 3D simulations. Key questions such as the energetics and the basic nature of nondilute moist convection, the spatial distribution of temperature, moisture, wind fields, the efficiency in heat redistribution in condensible-rich atmospheres and how this study will be of benefit to characterizing potentially habitable exoplanets if water vapor is the condensible substance will be investigated and answered.

1.4 Thesis Overview

We begin in Chapter 2 by a complete description of the convection scheme. The simple parameterization of moist convection is valid from the dilute to the nondilute limit, and will be used to discuss the basic character of nondilute convection. In 1D radiative-convective simulations, we show that this scheme conserves energy whether the condensible substance is dilute in the atmosphere or not in Chapter 3. As an example of the behavior of the scheme, we apply it to an atmosphere undergoing a runaway greenhouse on a planet with a high eccentricity orbit in Section 3.4. This serves as a test of energy conservation in a situation involving strong transient forcing. We discuss key differences between dilute and nondilute convection, as revealed by our simulations, in Section 3.5.

In Chapter 4, we first discuss the analytical results on the nature of nondilute climates in Section 4.2. The Exo-FMS general circulation model, which is implemented by the moist convection scheme and designed to remain valid for nondilute circulations, is described in Section 4.3. In Section 4.4 we present some preliminary simulation results illustrating the transition from dilute to nondilute behavior on rapidly rotating planets, and then show how some of the features of nondilute atmospheres are manifest in these simulations.

We continue to use Exo-FMS to simulate the thin condensible-rich atmosphere with a weak cold trap on slowly and synchronously rotating planets in Chapter 5. Previous work has been done on moist atmospheres with a weak cold trap but induced by other mechanisms. We then compare our simulation results with previous studies.

In Chapter 6, we focus on pure condensible atmospheres, and build simple 1D energy balance model to study the circulation in pure condensible atmospheres. A non-dimensional parameter that determines whether the atmosphere is global or local is derived based on the 1D model. The situation with non-condensible as a minor constituent in the atmosphere is discussed.

We conclude in Chapter 7.

CHAPTER 2

AN ENERGY-CONSERVING GENERAL MOIST CONVECTION SCHEME

2.1 Introduction

In this chapter, we formulate and test a simplified convection parameterization scheme that can deal with the full range of situations from dilute to condensible-dominated behavior, and use the scheme to explore some of the novel aspects of nondilute moist convection. The scheme is suitable for use both in single-column radiative convective models and in general circulation models. The scheme applies to any combination of a single condensible substance and noncondensible background gas, and conserves energy for any concentration of the condensible component.

The development of our scheme builds in part on the treatment of convection in a pure CO_2 Martian atmosphere given in Forget et al. (1998), and the related scheme for thicker atmospheres employed in Wordsworth et al. (2011). Leconte et al. (2013) incorporated some aspects of nondilute behavior in their 3D runaway greenhouse study, but did not specifically discuss the convection scheme, its energy conservation properties or the nature of nondilute convection. Further development of the subject requires a broader discussion of the basic ways in which nondilute convection differs from the familiar dilute case.

Manabe and Strickler (1964) first introduced a convective adjustment scheme in their study of a single air column subject to atmospheric radiation and convection. In their convection scheme, once the vertical lapse rate in the model exceeds a critical value (e.g., $6.5\,\mathrm{K\,km^{-1}}$, a typical value for present Earth's mid-latitude atmosphere), it is reset to the critical value. This assumes that the free convection is strong enough to maintain the assumed critical lapse rate. The critical lapse rate determines only the local slope of the adjusted $T(p)$ and an additional principle must be invoked to determine the intercept. In the initial version of the Manabe scheme, the column-integrated dry enthalpy $\int_0^{p_s}(c_pT)\mathrm{d}p/g$ is assumed to be conserved during the convective adjustment,where p_s is the surface pressure, c_p is the specific heat of dry air and g is the acceleration of gravity. Energy stored in the form of latent heat was not taken into account. Manabe et al. (1965) modified this convection scheme for a moist atmosphere when studying the climatology of a GCM with a simple hydrological cycle. This parameterization used the moist adiabat as the critical lapse rate and conserved the column-integrated moist enthalpy in the dilute limit $\int_0^{p_s}(c_pT + Lq)\mathrm{d}p/g$ during the convective adjustment, where L is the latent heat of condensation and q is the mass mixing ratio of water vapor. Betts (1986) and Betts and Miller (1986) proposed another new convection scheme (now known as the Betts-Miller scheme) by relaxing the temperature and humidity profiles gradually towards the post-convective equilibrium states with a given relaxation timescale. The precipitation rate and the change of the temperature and humidity profiles during the convective adjustment are again computed using conservation of the column-integrated moist enthalpy in the dilute limit. These schemes are widely used in idealized experiments (Renn et al., 1994; Frierson, 2007; O'Gorman and Schneider, 2008; Merlis and Schneider, 2010).

In this thesis, we propose a new simplified convection scheme similar in spirit to the convective adjustment scheme in Manabe and Strickler (1964) and the Betts-Miller scheme, but without assuming the condensible substance to be dilute. The resulting scheme conserves non-dilute moist enthalpy, takes the enthalpy of condensate and the mass loss from precipitation into account, and works for both dilute and non-dilute cases no matter what the condensable substance is.

The atmosphere is divided into discrete layers, and the scheme is applied iteratively to adjacent pairs of layers. The adjustment is performed for each pair of layers from bottom to top, with the procedure being repeated until the temperature and moisture profiles converge to their asymptotic form within the specified degree of accuracy.

When a pair of adjacent layers is found to be unstable to convection, adjustment to a neutral state is performed through a two step process. The subdivision of the adjustment into steps makes it easier to assure that each step (and hence the whole process) conserves energy. First, the pair is adjusted to the reference neutrally stable state of temperature and humidity conserving the summed nondilute moist enthalpy and moisture of the two layers, assuming that the final state is saturated in both layers. Condensate formed in this step is retained in each layer in such a way that the total mass of each layer remains unchanged; hence in this step the pressure of the interface between the layers and of lower layers remains unchanged, in accordance with hydrostatic equilibrium. If there is not enough moisture present to saturate both layers, the adjustment is done without forming any condensate, in a manner that will be detailed later.

In the second step, condensate is removed from the layers. For simplicity, we currently assume infinite precipitation efficiency, so that all precipitation is transported to the surface without any evaporation along the way; we also neglect heating due to frictional dissipation associated with the falling precipitation. The scheme can be easily modified to incorporate these complicating effects, but here we wish to focus on the most basic effects of nondiluteness. When the condensate is removed, the atmosphere is allowed to adjust to the resulting change in pressure, and the energy carried by precipitation is tracked, in such a way that the system conserves energy in the course of precipitation.

When mass is removed from the atmosphere by precipitation, the potential and thermal energy of the precipitation must be added to the surface energy reservoir for energetic consistency. At the bottom boundary, surface fluxes remove energy and condensate mass from the surface reservoir, and add it to the lowest model layer. In Sections 2.4 and 2.5 we show how the energy budget is balanced in the course of these processes.

Any problem involving condensation must confront the difficult issue of microphysics – loosely speaking the kinetics governing initial formation of condensate, the subsequent growth of particles by collision and coalescence, their transport by precipitation, and their mass loss due to evaporation as they fall through subsaturated layers of the atmosphere. These phenomena are all of considerable importance. For example, a parcel of atmosphere which is cooled by lifting or by radiative cooling can become highly supersaturated before condensate forms, in the absence of suitable cloud condensation nuclei (CCN's) to serve as sites to trigger initial formation of condensate. The density of CCN's can control the initial size of condensate particles, which in turn governs how long they take to grow to a size sufficient to cause appreciable sedimentation. The physical chemistry determining when a particle is a good CCN, and the factors governing the sources and sinks of CCN's pose formidable challenges even for the well-observed case of dilute condensation of water vapor on Earth. There is little doubt that microphysics will prove to be of great importance in governing condensible dynamics in the nondilute and chemically diverse atmospheres, but we will not attempt to address such issues in the present work. As an initial step in the exploration of nondilute dynamics, we will work in a highly idealized world in which there is sufficient supply of CCN that condensation always keeps the system from becoming supersaturated, in which condensate particles grow sufficiently quickly that they can be regarded as instantaneously removed by precipitation, and in which no mass of precipitate is lost on the way to the planet's surface condensate reservoir.

2.2 Thermodynamic Preliminaries: Nondilute Moist Enthalpy and the Nondilute Pseudoadiabat

We begin with a review of some relations pertinent to energy conservation in the nondilute case. The calculations involve three atmospheric constituents: a noncondensible gas (or mixture of gases) referred to with subscript a, and a condensible substance whose gaseous form is referred to by subscript c and whose condensed form is referred to by subscript ℓ. The subscript t will be used to refer to quantities associated with the total mass of condensible in both phases.

The temperature dependence of latent heat enters the problem at several points. When the density of the condensate is much greater than that of the vapor phase, the specific latent heat varies linearly with the temperature (Emanuel, 1994, p. 115).

$$\frac{\mathrm{d}L}{\mathrm{d}T} \approx c_{pc} - c_{p\ell} \tag{2.1}$$

Here subscript ℓ represents the condensate, which may be in a solid or liquid phase. We will take this temperature dependence into account in our formulation, but assume the specific heats to be independent of temperature.

Next consider a parcel of atmosphere which has become supersaturated by one means or another, and which relaxes back to saturation through condensation without loss of energy or mass. Thus

$$\mathrm{d}m_c + \mathrm{d}m_\ell = 0, \qquad \mathrm{d}m_c < 0 \tag{2.2}$$

where m_c and m_ℓ are the mass of condensible gas and condensate in the parcel. Suppose further that the pressure is kept constant in the course of the condensation. In hydrostatic equilibrium, this would correspond to the situation in which no mass is lost from the column of atmosphere above the parcel in question. The First Law of Thermodynamics then implies

$$0 = L(T)\mathrm{d}m_c + (c_{pa}m_a + c_{pc}m_c + c_{p\ell}m_\ell)\mathrm{d}T \tag{2.3}$$

where m_a is the mass of noncondensible in the parcel. From Eq. 2.1 and the assumption that specific heats do not depend on temperature. we deduce

$$L(T)\mathrm{d}m_c = \mathrm{d}[L(T)\ m_c] - (c_{pc} - c_{p\ell})m_c\mathrm{d}T \tag{2.4}$$

Combining this result with Eq. 2.3 we can define a quantity which is conserved in the course of isobaric condensation without loss of mass or energy:

$$\tilde{k} = (c_{pa}m_a + c_{p\ell}m_t)T + L(T)m_c, \tag{2.5}$$

where $m_t = m_c + m_l$. The conserved variable $\tilde{k}$ is usually referred as the moist enthalpy (Emanuel, 1994, p. 118). Dividing by $m_a + m_t$ yields the moist enthalpy per unit total mass

$$k = (c_{pa}q_a + c_{p\ell}q_t)T + L(T)q_c, \tag{2.6}$$

where q is the mass concentration of the atmospheric constituent indicated by each subscript. This expression remains well behaved even in the pure steam limit with $q_a = 0$ and $q_t = 1$. Allowing for pressure work done by the parcel in the general case, the First Law becomes

$$\mathrm{d}k - \frac{1}{\rho}\mathrm{d}p = \delta Q \tag{2.7}$$

where ρ is the total density of all constituents and δQ is the energy change due to such processes as radiative heating or cooling. Alternately, in a temperature-volume formulation the First Law can be written as

$$\mathrm{d}\left(k - \frac{p}{\rho}\right) + p\mathrm{d}\frac{1}{\rho} = \delta Q \tag{2.8}$$

Eqns. 2.7 and 2.8 are conservation law that apply following an individual air parcel, but that is not generally the same as the conservation law that applies when a column consisting of various air parcels is mixed by convection. Even if the initial and final states of the column are in hydrostatic balance, convection proceeds through nonhydrostatic motions, so energy conservation must be formulated to allow for nonhydrostatic dynamics. This is most easily done using altitude (z) rather than pressure (p) as the vertical coordinate. In Appendix A it is shown that an isolated volume of atmosphere conserves the quantity

$$\int_{z=0}^{\infty} \rho \cdot \left(k - \frac{p}{\rho} + gz\right) \mathrm{d}z \tag{2.9}$$

upon mixing by fluid motions of an arbitrary type, provided any condensate formed is retained within the air parcel in which it forms (though it is free to evaporate back into the air parcel). The density ρ in this formula includes the mass of condensate. This proceeds from a small variant of a standard thermodynamic derivation, but it is reproduced in Appendix A for the sake of checking that it remains valid even in the nondilute limit, and even in the presence of condensate.

The conservation law given in Eq. 2.9 is an approximate form of the exact conservation law, valid when kinetic energy in the initial and final states is negligible compared to the thermal energy. The energy contains contributions both from the internal energy $k - p/\rho$ and potential energy gz. In the dilute case for an ideal gas, $q_a \approx 1$, $p/\rho \approx R_a T$, $q_t \ll q_a$ and the internal energy takes on the familiar form $c_{va}T + Lq_c$. Returning to the general case, if the column is in hydrostatic balance, then $g\rho \mathrm{d}z = -\mathrm{d}p$ and

$$\int_{z=0}^{\infty} \rho g z \mathrm{d}z = \int_{p=0}^{p_s} z \mathrm{d}p = -\int_{p=0}^{p_s} p \mathrm{d}z = \int_{z=0}^{\infty} p \mathrm{d}z \tag{2.10}$$

where p_s is the surface pressure. Thus, for a column in hydrostatic balance the potential energy term cancels the term in Eq. 2.9 arising from p/ρ whence we conclude that the quantity

$$\int_{p=0}^{p_s} k \mathrm{d}p \tag{2.11}$$

is conserved in the course of mixing of a column of atmosphere provided the initial and final states are in hydrostatic balance and no mass is lost from any air parcel in the course of the mixing. The potential energy does not appear explicitly in this expression, but it is implicitly accounted for through the fact that c_p rather than c_v appears in the expression for enthalpy k. This will be important when we come to consider the energy carried by precipitation that removes mass from the atmosphere. One knows intuitively that part of the energy carried by the precipitation should be in the form of potential energy – that is after all where hydroelectric power comes from, namely the potential energy of water vapor stored in the atmosphere when solar energy is used to drive convection which lifts the water vapor to higher altitudes. Without carefully considering the above derivation, it is not clear where this potential energy is taken from when mass is removed from the atmosphere. The energy book-keeping is transparent if done in z-coordinates but is more subtle when done in p coordinates for a hydrostatic atmosphere. We will return to this point in Section 2.4 where we deal with mass loss.

We use the pseudoadiabat (Pierrehumbert, 2010, p. 129) as the reference temperature profile, meaning that the condensate does not accumulate in the atmosphere to the extent that the temperature profile would be significantly affected. By substituting the expression for $\mathrm{d}\ln p_a/\mathrm{d}\ln p$ into the formula given in Pierrehumbert (2010, p. 129), the pseudoadiabatic slope can be written in the form

$$\frac{\mathrm{d}\ln p}{\mathrm{d}\ln T} = \frac{p_{sat}}{p}\frac{L(T)}{R_cT} + \frac{p_a}{p}\frac{c_{pa}}{R_a}\frac{1+\left(\frac{c_{pc}}{c_{pa}} + \left(\frac{L}{R_cT}-1\right)\frac{L}{c_{pa}T}\right)r_{sat}}{1+\frac{L}{R_aT}r_{sat}} \tag{2.12}$$

This expression remains valid even in the nondilute case. Here p_{sat} is the saturation vapor pressure, L is the specific latent heat of vaporization, R is the specific gas constant, c_p is the specific heat capacity at constant pressure, r_{sat} is the saturation mass mixing ratio. Note that the pseudoadiabat reduces to the Clausius-Clapeyron relation at temperatures high enough that $r_{sat} \gg 1$, in which case $p \to p_{sat}$ and $p_a/p \to 0$.

2.3 Lapse Rate Adjustment with Retained Condensate

Consider two adjacent layers of atmosphere arranged as in Figure 2.1. The lower layer has pressure and temperature (p_1, T_1) and pressure thickness Δp_1, while the upper layer has pressure and temperature (p_2, T_2) and pressure thickness Δp_2.

In the first step of the convection scheme, we check the temperature difference between the two layers. If it is steeper than the pseudoadiabat computed on the basis of Eq. 2.12, heat and moisture is assumed to mix between the two layers, resulting in a state that satisfies the following criteria:

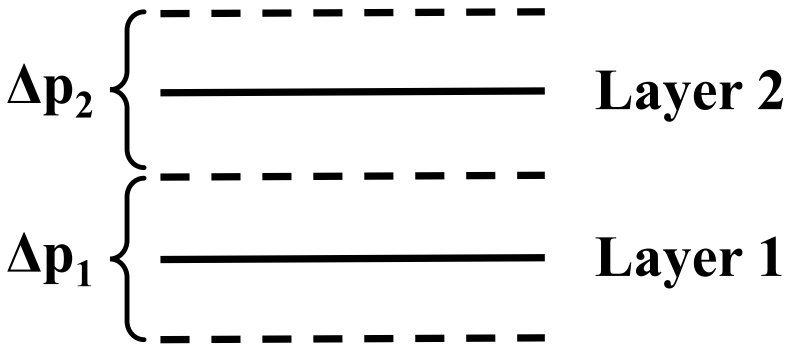

Figure 2.1: Notations used for the moist convective adjustment.

- The temperature difference between the layers is given by the slope of the pseudoadiabat.
- The vapor phase of the condensible is saturated in each layer, provided that the mass of condensible in the adjusted state is less than or equal to the available condensible mass in the initial state.
- The excess of condensible mass between the initial and final state is turned into condensate, which is retained within the two layers.
- The net nondilute moist enthalpy of the two layers is the same as in the initial state.
- The net mass in each layer remains unchanged, so according to the hydrostatic relation, Δp_1 and Δp_2 are the same in the initial and adjusted states.

The last of these assumptions is not really a physical assumption, but rather a convention about how the pressure layer interfaces are labeled after mixing takes place. This set of requirements gives rise to a nonlinear relation with one unknown parameter, which can be taken to be the temperature of the lower layer after adjustment; this parameter is adjusted using a Newton iteration until the conditions are satisfied to within a specified accuracy.

Specifically let $T_{1,I}$ be the lower layer temperature for the initial state and $T_{1,F}$ be the lower layer temperature for the adjusted state, with analogous notation for the other quantities. The temperature difference $\Delta T \equiv T_1 - T_2$ on the pseudoadiabat is computed from Eq. 2.12, and if $T_{1,I} - T_{2,I} > \Delta T$ convection is initiated and the temperatures are reset to

$$T_1 = T_{1,F},\ T_2 = T_{1,F} - \Delta T \tag{2.13}$$

where $T_{1,F}$ is yet to be determined. Because condensate forms in the course of the adjustment, it is most convenient to express the saturation assumption in terms of the mixing ratios r_c of gas-phase condensible relative to the non-condensible component.

$$r_{c1,F} = r_{\text{sat}}(T_{1,F}, p_1),\ r_{c2,F} = r_{\text{sat}}(T_{2,F}, p_2) \tag{2.14}$$

where $r_{\text{sat}}(T, p)$ is the function giving the mixing ratio at saturation.

Conservation of mass of condensible substance between the initial and adjusted states requires

$$\frac{r_{c1,F} + r_{\ell 1,F}}{1 + r_{c1,F} + r_{\ell 1,F}}\Delta p_1 + \frac{r_{c2,F} + r_{\ell 2,F}}{1 + r_{c2,F} + r_{\ell 2,F}}\Delta p_2 = q_{c1,I}\Delta p_1 + q_{c2,I}\Delta p_2 \tag{2.15}$$

since there is assumed to be no retained condensate in the initial state. This yields only one constraint for the two unknowns $r_{\ell 1,F}$ and $r_{\ell 2,F}$. Because total mass is conserved in each layer, the expression for conservation of non-condensible mass does not yield an independent relation. In order to close the problem, an assumption must be made regarding the distribution of condensate between the two layers. Defining $\eta \equiv r_{\ell 2,F}/r_{\ell 1,F}$ allows Eq. 2.15 to be solved for $r_{\ell 1}$, whence multiplication by η gives $r_{\ell 2}$. The left hand side of Eq. 2.15 is monotonic in $r_{\ell 1}$ and approaches $\Delta p_1 + \Delta p_2$ for $r_{\ell 1} \to \infty$, which is guaranteed to be greater than the right hand side because $q_c \leq 1$. If the initial state has enough condensible to saturate both layers, then the left hand side is less than the right hand side when $r_{\ell 1} = r_{\ell 2} = 0$, whence we conclude there is a unique solution with positive r_ℓ. If this condition is not satisfied, there is no physical solution. We will discuss the handling of that case shortly.

With the above assumptions, it is possible to compute the enthalpies $k_{1,F}$ and $k_{2,F}$ in the adjusted layers given $T_{1,F}$. Then $T_{1,F}$ is adjusted using a Newton iteration until the enthalpy conservation relation

$$k_{1,F}\Delta p_1 + k_{2,F}\Delta p_2 = k_{1,I}\Delta p_1 + k_{2,I}\Delta p_2 \tag{2.16}$$

is satisfied.

There is no clear physical basis for determining η but we do not believe it is a critical parameter of the scheme, since all condensate is removed in the second stage of the adjustment process. In the calculations we adopted the choice

$$\eta = \frac{1 + r_{c2}}{1 + r_{c1}} \tag{2.17}$$

which implies that condensate mass is distributed in proportion to the gas-phase mass of the atmosphere. This was found to yield a stable iteration, and also has the virtue of allowing Eq. 2.15 to be solved analytically for $r_{\ell 1}$ in terms of a simple linear equation.

It sometimes happens that there is not enough moisture in the initial state to allow a saturated adjusted state to be realized, i.e. that the adjusted saturated state would require negative precipitation. In such a case we still adjust the temperature to the pseudoadiabat in an enthalpy conserving way, but do not form any precipitation. In this case, the condensible vapor is redistributed in proportion to the final state saturation mixing ratio, with a proportionality constant $f_1 < 1$ chosen to conserve the condensible mass between the initial and final state:

$$r_{c1,F} = f_1 r_{\mathrm{sat}}(T_{1,F}, p_1),\ r_{c2,F} = f_1 r_{\mathrm{sat}}(T_{2,F}, p_2) \tag{2.18}$$

The temperature and moisture adjustment employed here is similar to the treatment of shallow nonprecipitating convection in the Simplified Betts Miller scheme (Frierson, 2007) that could release the convective available potential energy effectively in the tropical region and is used in many conventional general circulation model studies.

Condensation can also happen in the absence of convection, and such condensation is generally referred to as large-scale condensation. In a 3D general circulation model it can happen as a result of uplift and adiabatic cooling caused by the resolved large scale circulation, but it can also be caused by radiative cooling; the latter mechanism is the only large scale condensation mechanism in a 1D radiative-convective model. When large scale condensation forms, it can simply be added to the condensate (if any) produced by the convection step, and dealt with in the precipitation scheme described in the next section.

2.4 Precipitation and Mass Loss from the Atmosphere

In the precipitation step, condensate mass is removed from the atmosphere one layer at a time. The precipitation is assumed to reach the surface instantaneously without loss of energy or mass along the way. When this happens, an amount of enthalpy $c_{p,\ell}Tq_\ell\Delta p/g$ is removed from the layer and added to the surface energy budget. The temperature of the remaining gas in the layer remains unchanged, but the layer thickness Δp goes down in accord with the mass loss from the layer. This reduces the pressure of all the layers located at lower altitudes. When condensate is removed, it is like taking a brick off the top of a piston supporting a column of air; the piston rises, and the air in the cylinder below the piston expands adiabatically until the reduction in pressure force equals the new force of gravity exerted by the mass of the piston. In the course of the expansion, the air temperature drops adiabatically and the pressure work is done.

In the context of an atmospheric column, the enthalpy of layers below the one from which condensate was removed goes down to compensate for the pressure work done. This reduction is manifest as a reduction in the temperature of the lower layers, but because no mass is taken away from the lower layers in this step, their individual pressure thicknesses remain unchanged. The temperature reduction typically leads to supersaturation, but that is dealt with at the next condensation and convection step.

The pressure work done in the course of the expansion of the lower layers, and hence the enthalpy reduction in those layers, can be computed as follows. Let p_1 be the pressure of the level from which a condensate mass (per unit area) δm was removed, and let z_1 be the corresponding altitude. Then the work per unit mass done at some level $p > p_1$ is

$$\frac{1}{\rho}\delta p = \frac{1}{\rho} g \delta m \tag{2.19}$$

Then, doing a mass-weighted integral of this over all the lower layers yields the pressure work

$$\delta W \equiv \int_{p_1}^{p_s} \left[\frac{1}{\rho}\delta p\right] \frac{1}{g} \mathrm{d}p = g\delta m \int_{p_1}^{p_s} \frac{1}{\rho}\frac{1}{g}\frac{\mathrm{d}p}{\mathrm{d}z}\mathrm{d}z = g\delta m \int_{0}^{z_1} \mathrm{d}z = g z_1 \delta m \tag{2.20}$$

This is precisely the potential energy of the precipitation removed. Hence, energy conservation in the column is achieved if the potential energy, as well as the enthalpy, of the precipitation is added to the surface budget. In our simplified model, the potential energy is implicitly converted to kinetic energy of falling precipitation, which is then dissipated as heat when the precipitation strikes the surface. Forget et al. (1998) also included the potential energy of precipitation in the convection scheme used in their study of CO_2 snowfall on Mars, but did not explicitly consider the way the inclusion of this term leads to energy conservation.

2.5 Treatment of Evaporation

Evaporation is most easily treated in terms of discrete layers, rather than trying to pass to the continuum limit. Evaporation from the surface reservoir of condensible adds condensible mass to the lowest layer of the atmosphere, increasing its gas-phase condensible content and also increasing its mass, and hence the pressure thickness Δp of the layer. The pressure of higher layers is not affected, though implicitly potential energy is being stored in higher layers since, viewed in z coordinates, the addition of mass to the lowest layer raises the altitude of all overlying layers, insofar as the added mass takes up space. Additional energy is stored in the lowest model layer in the form of the latent heat of the vapor added to the layer, which is equal to the energy lost from the planet's surface through evaporation.

Since the temperature dependence of the latent heat is taken into account, it may seem that the latent heat change during atmospheric condensation aloft is larger than the latent heat put into the atmosphere during surface evaporation of the same amount of mass. However, the thermal energy change on converting a mass δm_ℓ from vapor to liquid at temperature T is

$$\left[L(T) + (c_{pl} - c_{pc})T(p)\right]\delta m_\ell \tag{2.21}$$

Which reflects the loss of sensible heat from the vapor phase and the gain in the form of sensible heat of the condensate, as well as the latent heat of phase change. From Eq. 2.1 for the temperature dependence of the latent heat, the term in brackets is simply $L(0)$, which is independent of temperature. Hence, the *net* energy change from condensation or evaporation is independent of temperature; the difference between latent heat added near the surface and latent heat released aloft is accounted for in the sensible heat carried away by the precipitation.

CHAPTER 3

ONE-DIMENSIONAL SIMULATION WITH RADIATIVE-CONVECTIVE MODEL

We carry out three experiments using a 1D column model incorporating the convection scheme introduced in Chapter 2. The first two simulations verify that the convection scheme conserves energy and mass for both dilute and non-dilute cases. In the third simulation we apply the model to the atmosphere undergoing the runaway greenhouse on a planet with a high eccentricity orbit, and illustrates some additional features of convection in the nondilute limit.

3.1 Model Framework

The non-condensable substance in the model is the mixed N_2-O_2 air on Earth, and the mass of the non-condensable substance, unless otherwise noted, is $10^4\,\mathrm{kg\,m^{-2}}$, as in the present Earth's atmosphere. The condensable substance in the model is water. The moist convection scheme determines the level of the tropopause. We then calculate the level of the cold trap where the saturation concentration of water vapor reaches its minimum above the tropopause and assume uniform concentration above the cold trap and relative humidity of unity between the tropopause and the cold trap. This is equivalent to a simplified vertical diffusion scheme. The calculation is performed with a gravitational acceleration of $9.8\,\mathrm{m\,s^{-2}}$.

The column model uses a gray radiation scheme similar to that described in Merlis and Schneider (2010) in the longwave spectral region. As in Merlis and Schneider (2010), the absorption coefficient of water vapor is kept constant at $0.1\,\mathrm{m^2\,kg^{-1}}$, but unlike Merlis and Schneider (2010) we compute the water vapor optical thickness based on the actual water vapor path in the model, rather than an idealized profile. With the stated absorption coefficient, the effective radiating level is 0.98 hPa for pure water vapor atmosphere. Therefore, in order to resolve the radiative and convective process at high water concentrations, we choose

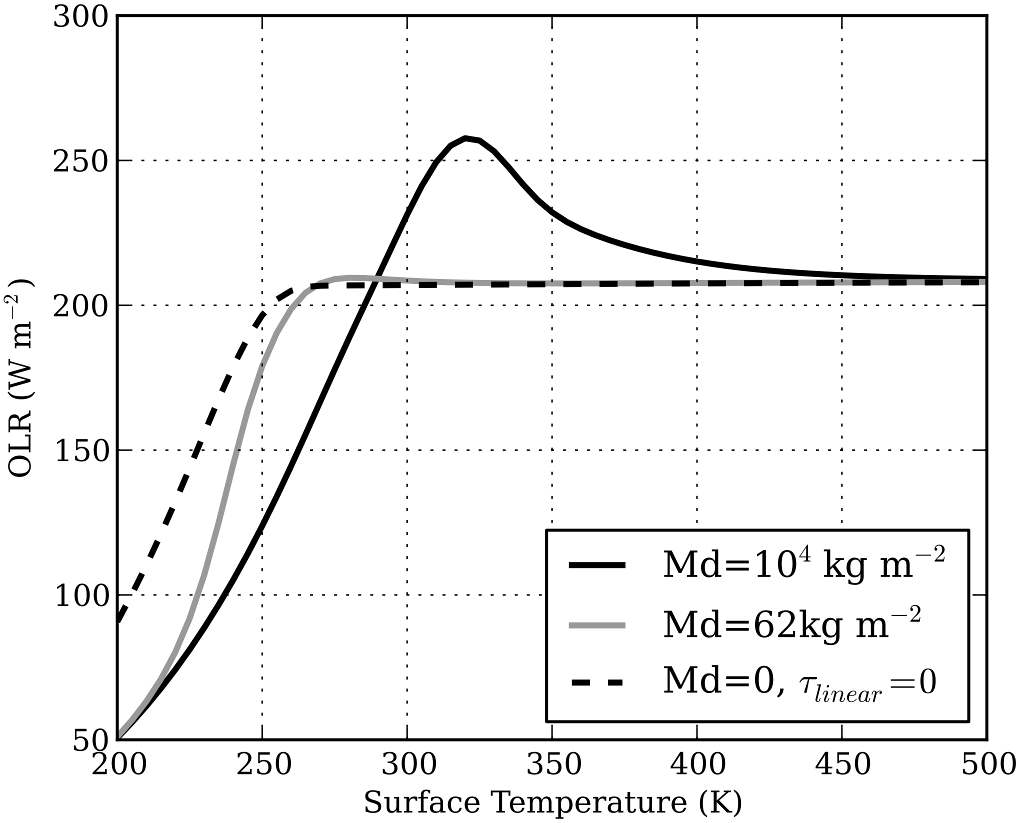

Figure 3.1: Outgoing Longwave Radiation (OLR) vs. surface temperature for a saturated moist adiabatic atmosphere using the same gray-gas radiation model as used in the calculations described in the text. M_{d} is the mass path of the noncondensible dry background gas. The two cases with nonzero M_{d} are calculated with background optical thickness $\tau_0 = 1.2$. The dashed line gives results for a pure water vapor atmosphere with no background temperature-independent opacity.

the level of 0.01 hPa as the top of the column model. In addition to the water vapor opacity, which varies with the water content (and hence temperature) of the atmosphere, the model includes a fixed background opacity which on its own would give the atmosphere a longwave optical thickness $\tau_0 = 1.2$. This can be thought of as the opacity due to a non-condensible trace gas in the atmosphere, such as CO_2. With these parameters the curve of the outgoing longwave radiation (OLR) as a function of the surface temperature exhibits overshoot for a saturated atmosphere, peaking at a value of $\mathrm{OLR}_{max} = 258\,\mathrm{W\,m^{-2}}$ at $T = 320\,\mathrm{K}$ before asymptoting to a value $\mathrm{OLR}_\infty = 210\,\mathrm{W\,m^{-2}}$ at high T (see Figure 3.1). Thus, if the absorbed stellar radiation is below 210 W m^{-2} the system can never enter a runaway greenhouse, and if it is above 258 W m^{-2} the system runs away regardless of the initial condition. For absorbed stellar radiation between 210 W m^{-2} and 258 W m^{-2} the system will runaway if initialized warmer than 320 K but will be attracted to a metastable non-runaway state if initialized cooler than 320 K.

We assume the atmosphere is transparent to the incoming stellar radiation. In reality the near-infrared absorption and Rayleigh scattering by water vapor molecules is very important when the water content in the atmosphere is high, but here we are chiefly interested in illustrating the behavior of the convection scheme, particularly with regard to vertical energy and moisture transport. The relevant phenomena are brought out most clearly in the idealized case in which incoming energy is deposited only at the surface.

The lower boundary of the column model is a heat reservoir with fixed thickness of 1 m and specific heat equal to that of liquid water. This lower boundary is included as a computational device to allow the surface energy budget to relax smoothly towards equilibrium; while it is mathematically identical to the common representation of an ocean mixed layer, it is not intended to represent either a shallow ocean or the mixed layer of an actual deep ocean. To represent an actual ocean layer, one would need to allow the depth to change in response to the mass budget, which is a simple modification, but an unnecessary complication in view of the use to which the heat reservoir is put in our model. At the surface, the sensible and latent heat fluxes are computed by standard drag laws assuming constant drag coefficients and surface wind velocity. The surface is also heated or cooled by absorption of the shortwave radiation transmitted through the atmosphere, and the net surface infrared flux (computed within the gray-gas model). The chief novel aspect of the surface budget in the nondilute case is that the enthalpy of the precipitation is added to the surface budget, as is the kinetic energy of the precipitation (after being converted to heat). In addition, surface pressure is updated by the net evaporation rate at the surface at the end of each time step.

The 1D simulations shown are carried out with 5 iterations per time step and a time step of 40 minutes in the dilute and runaway simulations, and 20 minutes in the equilibrium nondilute simulation.

3.2 Dilute Simulation

In the dilute simulation, we use the average shortwave solar flux absorbed by the Earth's climate system $S_0 = 238\,\mathrm{W\,m^{-2}}$ as the insolation and assume the albedo of the surface is zero. With the assumed background noncondensible opacity the equilibrium surface temperature in this simulation is similar to Earth's present tropics, and the system is therefore in the dilute regime.

We first check whether the convection scheme conserves energy. Both the net radiative flux at the top of the model and the net evaporation flux at the surface nearly vanish after integration of 3000 days, implying that the system reaches not only energy but also mass equilibrium (Figure 3.2a and 3.2b). The equilibrium profiles of air temperature and specific humidity are shown in Figure 3.2c and 3.2d. Below $\sim$200 hPa the atmosphere follows the moist adiabat, which defines the convective region. Above the tropopause, the atmosphere is in radiative equilibrium. Since there is no ozone in the column model, the upper atmosphere is nearly isothermal due to the gray gas assumption. The specific humidity at the surface is $\sim 2.08 \times 10^{-2}$ kg/kg, confirming that water vapor is dilute in this simulation.

The behavior of the convection scheme is shown in Figure 3.3. The troposphere is heated by the latent heat release and the convergence of sensible heat flux, except near the surface. In equilibrium, this heating is balanced by the radiative cooling in the troposphere. Near the surface, most of the sensible heat is transported upward and little condensation occurs, resulting in a cooling effect which is balanced by heat input from the surface (which is in turn heated by solar absorption). The maximal convective warming is located at $\sim$500 hPa, slightly higher than where most of the condensate forms.

In this 1D column model, the water vapor profile is only updated in the surface evaporation and convection scheme. Therefore, in the steady state, the water vapor concentration

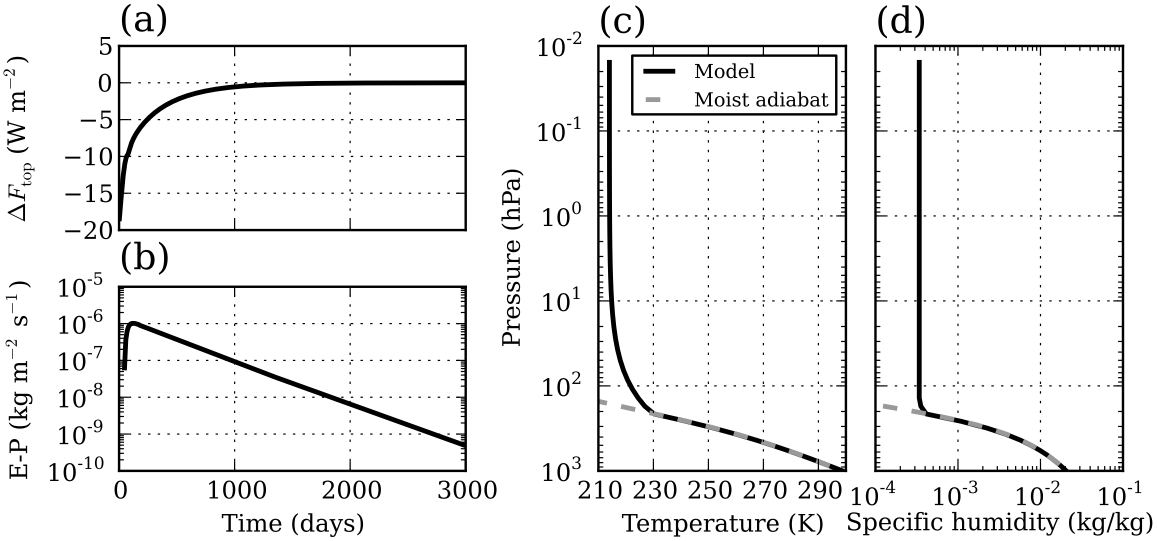

Figure 3.2: Time evolution of the net radiative flux at the top of the model (a) and the net evaporation flux at the surface (b) when insolation $S_0 = 238\,\mathrm{W\,m^{-2}}$, and the vertical profile of temperature (c) and specific humidity (d) when the column model reaches equilibrium. The dashed line in panel (c) gives the temperature on the moist adiabat and the dashed line in (d) gives the corresponding moisture in saturation.

does not change during the convective adjustment, except at the lowest model layer. In this layer, convective transport of moisture upward dries the layer (Figure 3.3b), which is balanced by moisture input from evaporation. An equivalent amount of water vapor then condenses out as air parcels rise in the atmosphere (Figure 3.3c), and falls to the ground, closing the mass budget of the climate system.

3.3 Nondilute Simulation

With an Earthlike noncondensible inventory and $\tau_0 = 1.2$, the atmosphere does not become strongly nondilute until the stellar flux is sufficiently high to cause a runaway, in which case the system does not reach equilibrium. In order to illustrate strongly nondilute convection in equilibrium, one could increase τ_0 with fixed stellar flux, or keep τ_0 at its original value while reducing the noncondensible inventory. Here we choose the latter approach, and raise the water vapor concentration in the 1D model by reducing the mass of the dry air to $62.10\,\mathrm{kg\,m^{-2}}$. In this case, the atmosphere can be non-dilute even at freezing point of water

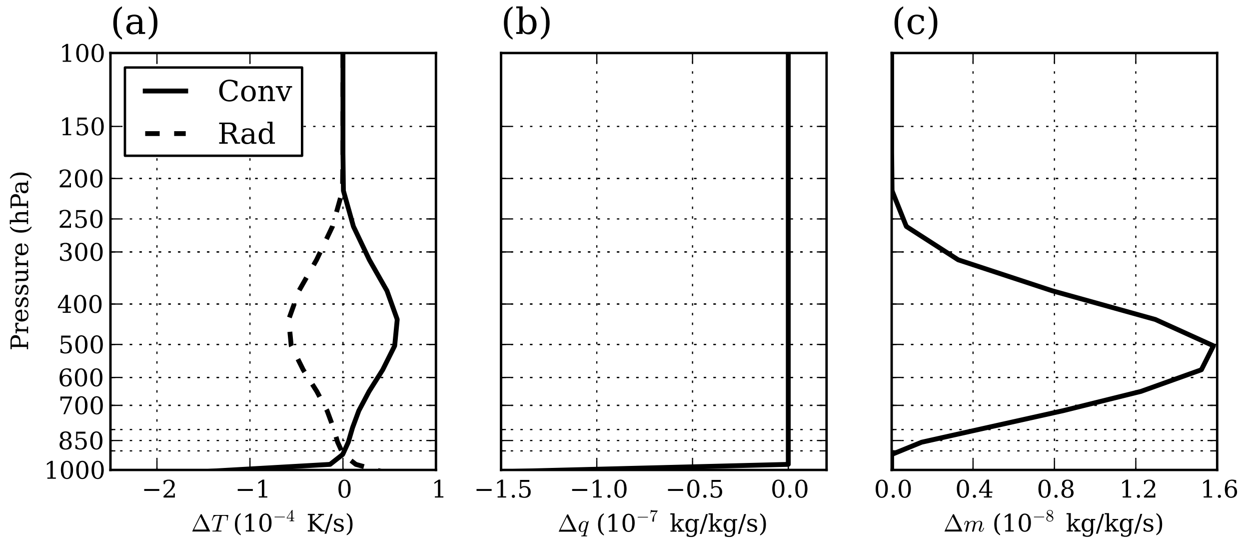

Figure 3.3: The rate of change of air temperature (solid line in a) and specific humidity (b), and the condensation rate of water (c) during the convective adjustment when the column model reaches equilibrium for $S_0 = 238\,\mathrm{W\,m^{-2}}$. The dashed line in (a) shows the radiative cooling profile. Near the surface, both the air temperature and specific humidity decrease during the convective adjustment primarily due to the upward transport of sensible heat and moisture.

since the saturation vapor pressure of water in the atmosphere only depends on the air temperature. This provides a simple and clean test of energy and mass conservation in the nondilute case. With reduced noncondensible pressure, the curve $\mathrm{OLR}(T_s)$ shows very little overshoot; OLR_∞ is the same as in the previous case, as it is determined by the limiting case of a pure water vapor atmosphere (see Figure 3.1). The absorbed stellar flux in this case was set at $208.5\,\mathrm{W\,m^{-2}}$, which is just short of the value at which the system enters a runaway state.

In this nondilute case, the system reaches both energy and mass equilibrium after integration of 3000 days (Figure 3.4a and 3.4b). The net evaporation rate at the surface approaches zero exponentially with time, similar to the dilute case (Figure 3.2b). However, the net radiative flux at the top of the model evolves somewhat more slowly compared with the dilute simulation (Figure 3.2a). This is related to the high climate sensitivity of water-rich atmospheres, i.e. the low slope of OLR as a function of surface temperature. Figure 3.4c and 3.4d show the equilibrium temperature and humidity profiles. The convection is so deep that

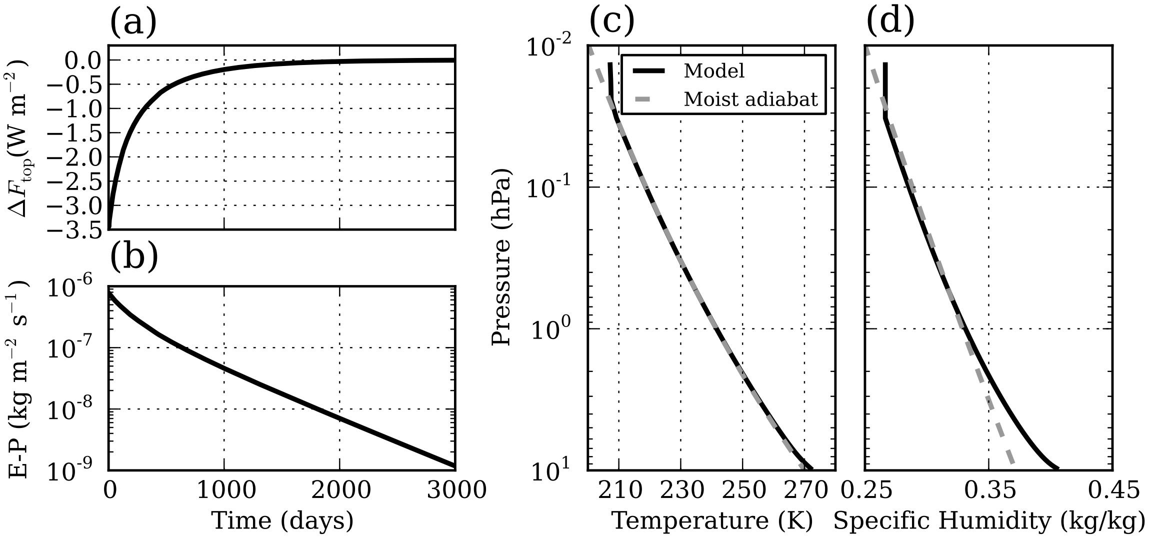

Figure 3.4: Same as Figure 3.2, but for non-dilute case with the dry air mass of $62.10\,\mathrm{kg\,m^{-2}}$ and the absorbed stellar flux of $208.5\,\mathrm{W\,m^{-2}}$, and all other parameters kept the same as in the dilute simulation.

it establishes a moist adiabat nearly throughout the column atmosphere. The tropopause is close to the top of the column model, $\sim 0.03\,\mathrm{hPa}$. The humidity profile confirms that water vapor is non-dilute in the atmosphere. Corresponding to the thermal structure, the vertical distribution of the specific humidity becomes more uniform compared with the dilute case. Even at the top of the model, the specific humidity is as high as 0.27 kg/kg. In addition, the surface pressure in equilibrium is about 9.75 hPa (Figure 3.4c and d), so that the mass of water in the atmosphere is ~40 kg, approximately two thirds of that of the dry air. The humidity near the ground is slightly in excess of the value associated with the saturated moist adiabat, but this does not actually arise from supersaturation in the convection scheme. Rather, the excess moisture arises from the fact that the temperature profile is very slightly warmer than the moist adiabat, and that the saturated specific humidity is very sensitive to temperature when the noncondensible inventory is so low.

The vertical structure of condensation and convective heating for nondilute convection will be discussed in connection with the runaway greenhouse simulation.

3.4 Runaway Greenhouse and Seasonal Cycle Simulation

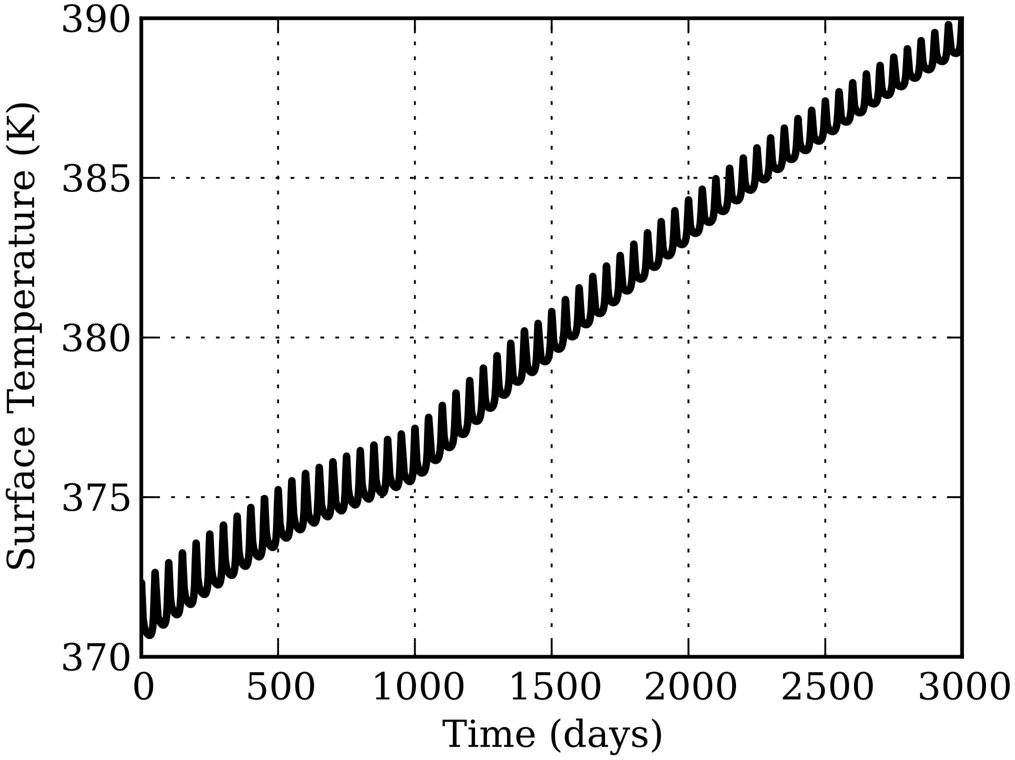

Figure 3.5: Time evolution of the surface temperature in the runaway greenhouse simulation. The seasonal cycle of the surface temperature is very weak ($\sim$1.5 K) despite the highly eccentric orbit assumed.

To test how the moist convection scheme behaves for time-dependent simulations, we use the 1D column model to simulate the runaway greenhouse atmosphere on a planet with a high eccentricity ($e = 0.5$). The orbital period of the planet in this simulation is 50 days, and the stellar flux at the distance equal to the semi-major axis of the orbit is $238\,\mathrm{W\,m^{-2}}$. Hence, the average of the stellar flux received by the planet over the course of the planetary year is $238/\sqrt{1-0.5^2} = 274.82\,\mathrm{W\,m^{-2}}$, which is sufficiently high to force the system into a runaway. Kepler's Second Law indicates that the planet travels slowly near the apastron (winter) and rapidly during periastron (summer), which would lead to short, hot summers and long, cold winters on a planet with little thermal inertia.

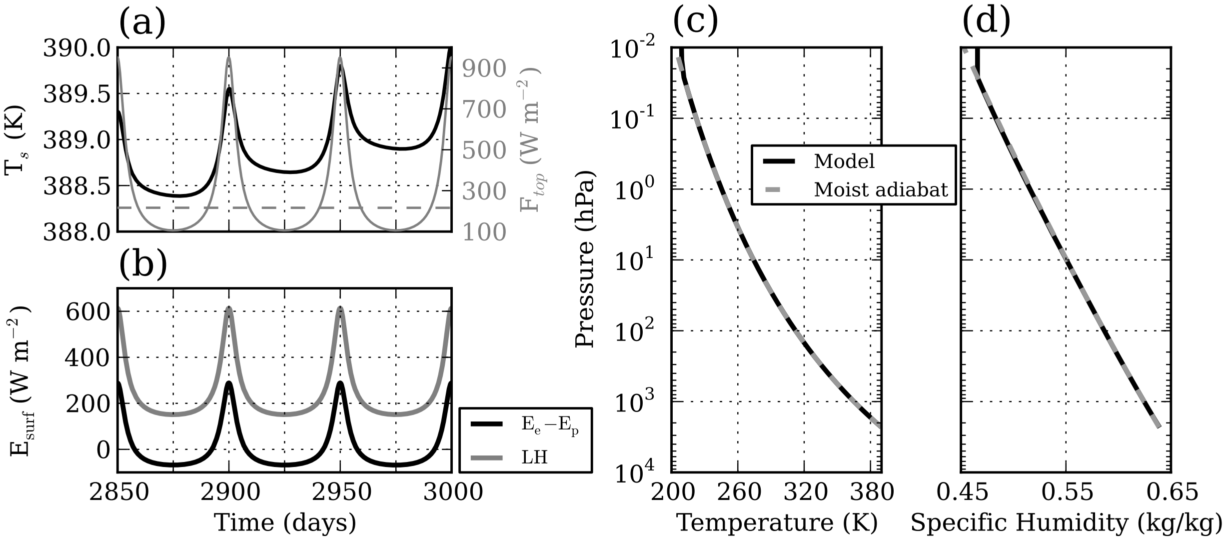

Figure 3.6: (a) Time evolution of the surface temperature (black solid), the global mean stellar flux received by the planet (gray solid) and the outgoing longwave radiation (gray dashed) for last 150 days of the runaway greenhouse simulation. (b) Time evolution of the energy flux associated with mass exchange between the surface and the atmosphere ($E_\mathrm{e} - E_\mathrm{p}$, black) and the latent heat flux due to surface evaporation (gray) for the same time period as in (a). (c) The vertical profile of air temperature on day 3000. (d) The vertical profile of the specific humidity on day 3000.

We integrated the model for 3000 days starting from an initial surface temperature of 372 K. The surface temperature evolution over this time period is shown in Figure 3.5. The temperature exhibits a steady upward trend rising by $\sim$ 20 K over the course of the integration, with only a small superposed seasonal cycle. Because the annual mean OLR (Figure 3.6a) remains near the limiting value of 210 W m^{-2}, which is less than the absorbed solar radiation, the planet is in a runaway state and the temperature will continue to grow indefinitely so long as a liquid ocean remains to feed the increasing atmospheric water content. Because the surface temperature response shows only a weak seasonal cycle, the runaway conditions are little affected by the strong seasonal cycle of insolation, even though the planet undergoes a long winter with stellar flux as low as 100 W m^{-2} (gray solid line in Figure 3.6a). If it were not for the evidently strong thermal inertia of the system much of the water vapor evaporated in summer would condense back onto the surface in the long winter.

The detailed response of the surface temperature to the large seasonal stellar forcing is shown in Figure 3.6a. The surface temperature varies by only 1.5 K, in spite of large stellar flux variation from $900\,\mathrm{W\,m^{-2}}$ to $100\,\mathrm{W\,m^{-2}}$ and small surface thermal inertia (recall that the thickness of the slab ocean is only 1 m). The surface energy budget in the 1D model is

$$\frac{\mathrm{d}(\rho_w c_{pw} H T_s)}{\mathrm{d}t} = -SW - LW - SH - LH + (E_p - E_e) \tag{3.1}$$

Here, ρ_w and c_{pw} are the density and specific heat of liquid water respectively, $H = 1\,\mathrm{m}$ is the thickness of the slab ocean, SW and LW are the net shortwave and longwave radiative fluxes (positive when going upward), SH and LH are sensible and latent heat fluxes at the surface respectively, E_p is the energy loss of the atmosphere when the condensate falls to the ground (equivalent to the sum of the internal energy and potential energy of the precipitated water, or the static energy of the precipitated water), and E_e is the energy increase of the atmosphere when water goes into the atmosphere by evaporation (equivalent to the sum of the internal energy and potential energy of the evaporated water, or the static energy of the evaporated water). In the runaway greenhouse simulation, both LW and SH are small because the surface air temperature stays very close to the surface temperature and the atmosphere is optically thick for longwave radiation near the ground. Hence, the absorbed stellar radiation is nearly balanced by the energy flux associated with the phase transition of water ($LH + E_e - E_p$, see Figure 3.6b). Therefore, most of the stellar flux is used to change the mass of the atmosphere instead of the surface temperature. The phase transition of water strongly damps temperature fluctuations, as it takes only a small change in surface temperature to drive a large change in the energy fluxes associated with water when the water content of the atmosphere is so high. Hence the planet exhibits very weak seasonal cycle in spite of its high eccentricity orbit. Note that $E_e - E_p$ is of comparable magnitude to the latent heat flux, so that this term makes up a crucial part of the exchange of energy between surface and atmosphere in the strongly nondilute case.

Although the thermal inertia associated with phase change strongly damps the seasonal cycle, it is easy to verify from a simple energy balance argument that this thermal inertia does not cause a significant delay in transfer of water from the ocean to the atmosphere. For very hot conditions, the atmospheric energy storage is dominated by water vapor. As an upper bound, let's estimate the energy of a saturated atmosphere with surface temperature and pressure at the critical point of water, beyond which point the distinction between ocean and atmosphere disappears. The mass of the atmosphere per unit area of planetary surface is p_{crit}/g, where p_{crit} is the critical point pressure. As an upper bound to latent heat storage, we multiply by the latent heat L at 1 bar and 373 K, which overestimates the latent heat storage because in reality L approaches zero as the critical point is approached (an effect not currently incorporated in our convection scheme). Besides the latent heat storage, the atmosphere stores dry enthalpy at a rate c_pT per unit mass, where T is the mass-weighted temperature of the atmosphere. As an upper bound to this, we take $T = T_{crit}$, which is not a bad approximation given the slow logarithmic decay of $T(p)$ for a pure steam atmosphere. The estimated energy storage per unit area is then $E = (L + c_pT_{crit})p_{crit}/g$ which works out to $8 \times 10^{12}\,\mathrm{J\,m^{-2}}$ for Earthlike gravity, with specific heat taken at the critical point. The net flux available to allow this energy to accumulate is the difference between the incoming stellar radiation and the OLR_∞, which is $64\,\mathrm{W\,m^{-2}}$. Dividing this into E, the time needed to reach the critical point is under 4000 Earth years, which is short compared to the other processes involved in irreversible water loss. The time required to reach the critical point becomes infinite as the absorbed stellar flux approaches OLR_{crit}, but even reducing the excess flux by a factor of 100 would not bring the thermal inertia delay into the range where it can be considered a significant inhibition to the runaway greenhouse process.

The vertical structure of the temperature and specific humidity on the last day of simulation is shown in Figure 3.6c and 3.6d. For the runaway greenhouse simulation, water vapor is non-dilute in the atmosphere. Similar to the non-dilute simulation in Section 3.3, essentially the whole atmosphere is subject to convective adjustment. As the surface temperature reaches 390 K, water vapor is non-dilute even in the upper atmosphere above 10 hPa, leading to large infrared opacity there. In contrast to the the dilute simulation discussed in Section 3.2 (Figure 3.3), condensation and convective heating are concentrated in a thin layer in the upper atmosphere, from 0.1 hPa to 10 hPa (Figure 3.7). This is in part due simply to the optical thickness of the atmosphere, which implies that the strong radiative cooling needed to balance the latent heat release due to strong condensation can only occur in the high portions of the atmosphere where the atmosphere first begins to become optically thin, and from which infrared can escape to space. However, a full understanding of the situation in the nondilute case requires some discussion of vertical motion and buoyancy generation, which exhibit key differences from the dilute case, which will be discussed in the next section.

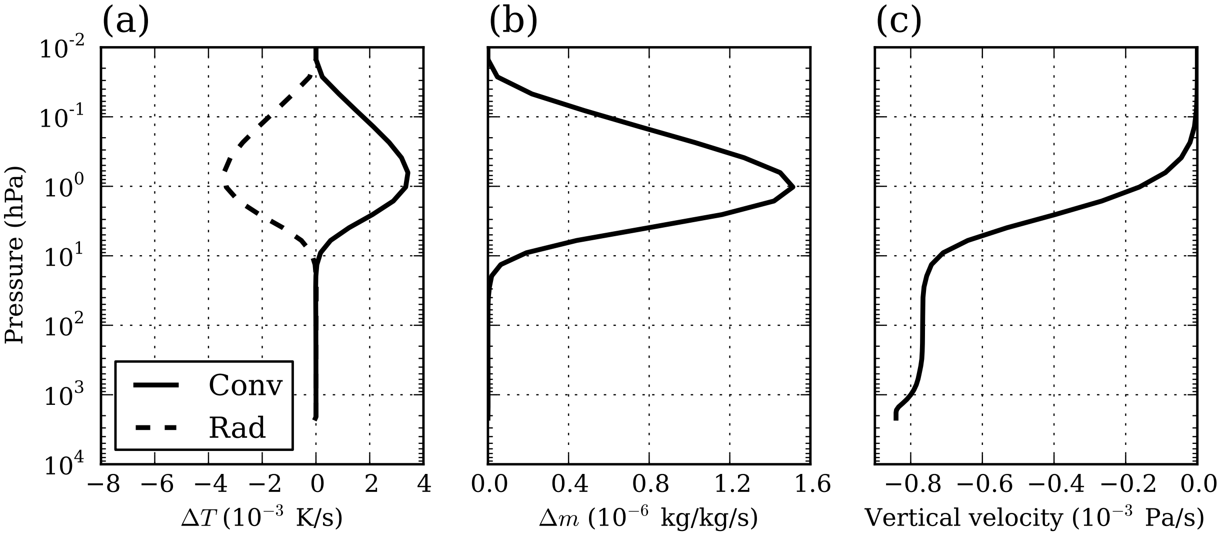

Figure 3.7: (a) Heating rate due to convection (solid) and radiation (dashed). (b) Condensation rate of water. (c) Vertical velocity due to the removal of the condensed water from the atmosphere. All data is from the runaway greenhouse simulation on day 3000.

3.5 Discussion

3.5.1 Vertical Motion Induced by Precipitation

The fact that precipitation carries a significant mass flux has important implications for the vertical motion of the gas phase part of the atmosphere in the nondilute case. Vertical motion is diagnosed from the continuity equation. In the nondilute case, the continuity equation needs be modified taking the mass loss due to precipitation into account. Specifically, assuming the hydrostatic approximation,

$$\partial_p \omega + \nabla \cdot (\boldsymbol{v}) = P \tag{3.2}$$

where $\boldsymbol{v}$ is the horizontal velocity and P is the rate of mass precipitation, per unit mass of the atmosphere. This is also the form the continuity equation would take when incorporating the convection scheme into a nondilute 3D general circulation model. This effect is included in Leconte et al. (2013) in their study of the runaway greenhouse threshold of the Earth's climate system. Integrating the continuity equation from the top of the atmosphere shows that a vertical motion is induced when the condensate is removed from the atmosphere (ω_2 in Eq.(3.3)).

$$\begin{aligned} \omega(p) &= \omega_1 + \omega_2 \\ \omega_1 &\equiv - \int_0^p \nabla \cdot \boldsymbol{v}_p \, \mathrm{d}p \\ \omega_2 &\equiv \int_0^p P \, \mathrm{d}p \end{aligned} \tag{3.3}$$

Here ω_1 comes from the air flow divergence above the pressure level, $\boldsymbol{v}_p = (u, v)$ is the horizontal wind velocity along the isobaric surface and vanishes in the 1D model simulation since there is no horizontal flow; this term would be present in a 3D model. In the dilute limit there would be no mean vertical motion in an isolated 1D column, but in the nondilute case a mean gaseous vertical motion ω_2 is supported by the downward mass flux of precipitation. Figure 3.7c shows the vertical velocity ω_2 due to the removal of condensed water from the atmosphere for the runaway greenhouse simulation, and indicates that some condensation also occurs between the 1 bar level and the surface. In this layer, the latent heat release is balanced by the adiabatic cooling due to the upward motion. For our single column model, the way that the vertical mass flux is balanced by a return mass flux in the form of precipitation can be considered as a peculiar form of one-column Hadley cell, in which the return mass flow compensating the upward motion in the convecting column is balanced by downward mass flux due to precipitation. For a conventional Hadley cell, the upward mass flux consists primarily of noncondensible gas, and must be balanced instead by downward noncondensible mass flux in adjoining subsiding regions, which leads to compressional heating there. The magnitude of vertical motion in the optically thick nondilute case is small, however, compared with the typical large-scale vertical velocity in the ITCZ of present Earth ($\sim$0.1 Pa s^{-1}). It is important to note that the transport of moisture and heat due to ω_2 does not need to be incorporated in the column model or 3D general circulation model as an explicit vertical advection term. This transport is handled implicitly as part of the convective adjustment process. Specifically, it is manifest as the change in pressure that occurs in a layer when mass is removed from a higher layer by precipitation.

3.5.2 Buoyancy Generation in Dilute vs. Nondilute Atmospheres

In the dilute limit, absorption of stellar radiation at the surface heats the low-lying air, which then picks up moisture from the adjacent surface; this builds buoyancy near the surface, leading to deep convection which takes the form of condensing plumes penetrating deep into the atmosphere. In the highly nondilute limit, in contrast, it is not possible to create buoyancy in this way, because the saturated moist adiabat collapses onto a unique curve without free parameters – the dewpoint/frostpoint formula obtained by solving the Clausius-Clapeyron relation for $T(p)$ – which is neutrally stable with regard to pseudoadiabatic vertical displacements. In contrast, in the dilute limit, the lower atmosphere can be heated to a *different* member of the moist adiabatic family of profiles, which is buoyant with regard to the overlying atmosphere. In the strongly nondilute case, heating the lower atmosphere increases surface pressure instead of buoyancy, in effect adding non-buoyant mass at the bottom of the atmosphere. Similarly, it is difficult to generate top-driven convection through production of negative buoyancy by radiative cooling in the upper atmosphere, because the energy loss goes into atmospheric mass loss via precipitation, which reduces surface pressure rather than generating negative buoyancy aloft. (Retention of condensate would alter this conclusion.) The lack of buoyancy generation in single-component condensible atmospheres was noted in Colaprete and Toon (2003) in connection with saturated pure-CO_2 Martian convection, but is in fact a generic property of nondilute convection.

	dilute	non-dilute	runaway (summer)	runaway (mean)
Surface temperature (K)	306.29	279.89	390.04	388.85
$E_p - E_e$ ($\mathrm{W\,m^{-2}}$)	-2.75	2.91	-288.87	-3.89
Precipitation rate ($10^{-5}\,\mathrm{kg\,m^{-2}\,s^{-1}}$)	5.82	6.12	8.58	9.48
$\Delta F_{\mathrm{top}} - \Delta F_{\mathrm{bottom}}$ ($\mathrm{W\,m^{-2}}$)	186.23	150.25	190.02	200.94
f(water) (kg/kg)	0.980	0.596	0.352	0.359
q_{sa} (kg/kg)	0.021	0.405	0.638	0.631

Table 3.1: Surface temperature, the energy flux associated with mass exchange between the atmosphere and surface ($E_p - E_e$), precipitation rate, the longwave radiative flux leaving the air column ($\Delta F_{\mathrm{top}} - \Delta F_{\mathrm{bottom}}$), f(water) and the specific humidity of the surface air (q_{sa}) for the dilute, non-dilute and runaway greenhouse simulations, respectively. For the runaway case, values are given both for the summer at day 3000 of the simulation, and for the average over the last seasonal cycle. The ratio f(water) measures the portion of water vapor transported upward from the lowest layer by the moist convection relative to the total evaporated water added to the layer by the surface evaporation.

Our single-column simulations shed some further light on how nondilute moist convection works in the absence of buoyancy generation. Table 3.1 gives the ratio of the water vapor transported upward from the lowest layer during moist convection to the total evaporated water added to the layer during surface evaporation, which measures the buoyancy of the atmosphere during moist convection. This ratio is smaller than unity. The remaining part stays in the lowest layer, increasing the mass of the atmosphere, with negligible amounts condensing out there (see Figure 3.3c and Figure 3.7b). In our simulations, this ratio is nearly the same as the mass concentration of non-condensable substance in the near surface layer (1-q_{sa}), as shown in the table. This simple relationship is confirmed by numerical simulations with a variety of different surface air specific humidities ($0 < q_{sa} < 0.95$, not shown). For the Earth-like atmosphere where water vapor is dilute, nearly all of evaporated water vapor is transported upward and forms precipitation in the mid-troposphere, releasing latent heat that balances the IR cooling there (Figure 3.8a). The column model indicates that the buoyancy of the atmosphere is getting weaker as water vapor becomes dominant in the atmosphere, with less vertical transport by deep convective plumes that nearly instantly mix water vapor throughout the depth of the troposphere. The evaporated water vapor tends to mostly stay in the lowest layer.

In the runaway simulation, where the mass of the atmosphere is steadily increasing, most of the evaporated water does indeed simply stay where it is put, at the bottom of the atmosphere. In an equilibrium situation such as the cold nondilute simulation with reduced noncondensible pressure, the surface pressure eventually stops growing, and so the mass added to the lowest model layer by evaporation must be carried away by some other means than deep convection. The answer lies in the advection due to the vertical velocity ω_2, which carries moisture just a little ways upwards from the lowest layer, rather than distributing it through the depth of the troposphere as deep convection would do. The equilibrium mass budget in strongly nondilute convection consists of addition of moisture to the bottom of the atmosphere by evaporation, which is then advected upward to the layer where the mass can condense out and return to the surface as precipitation. From the standpoint of energetics, the reduction in surface pressure due to precipitation must balance the increase due to evaporation because condensation is determined by infrared radiative cooling to space, while evaporation is determined by absorption of stellar radiation at the surface, and the two energy fluxes must balance in equilibrium. The contrast between dilute and nondilute moist convection is summarized in Figure 3.8. In the nondilute case convection takes the form of a "moisture elevator" in which moisture added at the surface ascends the floors of the atmosphere in an orderly and gradual process, in contrast to the chaotic, turbulent process by which deep convection transports moisture in the dilute case. In the nondilute case, a mean vertical motion can exist in a single column, with the upward vapor-phase mass flux balanced by downward mass flux from precipitation and the condensational heating is balanced locally by radiative and adiabatic cooling; this is another manifestation of the single-column Hadley circulation described previously. For the dilute case, in contrast, any mean upward motion in a column can still balance condensational heating against adiabatic cooling by ascent locally, but the upward noncondensible mass flux must be compensated by subsidence in the surrounding air, which leads to compressional heating that must be balanced by radiative cooling there.

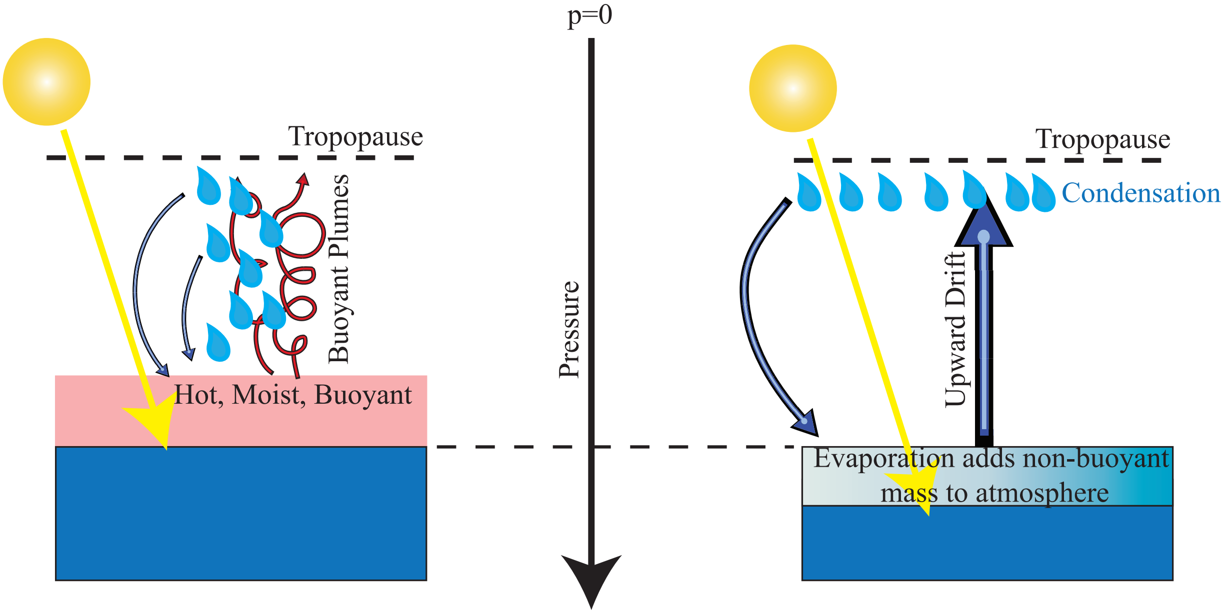

Figure 3.8: Schematic of moist convection in Earthlike conditions with a dilute atmosphere that is not optically thick throughout the infrared (left) and for a strongly nondilute optically thick atmosphere (right). In the Earthlike case, shortwave stellar energy absorbed at the ocean surface leads to the creation of a hot moist layer of air near the surface, which is buoyant with respect to the overlying atmosphere and results in deep convection. In the strongly nondilute case, stellar heating instead adds mass to the bottom of the atmosphere in the form of condensible vapor. Because of constraints related to Clausius-Clapeyron, the new mass added is not buoyant with regard to the overlying atmosphere, and is only gradually carried upward by gradual laminar ascent, to upper layers of the troposphere where the latent heat released by rapid condensation can be balanced by infrared cooling to space.

3.5.3 Energy Transport by Precipitation, and Precipitation-Temperature Scaling

The significant energy carried by precipitation is one of the novel features of nondilute convection. For present Earth's climate, even though the precipitation rate is trivial compared with the mass of the atmosphere, E_p is a large value. For a typical value of precipitation rate in the tropics ($5 \times 10^{-5}\,\mathrm{kg\,m^{-2}\,s^{-1}}$), E_p is as high as $50\,\mathrm{W\,m^{-2}}$. Table 3.1 shows $(E_p - E_e)$ for the three simulations discussed previously. The column for the dilute simulation, which is carried out in Earthlike conditions, shows that even though most of E_p is canceled by the internal energy of the liquid water evaporated from the surface, the remaining part $(E_p - E_e)$ is still not entirely negligible, attaining a value of approximately $-2.75\,\mathrm{W\,m^{-2}}$. For the cold nondilute simulation with reduced noncondensible mass, the value gets slightly larger in magnitude and changes sign. The change in sign arises primarily because the precipitation is warmer, owing to the weaker vertical gradient of temperature in the nondilute case. Even in the hot runaway case, the seasonal mean value only increases modestly in magnitude, to $-3.89\,\mathrm{W\,m^{-2}}$. The modest values of $E_p - E_e$ trace back to the fact that the precipitation rate is similar in all three cases, with only moderate increases even in the hot runaway case. In equilibrium or near-equilibrium, this limits the mass available to carry energy. In the course of the seasonal cycle, however, the exchange term can be very large, as evidenced by the summer runaway value in Table 3.1. In that case, $E_p - E_e$ is comparable to the absorbed solar flux at the surface. In our idealized calculation, all the energy carried by the precipitation is deposited at the ground, but in reality some proportion would be transferred to the atmosphere by evaporation and frictional dissipation on the way down.

The limited precipitation rate noted above arises from energetic limitations already familiar from studies of Earth's climate. Because of limitations on turbulent transfer of sensible heat through a stable boundary layer, the net evaporation (and hence, in equilibrium, net precipitation) cannot much exceed the stellar radiation reaching the surface (Pierrehumbert, 2002; Hir et al., 2009). For the runaway case the limit is $1.1 \times 10^{-4}\,\mathrm{kg\,m^{-2}\,s^{-1}}$, only slightly in excess of the realized precipitation. Another way of looking at the energetics is that the dominant balance in the troposphere when sufficiently large amounts of condensible substance is present is between latent heat release and net radiative cooling (which is purely infrared in our case). The column-integrated radiative cooling is shown in Table 3.1. It accounts well for the precipitation in the two optically thick nondilute cases, translating into a precipitation rate of $6.07 \times 10^{-5}\,\mathrm{kg\,m^{-2}\,s^{-1}}$ in the cold nondilute case and $9.04 \times 10^{-5}\,\mathrm{kg\,m^{-2}\,s^{-1}}$ in the runaway case. The radiative cooling limit significantly overestimates the precipitation in the dilute case, however, because in that case much of the radiative cooling is balanced instead by sensible heat transport due to convection.

3.5.4 Convective Adjustment Criterion

The convection scheme we have developed adjusts the atmosphere to a saturated pseudoadiabat, using the lapse rate in comparison to the nondilute pseudoadiabat as the sole criterion for convection. This achieves an equivalent of what is commonly done in single-column radiative-convective models, and thus leads the way for general circulation model experiments focusing on dynamical effects in nondilute atmospheres. When dealing with a situation presenting the novel physics of nondilute convection, it is useful to revert to simplified schemes such as this which are easy to understand, and which can most easily be made to incorporate the most fundamental physical constraints. This approach complements approaches such as that pursued by Wolf and Toon (2015), in which an attempt is made to adapt the complex Zhang-Macfarlane convection scheme – which incorporates many empirical assumptions based on Earth's current atmosphere – to nondilute conditions. However, unconditional convective adjustment to a pseudoadiabat does not necessarily represent the way convection operates in reality. There are many potentially important physical effects that have not been taken into account. Among other things, the derivation of the convection scheme has revealed a currently unconstrained parameter governing the distribution of condensate following convection, and there is currently no good physical basis for setting this parameter. In addition, more work is needed on the actual behavior of the shallow nonprecipitating convection that occurs when there is insufficient condensible to allow the adjusted state to be saturated, and on schemes that in general allow the adjusted state to be subsaturated. Further, given possibly strong contrasts between the molecular weight of the condensible and that of the background gas, there is a need to incorporate compositional effects on buoyancy into the parameterization, along the lines explored for $H_2 - H_2O$ atmospheres by Li and Ingersoll (2015). Such effects would be particularly extreme for H_2 atmospheres incorporating condensible CO_2 from a surface CO_2 ocean or glacier, and would yield stable layers near the ground that are highly resistant to the initiation of convection. Some insights may be gained by studying convection in nondiute atmospheres in the Solar System – notably those of Mars and Titan – but it is likely that further development of nondilute convection parameterizations will need to be informed by simulations with resolved three-dimensional convection/cloud simulations.

CHAPTER 4

THREE-DIMENSIONAL SIMULATION ON FAST ROTATING PLANETS

4.1 Introduction

Although 1D single-column model is a useful tool to explore the basic feature of moist convection, it can only simulate the global mean climate, but tells nothing on the 3D dynamics of the atmosphere (e.g., the energy and mass transport in the atmosphere) that is essential to understanding the climate dynamics of condensible-rich atmospheres. In fact, sometimes 1D radiative-convective calculations have to make certain assumptions to include the 3D dynamics of the atmosphere, e.g., choosing a reference relative humidity profile to reflect the sub-saturation in the troposphere as in Manabe and Wetherald (1967) and Kasting and Ackerman (1986). In this chapter, we begin with some analytical results on the nature of nondilute climates, and then we show how some of these features are manifest in numerical simulations in a 3D general circulation model incorporating the 1D radiative-convective calculation introduced in Chapter 3.

4.2 Analytic Results on Nondilute Atmospheres

4.2.1 WTG and Barotropic Nature of Strongly Nondilute Circulations

One of the key properties of nondilute atmospheres which we will demonstrate is that they are characterized by weak horizontal temperature gradients. Therefore, it is useful to examine other dynamical regimes which produce weak temperature gradients without relying on nondilute physics. Loosely speaking, at latitudes where the effective Coriolis force is weak, temperature gradients are also weak because the pressure gradients associated with strong temperature gradients cannot be balanced by the Coriolis forces produced by winds of a magnitude compatible with other dynamical constraints (e.g. angular momentum conservation). The Coriolis parameter giving the local effect of rotation is $f = 2\Omega \sin\phi$ where Ω is the angular rotation rate of the planet and ϕ is the latitude. Thus, the weak gradient behavior always applies near the equator, and indeed this forms the basis of the standard conceptual model of the Earth's tropical circulation (see Williams et al. (2009) for a summary of the ideas and their history). For a slowly rotating planet, the weak temperature gradient (WTG) approximation holds globally. This regime is of particular importance for tidally locked planets about low-mass stars, since tide-locking can occur in long-period orbits in that case, and in particular within the conventional habitable zone of M-dwarf stars. The application of WTG in this regime was elaborated in Pierrehumbert (2011). Some attempts at formulating criteria for WTG validity based entirely on externally imposed parameters are presented in Perez-Becker and Showman (2013) and Koll and Abbot (2016).

Generally speaking, in completely dry or dilute atmosphers, WTG cannot be sustained globally by atmospheric dynamics when the planet is fast rotating ($a^2/L_{R_O}^2 \gg 1$, where a is the radius of the planet and L_{R_O} the the equatorial Rossby deformation radius) or when the the planet rotates slowly but with a radiative cooling timescale shorter than the timescale for the subsidence in the atmosphere. It is abundantly clear that dilute atmospheres on rapid rotators support strong temperature gradients, as in Earth's extratropics. What is the situation for nondilute rapid rotators?

For sufficiently rapid rotators, the atmospheric flow will be in geostrophic balance. For geostropically balanced flow, the thermal wind relation links vertical gradients in wind to horizontal density gradients taken on an isobaric surface. Specifically introduce a local Cartesian coordinate system (x, y) on a pressure surface, and let u be the wind in the x direction. Then the thermal wind relation states

$$\frac{\partial u}{\partial p} = \frac{1}{pf}\frac{\partial \overline{R}T}{\partial y}\bigg|_p \tag{4.1}$$

where $\overline{R}$ is the gas constant for the mixture of condensible and noncondensible gas at each point and f is the local Coriolis parameter. However, we know that in the saturated steam atmosphere limit, $T = T(p)$, i.e. temperature is uniform on isobaric surfaces within the saturated part of the atmosphere. Moreover, in a pure steam atmosphere $\overline{R} = R_c = const.$. Eq. 4.1 then implies that the wind is independent of height, and that the dynamics is barotropic. In consequence, strongly nondilute saturated atmospheres will tend to have nearly barotropic dynamics. They will have weak horizontal temperature gradients on pressure surfaces, even if the planet rotates rapidly.

Note that the above result assumes saturation. Strongly subsaturated atmospheres, even if pure steam, can be baroclinic. Hence the factors determining subsaturation also have a major effect on the dynamics of the atmosphere. We will see some examples of the behavior of subsaturation in 3D nondilute atmospheres in Section 4.4.4.

The barotropic nature of the system does not in itself preclude the existence of strong temperature gradients at the planet's surface (if it has one), because the planetary surface is not an isobaric surface. The surface pressure gradients are equal to the pressure gradients aloft, and geostrophically balance the barotropic winds. Differential stellar heating of the planet's surface would lead to surface temperature gradients, just as the Earth is generally colder at the poles than at the equator. On a planet with a surface condensible reservoir, these temperature gradients would lead to corresponding surface pressure gradients via the Clausius-Clapeyron relation.

In a dilute rapidly rotating atmosphere like the Earth's, baroclinic instability acts to weaken temperature gradients in midlatitudes and the Hadley cell weakens them in the tropics. For the saturated strongly nondilute case, the dynamics is barotropic, so baroclinic eddies cannot play a role in transporting heat. Hadley cells cannot be sustained in the saturated strongly nondilute atmosphere either, due to the strong constraint by the Clausius-Clapeyron relation. However there are a number of other mechanisms that can act to wipe out surface temperature and pressure gradients in a nondilute atmosphere.

4.2.2 Mechanisms of Horizontal Homogenization of Temperature

Barotropic Adjustment

Suppose that differential stellar heating of a planet gives rise to a latitude-dependent surface temperature $T_s(\phi)$. On a planet with a global surface reservoir of condensible, this will give rise to a surface pressure $p_s(\phi) \approx p_{\mathrm{sat}}(T_s(\phi))$ if the planet is warm enough for the atmosphere to be dominated by the condensible. Because of the exponential dependence of saturation vapor pressure on temperature, a small surface temperature gradient translates into a large surface pressure gradient, and hence (by geostrophic balance) a very large barotropic wind. Unless the temperature gradient is sufficiently small, the resulting jet will be barotropically unstable, and the resulting instability will act to weaken the jet and to redistribute mass such that the surface pressure and temperature gradients weaken. This mechanism should take effect in the hypothetical rocky vapor atmosphere on close-in terrestrial exoplanets, on which the surface temperature varies greatly.

The assumption that barotropic instability acts to adjust the state to one of barotropic neutrality can be used to obtain an estimate of the surface pressure and temperature gradient towards which the system is relaxing. Introduce a local Cartesion coordinate y in the vicinity of latitude ϕ_0, measuring distance in the meridional direction. Let $u(y)$ be the zonal wind in a geostrophically balanced state. Then according to the Rayleigh-Kuo criterion neutrality to barotropic instability requires

$$\beta - \frac{\mathrm{d}^2 u}{\mathrm{d}y^2} = 0 \tag{4.2}$$

where $\beta \equiv \frac{\mathrm{d}f}{\mathrm{d}y}(\phi_0) = 2\frac{\Omega}{a}\cos\phi_0$. Geostrophy and Clausius-Clapeyron imply

$$u = -\frac{1}{f_0 \rho}\frac{dp_{\mathrm{sat}}}{dy} = -\frac{1}{f_0} L \frac{1}{T_s}\frac{dT_s}{dy} \tag{4.3}$$

If we stipulate that winds are weak near the poles, Eq. 4.2 implies $u \sim \beta a^2$, where a is the radius of the planet. Further, the planetary scale temperature variation is $\Delta T_s \sim a\frac{dT_s}{dy}$.

Substituting into Eq. 4.3 and solving for the temperature variation yields

$$\frac{\Delta T_s}{T_s} \sim \beta f_0 a^3 \frac{1}{L} \sim \frac{\Omega^2 a^2}{L} \tag{4.4}$$

Therefore, the constraints imposed by barotropic stability only guarantee weak temperature gradients for slow rotators; sufficiently rapid rotators can support large temperature gradients in strongly nondilute atmospheres without the corresponding jet becoming barotropically unstable. Because the latent heat L is typically a large number, however, weak gradients can prevail up to quite large values of Ωa. For example, for an Earth-sized planet with half Earth's rotation rate, a saturated pure water vapor atmosphere would have $\Omega^2 a^2/L = .021$, corresponding to roughly a 2% relative variation in surface temperature. The expression in Eq. 4.4 is similar in form to the parameter $\Omega^2 a^2/RT$ which is small when the WTG approximation is valid for dry atmospheres, except that RT is replaced by L. Since $L \gg RT$ away from the critical point of the atmospheric gas, the barotropic adjustment process in a saturated pure steam atmosphere can maintain weak temperature gradients at higher rotation rates than would be possible in the absence of condensation.

Ekman Spin-down

For planets with a surface which exerts frictional drag on the overlying atmosphere, Ekman spin-down offers another way of damping surface pressure and temperature gradients. Surface temperature gradients induce surface pressure gradients via Clausius-Clapeyron, and these gradients are in turn balanced by a geostrophic wind. Within the frictional boundary layer, the dominant balance between frictional forces on the wind and the Coriolis force induces a drift in the boundary layer in the direction from high pressure to low pressure. Alternately, the process can be understood in terms of the "Einstein's Teacup" analogy, in which the pressure gradients in the boundary layer are nearly the same as in the geostrophically balanced atmosphere aloft, but friction has weakened the wind that induces the balancing

Coriolis forces, thus leaving an unbalance pressure gradient that drives a downgradient current. With either way of looking at it, the process spins down the wind, transport heat and mass toward cold regions, and acts to damp the surface pressure and temperature gradients.

For an Earth-like fast-rotating planet, the Ekman layer is thin enough that the atmospheric temperature in the layer is close to the surface temperature (T_s). Then the energy balance of the planetary system (ignoring heat flux in the ocean) at latitude ϕ can be simplified as

$$S_{abs}(\phi) - OLR(T_s(\phi)) \approx \frac{1}{a\cos\phi}\frac{\mathrm{d}}{\mathrm{d}\phi}\Big(\cos(\phi)M_E(\phi)L(T_s)\Big) \tag{4.5}$$

where S_{abs} is the absorbed stellar flux and OLR is the outgoing longwave radiation of the planetary system respectively, a is the radius of the planet, M_E is the meridional Ekman mass transport and L is the specific latent heat of vaporization (assumed to have a weak temperature dependence). The left hand side of Eq.(4.5) represents the net downwelling radiative flux at the top of the atmosphere and the right hand side represents the divergence of the meridional energy flux. Assuming that friction in the Ekman layer is parameterized by a constant eddy viscosity A, M_E can be described by the product of the layer thickness and the geostrophic zonal wind (Vallis (2006), p. 112), and then is related to the meridional gradient of surface temperature through the Clausius-Clapeyron relation,

$$M_E \approx \frac{1}{2}\sqrt{\frac{A}{\Omega\sin\phi}}\frac{1}{2\Omega a\sin\phi}\left(-\frac{\mathrm{d}p_{sat}(T_s)}{\mathrm{d}\phi}\right) = \frac{1}{2}\sqrt{\frac{A}{\Omega\sin\phi}}\frac{1}{2\Omega a\sin\phi}\left(\frac{Lp_{sat}(T_s)}{RT_s^2}\right)\left(-\frac{\mathrm{d}T_s}{\mathrm{d}\phi}\right) \tag{4.6}$$

where Ω is the spin rate of the planet. The final equality proceeds from application of the chain rule and Clausius-Clapeyron. Furthermore, the outgoing longwave radiation (OLR) of a steam atmosphere is nearly a linear function of T_s before the runaway greenhouse occurs. With the above simplifications, Eq.(4.5) becomes the equation of a diffusive energy balance model with a latitude-dependent diffusivity. The steady-state meridional distribution of T_s can be obtained by solving such a diffusion equation numerically given the insolation profile.

We can simplify Eq.(4.5) further by the mass balance equation if considering the limit in which the horizontal energy transport is so efficient that the global surface becomes isothermal (denoted as T_{s0}),

$$S_{abs}(\phi) - OLR(T_{s0}) \approx \frac{1}{a\cos\phi}\frac{\mathrm{d}}{\mathrm{d}\phi}\Big(\cos(\phi)M_E(\phi)\Big)L(T_{s0}) = (E-P)\Big|_{\phi}L(T_{s0}) \tag{4.7}$$

where $(E-P)$ is the net evaporation rate at the surface (E represents the evaporation and P the precipitation) and is proportional to the net radiative flux at the top of the atmosphere. This implies the condensable substance goes from the surface reservoir to the atmosphere in the low-latitudes, and returns the reservoir again in the high-latitudes.

In Section 4.4.2 we will show simulations demonstrating the effectiveness of this mechanism for equalizing surface pressures and temperatures in nondilute atmospheres.

4.2.3 Inhibition of Subsaturation for Strongly Nondilute Flow

Much of the discussion of the novel behavior of nondilute atmospheres relies on the assumption that nearly saturated conditions prevail within extensive regions of the atmosphere. In Earth's present dilute atmosphere, in contrast, most of the atmosphere is highly undersaturated, even in the free troposphere over the oceans. In Earth's dilute atmospehre, subsaturation is produced primarily through transporting moist air parcels to colder, lower-pressure places (poleward or aloft) where adiabatic expansion and other cooling mechanisms cause most of the condensible substance to rain out, and then transporting them back to higher-pressure warmer places where the warming increases the saturation vapor pressure of the parcel but not the condensible content (until it picks up a new supply of condensible from some source)(Pierrehumbert et al., 2007). This can happen at the scale of baroclinic synoptic eddies in midlatitudes, or on global scales due to planetary Rossby waves in the midlatitudes or Hadley and Walker circulations in the tropics. It can also happen at the scale of ensembles of convective clouds.

There are a number of factors that make it much harder for strongly nondilute atmospheres to generate significant subsaturation. Once a saturated layer is established in such an atmosphere, the dynamics becomes largely barotropic, as discussed in Section 4.2.1, which precludes the vertical motions needed to generate subsaturation. Thus, saturated layers tend to maintain themselves in strongly nondilute atmospheres. Further, the mass-flux in the upward branches of Hadley and Walker circulations do not need to be fully compensated by subsidence in the surroundings in strongly nondilute atmospheres, as the upward flux of vapor is mostly balanced *in situ* by the downward mass flux associated with precipitation (Section 3.5.1). In dilute atmospheres with extensive tropical circulations, the large scale subsidence which brings down dry air from the upper troposphere is a key source of subsaturated air (Pierrehumbert et al., 2007).

More generally, subsaturation is difficult to produce in strongly nondilute atmospheres because a significant isobaric gradient in subsaturation between neighboring air parcels requires a gradient in temperature, since in the pure steam limit the degree of saturation corresponds to the excess of temperature over $T_{\text{sat}}(p)$. In contrast, for a dilute atmosphere, a saturated air parcel can have the same temperature (more precisely the same virtual temperature) as a neighboring completely dry parcel. In a nondilute atmosphere the temperature gradients associated with a subsaturation contrast extending over a deep layer would lead to strong pressure gradients in accordance with hydrostatic balance. This would drive circulations that tend to mix away the gradient. By itself this only implies weak gradients in degree of subsaturation, but if there is any portion of the atmosphere that is maintained near saturation (e.g. in a region of strong nondilute convection), the saturation there will tend to be transmitted to the rest of the atmosphere.

The preceding effects inhibit dynamic production of subsaturation of the type that occurs in Earth's troposphere, but subsaturated layers can nonetheless be produced by radiative means in a nondilute atmosphere. Any layer of the atmosphere within which the local radiative equilibrium $T_{\text{r.e}}(p)$ exceeds the saturation temperature $T_{\text{sat}}(p)$ will be subsaturated. Such layers would typically be produced by strong absorption of shortwave stellar radiation by the atmosphere, and if the atmosphere is so strongly absorbing that essentially no shortwave radiation reaches the surface, the subsaturated layer can even extend all the way to the condensed reservoir at the surface. Note that the stellar heating need not be strong enough to create a temperature inversion. Temperature can decrease with height, so long as it doesn't fall below $T_{\text{sat}}(p)$.

Although the above arguments lend a certain plausibility to the assertion that atmospheres should become more saturated as they become more nondilute (barring effects of strong internal radiative heating), the dynamical issues are subtle and difficult to quantify convincingly without some guidance from full 3D simulations. We'll return to the issue of subsaturation in Section 4.4.4.

4.3 Description of Exo-FMS Model

We have developed an idealized three-dimensional general circulation model (3D GCM) with simplified physical parameterizations that have been utilized in the 1D single column model discussed in Chapter 3, including an active hydrological cycle based on formulations that remain valid regardless of the diluteness of the condensable substance in the atmosphere. It is a variant of the model used to study idealized atmospheres in O'Gorman and Schneider (2008) and Frierson (2007) and the model used to study tidally-locked Earth-like aquaplanets in Merlis and Schneider (2010). These models are designed to improve our understanding of fundamental processes in complex planetary atmosphere, and are different from the models of a high degree of complexity used for making precise predictions.

Two major modifications are made in our model compared with previous studies. First, to avoid numerical instabilities at high concentrations of the condensable substance, our model (hereafter referred to as Exo-FMS) uses the finite-volume dynamical core of the GFDL Flexible Modeling System (FMS) described in Lin (2004) instead of the spectral transform method used in O'Gorman and Schneider (2008) and Merlis and Schneider (2010) to solve three-dimensional primitive equations of an ideal-gas atmosphere. Second, Exo-FMS uses an energy-conserving simplified moist convection scheme without any approximation about the diluteness of the condensable substance while conventional GCMs usually use the dilute approximation and assume the surface pressure and thermodynamic parameters of the atmosphere is insensitive to the amount of condensible substance in the atmosphere. Our moist convection scheme is similar in spirit to the hard convective adjustment scheme in Manabe and Strickler (1964), but conserves non-dilute moist enthalpy while the condensate is produced and retained in the atmosphere, and takes the energy change due to mass redistribution into account when the condensate falls to the surface or enters the atmosphere through surface evaporation. The condensate falls within the same time step right after it is produced in the super-saturated layer. The nondilute moist convection scheme is described and validated in Chapter 2, where we show that it conserves both energy and mass from the dilute to non-dilute regime. Similarly, our large-scale condensation scheme takes into account the conservation of non-dilute moist enthalpy and the energy loss associated with large-scale condensation precipitation. Microphysical effects are no doubt of considerable importance in all planetary atmospheres with a condensible component, but in these simulations we neglect the microphysics governing formation and removal of precipitation, as well as effects of retained condensate and atmospheric heating due to frictional dissipation surrounding falling precipitation.

Since we wish to highlight dynamical phenomenon, the Exo-FMS simulations presented here use a gray radiation scheme in the infrared spectral region, and assumes the atmosphere is transparent to shortwave radiation. The longwave optical depth τ has two contributions

$$\tau(p) = \kappa_0 \int_0^p q(p')\frac{\mathrm{d}p'}{g} + \tau_1 \frac{p}{p_s} \tag{4.8}$$

where κ_0 and q are the absorption cross-section and the mass concentration of the condensable substance respectively, and τ_1 is the total optical thickness of the non-condensable absorber which is assumed to be well-mixed in the atmosphere . Both κ_0 and τ_1 are constants.

In the simulations we present, τ_1 and κ_0 are independant of the total mass of noncondensable in the atmosphere. This is somewhat unrealistic since it assumes the total mass of the noncondensable greenhouse gas decreases with p_s in such a way as to compensate for pressure broadening and keep τ_1 fixed, and also neglects pressure broadening or collisional opacity of the condensible component. However, this experimental protocol allows us to keep the mean surface temperature roughly fixed as the mass of the noncondensable background is changed, and thus makes it easier to isolate the effects of nondiluteness. For similar reasons we avoid the complex issues associated with cloud feedbacks by neglecting the radiative effect of clouds.

The opposite regime from the shortwave-transparent atmospheres we consider in the present work is the one in which atmospheric shortwave absorption is so strong that essentially all incoming stellar radiation is deposited directly in the atmosphere, rather than being deposited at the ground and being communicated upwards by radiation and convection. Many exoplanets, including low density Super-Earths such as GJ 1214b, are expected to be fluid planets with no distinct surface at all. Planets without appreciable deposition of stellar energy at a distinct surface can nonetheless have nondilute layers, as discussed in Section 1.2. This is an important regime, which will be the subject of future work.

In Exo-FMS, the specific heat capacity of the substances in the atmosphere are treated as constants, but the specific latent heat of vaporization has a weak temperature dependence. The specific latent heat of a material varies approximately linearly with the temperature when the density of the condensate is much greater than that of its vapor phase (Emanuel (1994), p. 115).

$$\frac{\mathrm{d}L}{\mathrm{d}T} \approx c_{pc} - c_{p\ell} \tag{4.9}$$

Here c_p is the specific heat capacity at constant pressure, and subscript "c" and "ℓ" represents the vapor phase and the condensate, respectively. With this form of temperature dependence it is fairly straight forward to formulate a moist enthalpy incorporating both gaseous and condensed phases, which is conserved when the enthalpy carried by precipitation is taken into account. For simplicity, there is only a single phase transition in Exo-FMS, which could equally be interpreted as liquid-vapor or ice-vapor.

The lower boundary of the column model is a liquid slab ocean with uniform thickness. At the surface, the sensible and latent heat fluxes are computed based on the bulk exchange formulae (see Pierrehumbert (2010), p. 396) assuming constant drag coefficient ($C_D = 0.005$). The surface pressure is calculated not only by the air flow divergence above the ground as in conventional GCMs, but also by the ($E-P$) flux at the surface. In the surface energy budget, other than the sensible and latent heat fluxes and the radiative flux, we also take into account the internal and potential energy flux of the exchanged mass between the atmosphere and the surface reservoir to conserve energy. In Exo-FMS, both the mass of the non-condensable and condensable substances (including both phases in the atmosphere and surface reservoir) are conserved. The former conservation is automatically achieved by the FMS finite-volume dynamical core. The mass budget of the slab ocean requires a mass redistribution scheme to even out the horizontal variations of the ocean depth created by the distribution of $P - E$. Otherwise, the liquid substance will accumulate in some places and be depleted in other places. At each time step, mass is redistributed so as to keep the ocean depth globally uniform, and then a globally uniform temperature offset is applied to the ocean temperature so as to enforce conservation of oceanic energy in the course of the mass adjustment. The oceanic heat transport implied by the temperature adjustment is small because it is only the heat associated with the mass added to or taken away from an ocean column that is mixed throughout the global ocean, leaving the pre-existing temperature gradients intact. Details of the adjustment scheme, as well as other technical details concerning the formulation of Exo-FMS, are provided in Appendix B.

To show that Exo-FMS is capabable of reproducing features familiar from other moist simulations of circulation of tide-locked planets, we will show one Earth-like tidally locked simulation with experimental design essentially identical to those described by Merlis and Schneider (2010), except that the period of the circular orbit is taken to be 50 Earth days.

Two latitude-height cross sections of temperature are shown in Figure 4.1. Exo-FMS reproduces the WTG behavior (Figure 9 in Merlis and Schneider (2010)) in the free troposphere. In our simulation, the horizontal temperature gradient is small aloft both on the dayside and nightside of the planet. Other familiar features include the shallow hot-spot in the lower atmosphere over the substellar point, and the nightside temperature inversion near the surface. Horizontal winds, vertical velocity and precipitation are shown in Figure 4.2, and reproduce the typical features of strong low-level convergence into a region of concentrated updraft and precipitation near the substellar point, subsidence aloft over most of the planet. Aloft, the simulation reproduces the familiar equatorial super-rotating winds and the global Kelvin/Rossby wave pattern expected in a planet with weak but nonvanishing rotation.

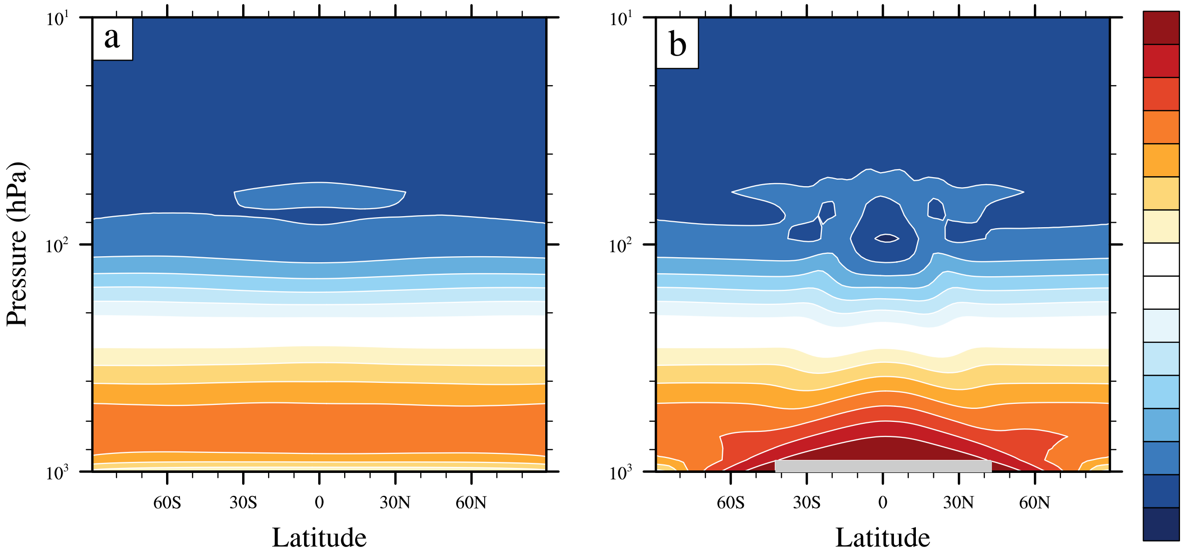

Figure 4.1: Cross section of the atmospheric temperature (K) along anti-stellar longitudes (a) and substellar longitudes (b) of a tidally-locked simulation conducted in the dilute regime. Averages are taken over 10° of longitude.

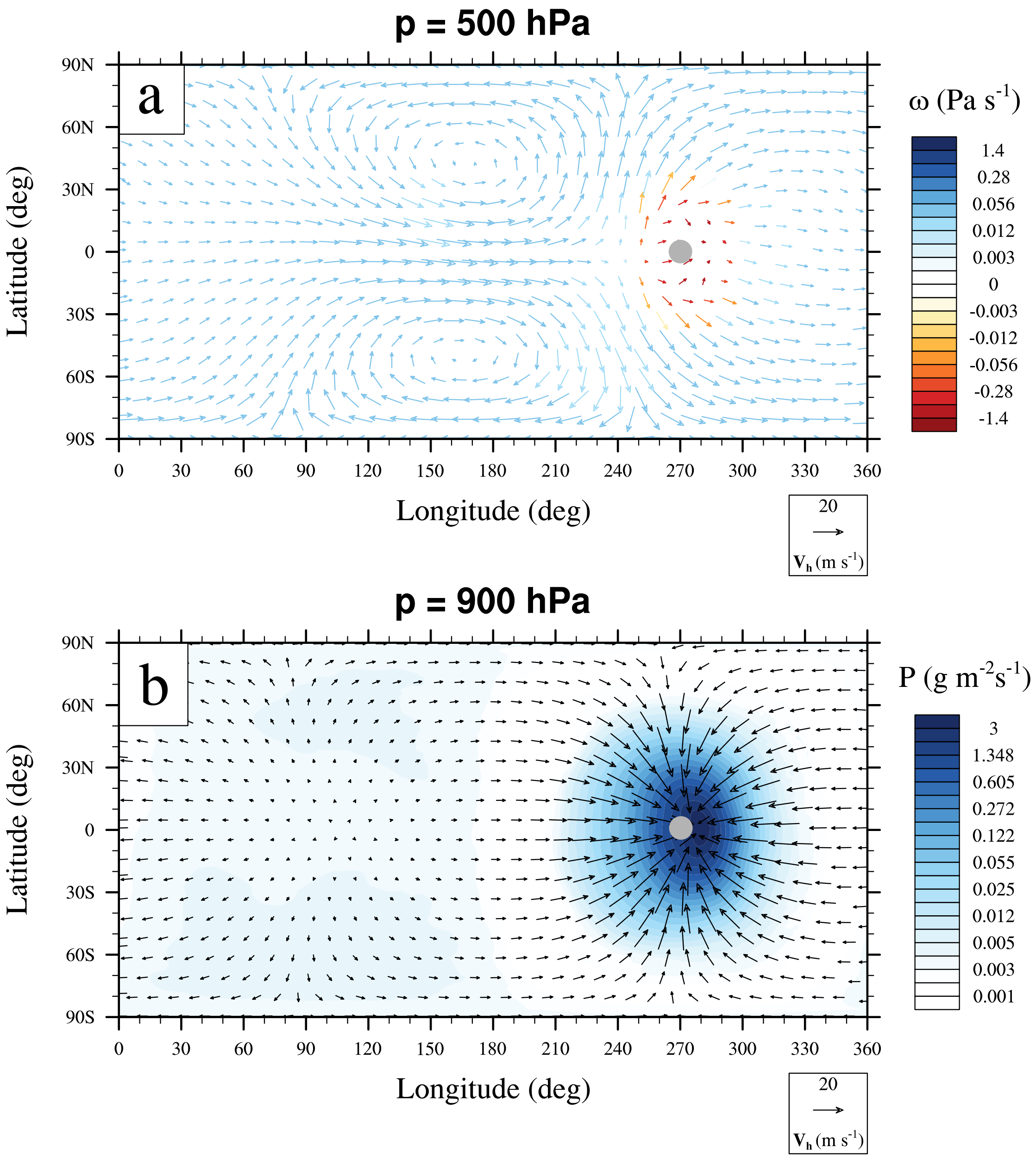

p = 500 hPa

p = 900 hPa

Figure 4.2: Upper panel: 500 hPa horizontal winds (arrows) and vertical pressure velocity ω (arrow colors) for the dilute tidally locked simulation. Lower panel: 900 hPa winds (arrows) and net column precipitation (color shading), The grey circle marks the substellar point.

4.4 3D Simulations of Nondilute Atmospheres on Rapid Rotators

4.4.1 Simulation Design

Since the novel effects of nondiluteness are most striking in the case of rapid rotators, we concentrate on that case here. Hot tide-locked planets in short-period orbits can be rapid rotators, but we'll also focus here on Earthlike annual mean instellation patterns, which are symmetric about the rotation axis. For tide-locked planets, whether slowly or rapidly rotating in the sense of the WTG approximation, nondiluteness is expected to cause interesting and important deviations from the dilute pattern consisting of subsaturated subsiding air over most of the planet, but that will be the subject of a future work.

Our simulation design is similar to the study of the runaway greenhouse state of a 3D gray atmosphere in Ishiwatari et al. (2002), except we have performed simulations with a range of values of the inventory p_{a0} of the noncondensible gas. The noncondensible inventory is the parameter we vary in order to control the diluteness of the atmosphere. An alternate way to control diluteness is to keep p_{a0} fixed but vary the instellation of the planet (corresponding to changing the luminosity of the star or the radius of the orbit), but varying p_{a0} makes for a cleaner exploration of nondiluteness effects because the maximum surface temperature remains approximately fixed in our simulation. All other parameters are chosen to mimic the present Earth conditions. The non-condensable substance in the simulation is mixed N_2-O_2 air, as in the present Earth's atmosphere, while the condensable substance is water vapor. As in Ishiwatari et al. (2002), the longwave absorption cross-section of water vapor κ_0 is a constant [1], $0.01\,\mathrm{m^2\,kg^{-1}}$. The atmosphere is transparent to the shortwave incoming radiation and the surface albedo is zero.

The top-of-atmosphere instellation is given by the annual and zonal average evaluated with the present Earth's orbit, approximated by

$$S_{TOA}(\phi) = S_0(1 + 0.3(1 - 3\sin^2\phi)) \tag{4.10}$$

where $S_0 = 300\,\mathrm{W\,m^{-2}}$ is the global mean insolation and there is no diurnal or seasonal cycle. The horizontal resolution utilized in this study is 144×96, and there are 40 unevenly

---

[1] An average angle should be taken into account in the two-stream radiation equations because the infrared flux tends to become forward-peaked as it propagates. Our chosen κ_0 has already include this effect. This is slightly different from the radiation scheme utilized in Ishiwatari et al. (2002) who do not specify the average angle they chose.

spaced vertical levels in hybrid $\sigma = p/p_s$ coordinate (pressure p and surface pressure p_s). The pressure of the radiative level in a pure water-vapor atmosphere in our model is 9.8 hPa. Given that the strongest radiative cooling and convective heating of water vapor occurs near the radiating level, the pressure at the top of our model is chosen to be 0.01 hPa in order to resolve the radiative and convective processes in the non-dilute atmosphere.

As listed in Table 4.1, four experiments are presented with different values of noncondensible inventory p_{a0}. Each experiment is referred to as a letter P followed by the value of p_{a0} in hPa specified in the experiment. Experiment P1000 is the run that mimics the present Earth's atmosphere. The results we present are averages over the last 600 days of 3000-day integrations.

Table 4.1: The list of experiments and the values of the initial surface partial pressure of the N_2-O_2 air (p_{a0}), global mean surface temperature (T_s) and global mean mass concentration of water vapor in the atmosphere q for each experiment.

Experiment	p_{a0} (hPa)	Global mean T_s (K)	Global mean q (kg/kg)
P1000	1000	294.40	6.41×10^{-3}
P30	30	287.37	0.21
P5	5	292.71	0.70
P0	0	287.79	1.00

Because the mass of dry air in our experiments has no direct radiative effect, the global mean T_s varies only by 7 K[2] (Table 4.1). Hence, it is primarily the mass of dry air that alters the concentrations of water vapor in the atmosphere by two orders of magnitude. Though we vary the partial pressure of the non-condensible gas in theses simulations primarily as a convenient means of controlling nondiluteness, there are in reality many real physical processes that can enter into the determination of the noncondensible inventory on actual planets, so exoplanet climate studies should always consider a wide range of possible values for this parameter. For our own planet Earth, a surface pressure of two or three times the present value is proposed to help reduce the amount of CO_2 needed to resolve the 'Faint

---

[2] There is an indirect radiative effect through the effect of the dry air on the lapse rate, and through nonlinear rectification of surface temperature variations in latitude.

Young Sun' paradox, via pressure-broadened increase of infrared absorption of greenhouse gases (Goldblatt et al., 2009) or the H_2-N_2 collision-induced absorption (Wordsworth and Pierrehumbert, 2013a), though fossil raindrop imprints suggest an absolute upper limit of less than 2100 hPa for the late-Archean climate (Som et al., 2012). The mass of the non-condensable on Earth-like exoplanets is even more difficult to constrain by transit spectra. The mass of the non-condensable can affect the planetary climate through various ways, and our study here only focuses only on diluteness effects.

4.4.2 Basic Description of Zonal-mean Temperature and Humidity Fields

The zonal mean temperature fields in the simulations are shown in Figures 4.3a-d, and the specific humidity fields (Figuress 4.3e-g) provide an indication of the degree of diluteness of the atmosphere in each simulation. The most dilute experiment, P1000, exhibits a latitude-height pattern of temperature and humidity similar to the Earth's present atmosphere, with WTG behavior seen only in the tropics. As the atmosphere is made more nondilute, the vertical temperature gradients become weaker; this is a simple consequence of the flatness of the moist adiabat, and its tendency to become nearly isothermal as the steam atmosphere limit is approached. The temperature gradient on isobaric surfaces also becomes weaker, as expected from the discussion in Section 4.2.1. Moreover, the planet's surface becomes nearly isobaric (and hence nearly isothermal), as argued in Section 4.2.2. Specifically, the equator-to-pole surface temperature differences in the four experiments reduce from 40 K in P1000 to 1 K in P0.

Note that even in the very nondilute case P5, the low level specific humidity varies by nearly 25%, with lowest values appearing in the polar regions. This may be surprising in view of the weak temperature gradients, but it is a simple consequence of the fact that the exponential dependence of vapor pressure on temperature makes the specific humidity very sensitive to temperature in cases with just a small amount of noncondensible gas.

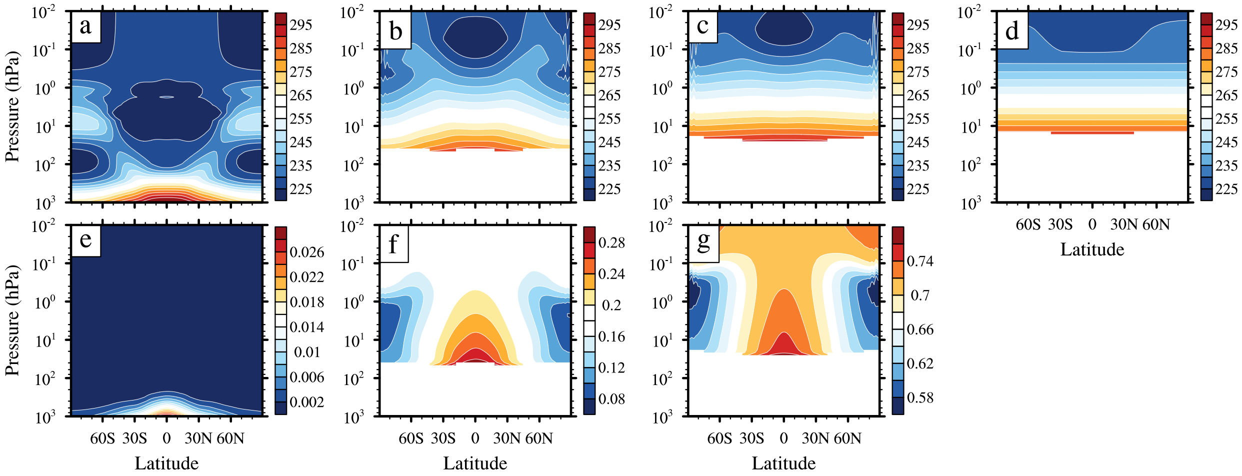

Figure 4.3: Zonal-mean cross sections of the temperature (K) in experiments (a) P1000, (b) P30, (c) P5 and (d) P0, and the mass concentration of water vapor (kg/kg) in experiments (e) P1000, (f) P30 and (g) P5. The concentration of water vapor in experiment P0 is unity everywhere in the atmosphere, and therefore is not shown in the figure. The plots of temperatures share the same contour intervals. The white horizontal bars at the bottom of the atmosphere are due to meridional surface temperature variations when the atmosphere becomes non-dilute.

4.4.3 The Nature of the Circulation

Latitude-height profiles of zonal mean wind are shown in Figures 4.4a-d, with corresponding meridional circulation shown in Figures 4.4e-h. The streamfunctions are computed using only the large scale velocity, and not the convective mass transport of condensible implicit in the convection parameterization, which is balanced by the mass flux of precipitation. For experiment P1000, which has Earthlike diluteness, there are baroclinic jets associated with midlatitude temperature gradients. Detailed examination of the transient eddy properties is beyond the scope of the present work, but an examination of the time behavior (not shown) reveals Earthlike midlatitude baroclinic eddies and eastward-propagating convectively coupled waves in the tropics. There is a strong Hadley circulation. This only appears shallow because of the large range of pressures plotted; it in fact reaches to approximately 200 hPa. Associated with this circulation is a pair of strong subtropical jets. These subtropical jets are somewhat more strongly separated from the midlatitude jets than is generally the case in Earth's present climate, but that may be due to the aquaplanet configuration.

At the other extreme, in the pure steam simulation there is essentially no horizontal temperature gradient in the interior of the atmosphere. In accordance with Section 4.2.1, the vertical zonal wind shear vanishes and two barotropic jets emerge at $\sim 60^\circ$ (experiment P0, Figure 4.4d). The jets are weak and barotropically stable, and in fact the system settles into a time-independant state with no transient eddies at all. This suggests that the surface pressure gradients are being determined by the Ekman transport mechanism rather than barotropic adjustment, which would proceed via barotropic instability. The Hadley cell has completely vanished, and meridional mass transport is dominated by boundary layer currents which carry mass from the high pressure tropics to the low pressure poles.

The pure steam simulation illustrates a striking effect of nondiluteness on the angular momentum budget of the planet. In this simulation, the low level flow is everywhere poleward, and maintains surface winds that are westerly everywhere. At first glance, this appears paradoxical, because the resulting unbalanced torque would spin up the planet without bound, violating angular momentum conservation. The resolution relates to the angular momentum carried to the surface by precipitation. The everywhere-poleward mass flux, which would be impossible in a dilute atmosphere, is possible in this case because the atmosphere picks up mass through evaporation in the tropics and loses it by precipitation at higher latitudes. The Coriolis force acting on this current maintains the global surface westerlies against friction. The mass added to the atmosphere in the tropics takes high angular momentum with it. As air parcels move poleward, their angular momentum reduces through the action of friction. Thus, when mass is returned to the surface by precipitation, it has lower angular momentum than when it left the surface in the tropics. This acts as a sink of angular momentum of the surface ocean, compensating the net torque exerted on it. In experiment P0, the global mean value of the angular momentum source and sink are estimated as 5.49×10^4 N·m /m^2 and 5.60×10^4 N·m /m^2, respectively, which very nearly closes the angular momentum budget in this pure steam simulation.

In the intermediate cases P30 and P5, the main surprise is that the vertical wind shear is

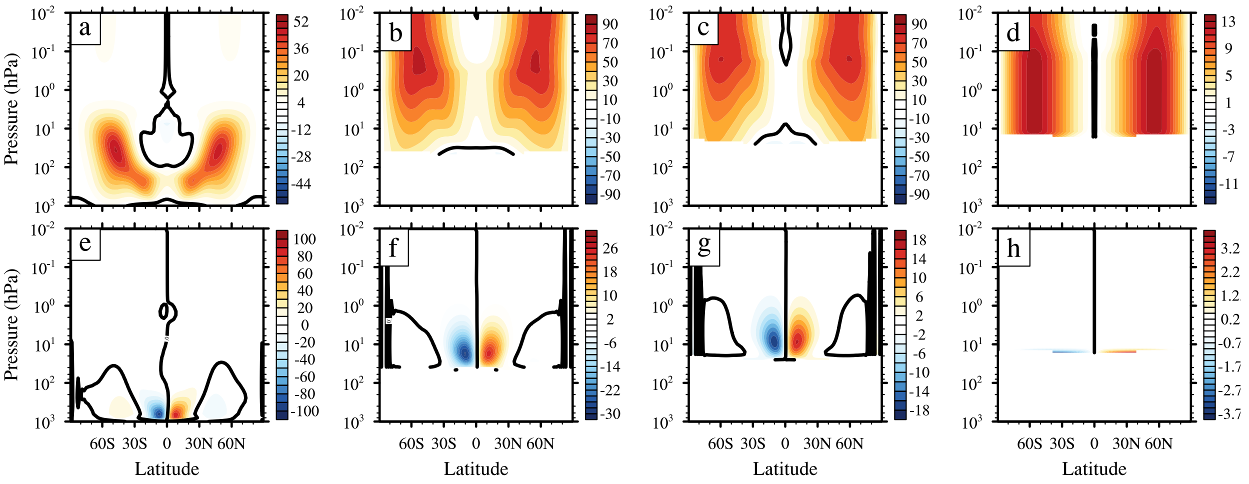

Figure 4.4: Upper panels: Zonal-mean cross sections of the zonal wind component ($\mathrm{m\,s^{-1}}$) in experiments (a) P1000, (b) P30, (c) P5 and (d) P0. Low panels: Same as the upper panels, but for the zonal-mean cross sections of the mass streamfunction in $10^9\,\mathrm{kg\,s^{-1}}$ in each experiments.

quite strong, despite the weakening horizontal temperature gradients. In fact, the maximum jet speed actually increases between the Earthlike case and the more nondilute case P30. This behavior arises in part because the thermal wind relation (Eq. 4.1) has a pre-factor p^{-1} which tends to amplify the vertical shear (as seen in pressure coordinates) when the pressure is low. The rest of the behavior is due to a novel dynamical effect of moisture in the nondilute regime. In a dilute atmosphere, the gas constant R in Eq. 4.1 is nearly constant. It is also constant in the pure steam limit. However, in nondilute atmospheres that aren't close to the pure steam limit, R varies greatly in the horizontal because the variations of specific humidity lead to variations in the mean molecular weight of the atmosphere. Recall that $R = R^*/M$, where M is the mean molecular weight. Since the simulations were done with dry air (molecular weight 29) as the noncondensible and water vapor (molecular weight 18) as the condensible, the lower specific humidity towards the poles in cases P30 and P5 leads to higher mean molecular weight and lower R in polar regions, yielding an effect analogous to decreasing temperature poleward with fixed R. The effect could be captured in the conventional form of the thermal wind relation by defining a virtual temperature T_v such that $RT = R_dT_v$, where R_d is the gas constant for the noncondensible background atmosphere. Note that the sign of the compositional thermal wind would be reversed if the condensible had higher molecular weight than the background, e.g. for condensible H_2O or CO_2 in noncondensible H_2. In such situations, the moderately nondilute climates would exhibit weaker or even easterly vertical shear.

The intermediate diluteness cases exhibit a Hadley cell of the classic form, but it gets wider, deeper (as measured by range of pressure it covers) and weaker as the nondiluteness is increased. The depth increase results from the elevation of the tropopause, which in turn is associated with the weak lapse rate associated with hot moist adiabats. The causes of the broadening are more subtle and require further analysis, which we will not pursue here.

Unlike the pure steam case, the intermediate diluteness cases do exhibit transient eddies. In case P5, the transience consists of fairly large scale convective clusters that appear and disappear without any clear propagation. Though there is some eddy activity in the midlatitudes, this is largely barotropic and almost all precipitation in case P5 is convective precipitation associated with the tropical convective clusters. It is interesting that the compositional meridional baroclinicity does not give rise to baroclinic instabilities. This may arise because ascending, condensing motions do not alter the mass distribution, while noncondensing descending motions expend energy in subsiding through a statically stable atmosphere. The stability of jets arising from compositional pressure gradients requires further study, and this, as well as an analysis of the tropical transient eddies, will be reserved for future work.

Since the pole-to-equator instellation gradient is held fixed in these simulations, the weakening of the meridional temperature gradient as nondiluteness is increased implies that the atmosphere must be carrying heat poleward at a greater rate in the more nondilute cases. This may seem surprising, given that the atmospheric mass goes down in these simulations as the noncondensible background gas is reduced. However, while total atmospheric mass goes down, the mass of water vapor in the atmosphere rises markedly from experiment P1000 to P0, due to the decrease in vertical lapse rate and the rise of atmospheric relative humidity.

This allows increased poleward latent heat transport ($\int_0^{p_s}(Lqv)\mathrm{d}p/g$) leading to the uniform surface temperature in experiment P0. Figure 4.5 shows the meridional distributions of the shortwave and longwave radiative fluxes at the top of the model together with $(E-P)$ for the pure steam case. The outgoing longwave radiation is essentially independent of latitude in this case. $(E-P)$ has the right shape and magnitude (when scaled by latent heat) to balance the radiative imbalance, verifying that, though thin, the latent heat of the atmosphere allows it to nonetheless transport energy efficiently. This mechanism breaks down for atmospheres where the temperature can only produce an extremely low vapor pressure, as is the case for the local condensing SO_2 atmosphere of Io. The analogous local rock vapor atmospheres discussed in Castan and Menou (2011) are not especially thin, nor is the latent heat of rock vapor condensation notably small; the breakdown of the barotropic global atmosphere behavior in this case is probably because the latent heat transport is still not large enough to flatten the enormous incoming differential radiative heating. Related issues will be discussed in Chapter 6.

4.4.4 Saturation Dynamics

The relative humidity of an air parcel is the ratio of the partial pressure of the condensible substance in that air parcel to the saturation vapor pressure corresponding to the temperature of the air parcel.

The relative humidity distribution affects the mass of water vapor in the atmosphere and therefore the meridional heat transport. Further, when the condensible is a greenhouse gas (as in the case of water) it has a strong impact on the radiation budget of the planet. For Earth's atmosphere, how the relative humidity is distributed and how this distribution changes in a warming world are key questions involved in understanding the feedbacks that determine the sensitivity of climate to changes in radiative forcing. This would be equally true for other planets for which the condensible substances have a significant greenhouse effect.

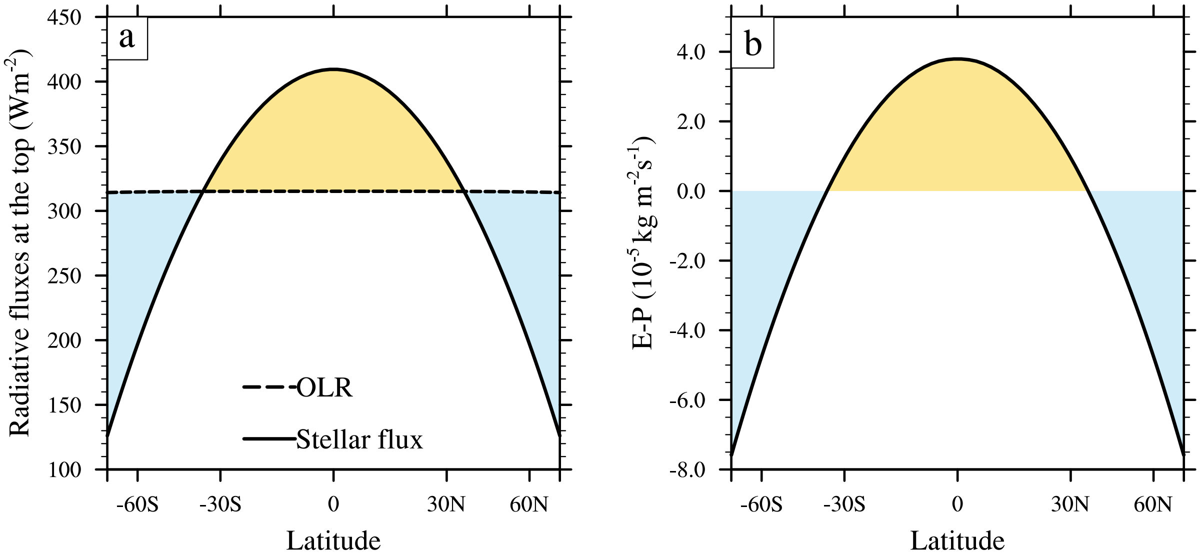

Figure 4.5: (a) Meridional profiles of the insolation (solid) and the OLR (dashed) in experiment P0. The yellow shaded area marks the latitudes with radiative energy surplus, while the blue ones mark the latitudes with energy deficit. (b) Meridional profile of the net evaporation rate at the surface (E-P) in experiment P0. Similarly, the yellow shaded area shows the latitudes where net water mass flux goes from the surface reservoir to the atmosphere. The model has reached both mass and energy equilibrium, indicating that the area of the yellow shaded region is equal to the sum of the two blue ones in both two plots.

A paradigm of nonlocal large-scale control of tropospheric humidity has long been proposed for understanding the relative humidity distribution in Earth's atmosphere, known as the advection-condensation model (Pierrehumbert and Roca, 1998; Pierrehumbert et al., 2007). This model makes use of the property that the mixing ratio of the condensible in an air parcel is conserved along any segment of a trajectory which doesn't encounter conditions where it becomes saturated and loses water by precipitation. Hence the relative humidity of the air parcel at its destination is the ratio of the saturation molar mixing ratio r_{sat} of water vapor at the position of the last saturation to that at the destination, and the relative humidity at the final position has no sensitivity to the air parcel's history at times earlier than the last saturation. This is an idealized model of relative humidity, as unsaturated air parcels can gain moisture by evaporation of precipitation or mixing with neighboring moist parcels, or lose it by mixing with neighboring dry parcels; however the advection-condensation model has been found to have considerable quantitative explanatory value. In terms of equations, the last-saturation model giving the relative humidity at position $\mathbf{x}$ can be expressed as

$$RH(\mathbf{x}) \equiv \frac{p_c(\mathbf{x})}{p_{\mathrm{sat}}(\mathbf{x})} = \frac{r_c(\mathbf{x})}{r_{\mathrm{sat}}(\mathbf{x})} = \frac{r_{\mathrm{sat}}(\mathbf{x}_{last})}{r_{\mathrm{sat}}(\mathbf{x})} = \frac{p_{\mathrm{sat}}(\mathbf{x}_{last})}{p_{\mathrm{sat}}(\mathbf{x})} \frac{p_a(\mathbf{x})}{p_a(\mathbf{x}_{last})} \tag{4.11}$$

where $r_c \equiv p_c/p_a$ is the molar mixing ratio of the condensible, r_{sat} its value at saturation, p_{sat} is the saturation vapor pressure and the subscript 'last' stands for the position of last saturation. This model was used to reconstruct relative humidity in the Earth's subtropics using a backward Lagrangian trajectory technique, and showed excellent agreement with the Meteosat satellite observations (Pierrehumbert and Roca, 1998). The assumption about water mass in an air parcel in the advection-condensation model is exactly what occurs in our GCM since there is no microphysical cloud scheme or small-scale unresolved turbulent mixing (apart from numerical diffusion). Therefore we can use the concept of last saturation to explain the simulated relative humidity distribution. The typical situation leading to strong subsaturation is when the air parcel came from a higher, colder place. In that case, the first ratio at the end of Eq. 4.11 is very small, because of the exponential dependence of saturation vapor pressure on temperature; the second ratio is greater than unity because of the subsidence and compression of the air parcel, but it is invariably overwhelmed by the exponentially small first term.

Figure 4.6 shows the cumulative distribution of the relative humidity for the four simulations. Results are shown on two different σ surfaces: one near the mid-troposphere ($\sigma = 0.51$) and the other in the upper atmosphere ($\sigma = 0.12$). First, because the saturation mixing ratio decreases with height, the driest air parcel in the troposphere usually forms in the subtropics and is last saturated at the coldest location in the troposphere–the tropopause at the equator. We can roughly estimate the minimum relative humidity in experiment P1000 by the advection-condensation model. From the mass steamfunction in Figure 4.4e and the air temperature in Figure 4.3a, the driest air parcel should be last saturated near 150 hPa with

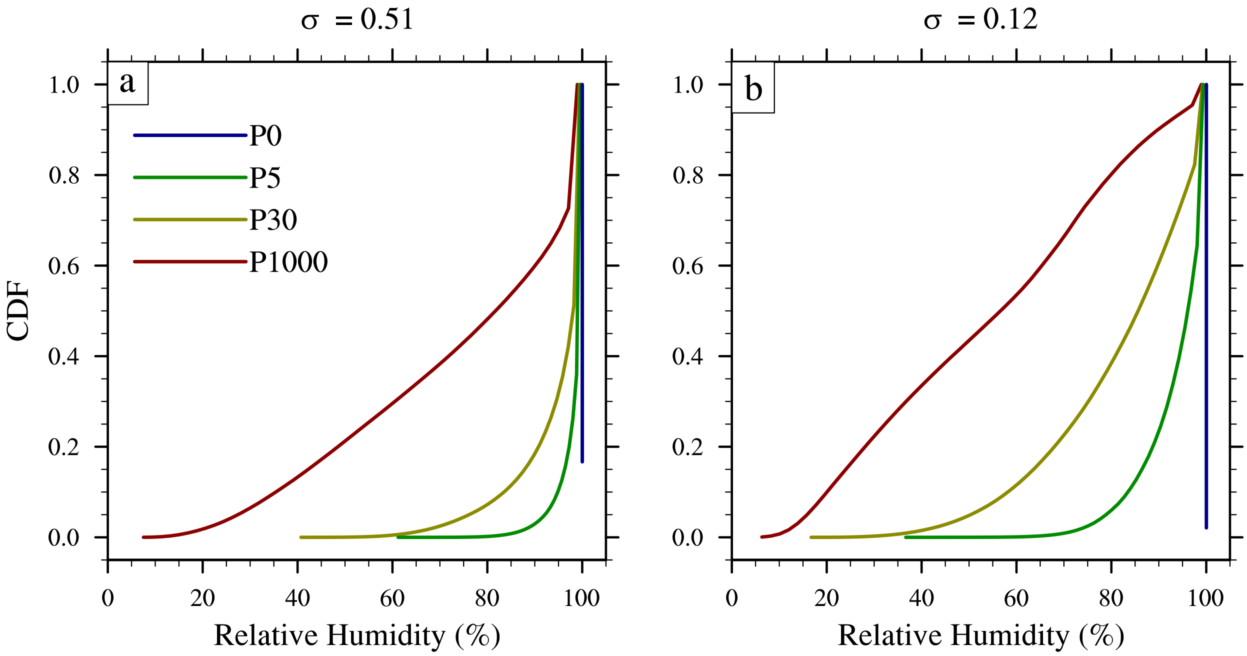

Figure 4.6: Cumulative distribution function of relative humidity in experiments P1000 (red), P30 (yellow), P5 (green), P0 (blue) on the $\sigma = 0.51$ (a), 0.12 (b) surfaces. The data samples are taken from a 100-day integration and collected once per day.

the temperature of 235.4 K. Since the subtropics also satisfy the WTG approximation, the temperature at 510 hPa can be computed by the moist adiabat, which is 283.4 K. Then the estimated relative humidity given by Eq.(4.11) is 7.0%, and very close to the minimum value in the simulation (the left end point of the red curve in Figure 4.6a). Second, Figure 4.6a and b show a general trend that the troposphere becomes more saturated as the water vapor concentration rises. This is again related to the decrease in the vertical lapse rate ($\mathrm{d}\ln T/\mathrm{d}\ln p$), which leads to a decrease in the vertical relative change of saturation mixing ratio ($\mathrm{d}\ln r_{\mathrm{sat}}/\mathrm{d}\ln p$) and a small expansion of the troposphere (Figure 4.3a-c). Although the latter one tends to dry the upper troposphere, the former one wins the competition.

The role of the last-saturation statistic changes markedly, however, as the pure-steam limit is approached. For a nearly pure-steam atmosphere, $p_{\mathrm{sat}}(\mathbf{x}_{last}) \approx p(\mathbf{x}_{last})$ and since p_a/p_c is conserved along the noncondensing trajectory $p_a(\mathbf{x}_{last})/p_c(\mathbf{x}_{last}) = p_a(\mathbf{x})/p_c(\mathbf{x})$, which in the nearly pure steam limit implies $p_a(\mathbf{x})/p_a(\mathbf{x}_{last}) \approx p(\mathbf{x})/p(\mathbf{x}_{last})$. Plugging this into the last equality in Eq. 4.11 then implies

$$RH(\mathbf{x}) = \frac{p(\mathbf{x})}{p_{\mathrm{sat}}(\mathbf{x})} \tag{4.12}$$

This depends only on the local temperature and pressure where the parcel lands. It is independent of the parcel's history, except insofar as that history affects the final temperature of the parcel. In contrast to the more dilute cases, subsaturation cannot be created by "bringing down" dry air from aloft. It can only create subsaturation by heating up an air parcel, either by adiabatic compression or net radiative heating. In our simulation there is no net radiative heating internal to the atmosphere, but in principle, subsaturated air could still be produced by subsiding motions that are fast enough to overcome radiative cooling. This does not happen to any significant extent in our pure steam simulation (the two blue lines in Figure 4.6a and b), and the atmosphere to all intents and purposes becomes saturated everywhere except in the very thin stratosphere where radiative heating warms the atmosphere to temperatures greater than the dew point.

The upper tropospheric relative humidity (UTRH) can vary the pressure of the radiating level (the optical thickness between the radiating level and the top of the atmosphere is approximately unity for an optically thick gray atmosphere), and therefore the OLR. It is not easy to show the change of the relative humidity above the radiating level directly in the simulations listed in Table 4.1. Here we develop another experiment and simulate a runaway greenhouse atmosphere to study the change of the UTRH as the atmosphere becomes non-dilute and the radiative effect due to this change. We use the temperature, humidity and wind fields on day 3000 of the experiment P1000 as the initial condition and trigger a runaway greenhouse by raising the global mean insolation to $450\,\mathrm{W\,m^{-2}}$. The value is well above the threshold of 1D runaway greenhouse assuming a relative humidity of 45% in our gray radiation scheme. We plot the OLR as a function of T_s with both quantities averaged in the tropics in Figure 4.7b. Due to the WTG approximation, the comparison

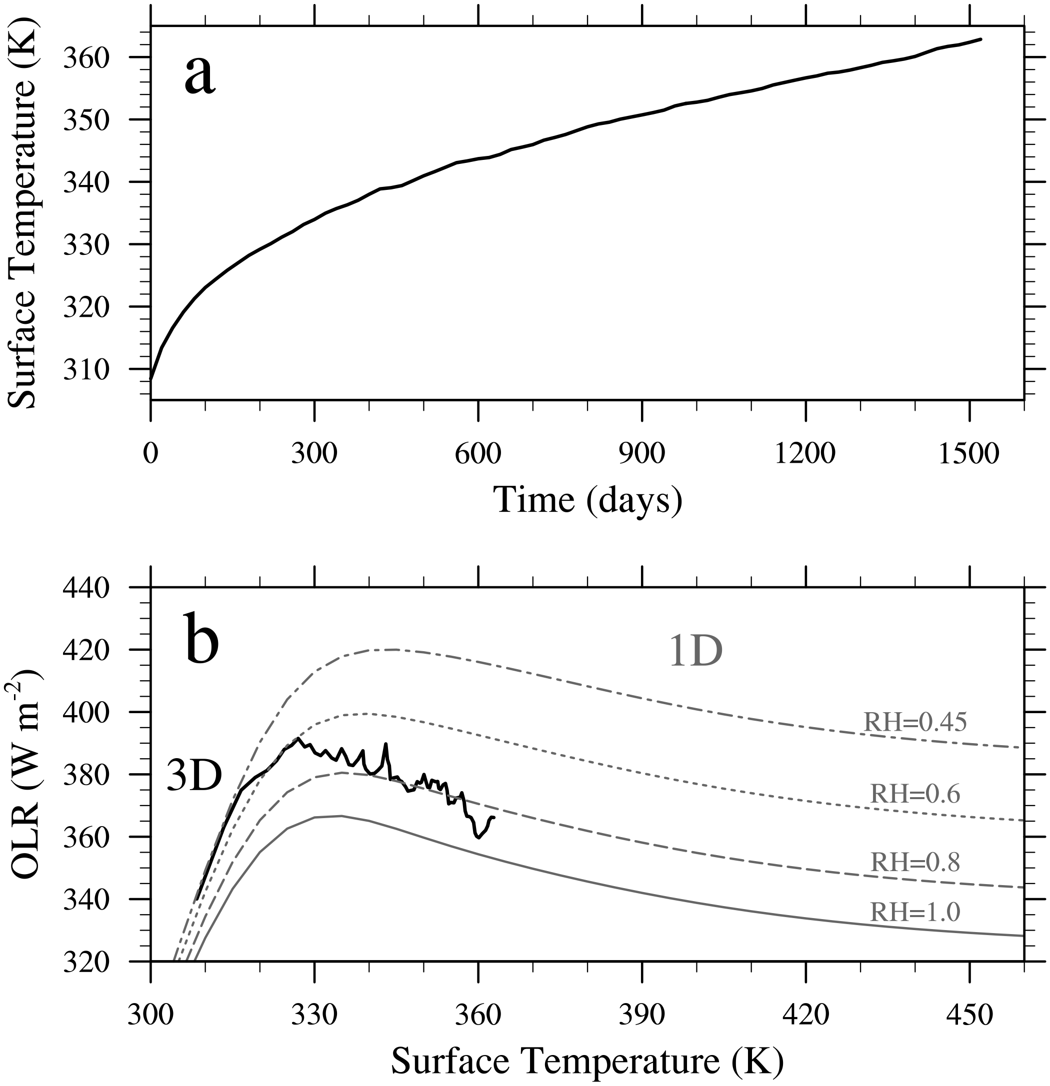

Figure 4.7: (a) Time evolution of the tropical mean T_s (averages are taken within 30° of latitude) in the runaway greenhouse experiment with global mean insolation of $450\,\mathrm{W\,m^{-2}}$. (b) OLR dependence on T_s in tropics. The black curve shows results for the idealized 3D simulation, and gray curves show results for for 1D radiative-convective simulations. The 1D model assumes moist adiabat and uses various values of relative humidity in the 1D radiative transfer.

between the modeling result and the 1D reference curves corresponding to various relative humidities could roughly[3] give the degree of saturation averaged near the tropical radiating level. The relative humidity first stays constant at 45% until the T_s reaches 315 K, and then

---

[3] The relation between the OLR and the water path is not linear

it continue to rise towards unity as the planet warms. Another idealized simulation on the 3D runaway greenhouse gray atmosphere also show similar trend of the UTRH (Figure 7 in Ishiwatari et al. (2002)). Recently, Leconte et al. (2013) conducted a study of the runaway greenhouse in an idealized 3D GCM with a real-gas radiation scheme. This new simulation showed a decrease in UTRH before runaway greenhouse occurs ($T_s \approx 320\,\mathrm{K}$, Extended Data Figure 3b in Leconte et al. (2013)), probably because of the emergence of a cold tropopause owing to real-gas radiation effects. However, when the surface temperature continues to increase and the runaway greenhouse atmosphere becomes non-dilute, the UTRH should rise again and approach unity according to our discussion regarding $\mathrm{d}r_{\mathrm{sat}}/\mathrm{d}p$ above. This effect is not seen in Leconte et al. (2013), but some indication of this behavior is found in the simulation of the same problem in Wolf and Toon (2015), which also edges into the nondilute regime.

This increase in UTRH leads to an interesting question about multiple equilibria in the real runaway greenhouse atmosphere. Assuming constant planetary albedo that does not change with T_s, for a pure water-vapor atmosphere, there is only one stable equilibrium state when the net absorbed stellar flux (S_{abs}) is less than the Kombayashi-Ingersoll limit of the water vapor atmosphere ($F_{KI} \approx 282\,\mathrm{W\,m^{-2}}$), and no equilibrium state when $S_{abs} > F_{KI}$. For the Earth's atmosphere, the 1000 hPa of non-condensible components not only dilutes the atmosphere, but also leads to the sub-saturation of the upper troposphere and therefore increases the maximum amount of energy the planet could emit into space ($F_{max} \sim 320\,\mathrm{W\,m^{-2}}$ shown in Extended Data Figure 3b in Leconte et al. (2013)). Hence, two equilibrium states exists when $F_{KI} < S_{abs} < F_{max}$: one is stable and another unstable. In a real water-vapor atmosphere, the planetary albedo depends on T_s as well. Leconte et al. (2013) show a downward trend of the planetary albedo in a dilute atmosphere as the planet warms. For a non-dilute atmosphere, the planetary albedo is primarily determined by the Mie scattering of water clouds and Rayleigh scattering and absorption of water molecules. The latter effect can be easily computed, but the former one is not for we still know little about the cloud microphysics when the atmosphere is non-dilute. If the planetary albedo is a strongly non-linear function of T_s, then more equilibria (possibly stable) may exist in the non-dilute atmosphere. In fact, when applying the relation between the planetary albedo and T_s estimated in a 1D model (Figure 3b in Kopparapu et al. (2013)), there would be another stable equilibrium state with $T_s \sim 400\,\mathrm{K}$ under our current insolation. Goldblatt (2015) carried out a similar analysis and showed both a cold ($270 \lessapprox T_s \lessapprox 290\,\mathrm{K}$) and hot ($350 \lessapprox T_s \lessapprox 550\,\mathrm{K}$) stable climate state for a pure water atmosphere.

CHAPTER 5

THREE-DIMENSIONAL SIMULATION ON SLOWLY AND SYNCHRONOUSLY ROTATING PLANETS

5.1 Introduction

In Chapter 4, we study the climate of condensible-rich atmospheres on rapid rotators, and Exo-FMS model proves to be a useful tool. It is also important to explore the non-dilute atmospheres in a different climate regime – on slowly and synchronously rotating (tidally locked) terrestrial planets because such planets are common around low-mass M-dwarfs and the atmospheres on these planets will be able to be characterized by near-future telescopes such as the *James Webb Space Telescope*.

Pioneer work has been done to develop new theories for understanding the potential atmospheres on these planets and interpreting future observations. For dry atmospheres, Koll and Abbot (2016) developed a radiative-convective-subsiding model that explains the temperature structure and atmospheric circulation of dry, tidally locked rocky exoplanets. For moist atmospheres, most work focus on Earth-like thick atmospheres with condensible water vapor in the habitable zone of M-dwarfs. Yang et al. (2013) first used a full 3D global climate model to study the H_2O runaway greenhouse on tidally locked planets, and then construct an idealized two column model to reproduce the GCM results in Yang and Abbot (2014). One interesting phenomenon in their work is that when a tidally-locked habitable planet approaching the runaway greenhouse state, the night hemisphere starts to emit more thermal radiation than the dayside seen from the broadband thermal phase curve. Such a reversal of thermal emission between dayside and nightside is unlikely to be produced by a dry atmosphere on tidally locked terrestrial planets (Koll and Abbot, 2015). If detected on a potentially habitable planet, it indicates two important features of the planetary atmosphere: (1) the emergence of high-level cirrus clouds associated with deep convection; (2) the cold trapping mechanism of water vapor is weakened so that optically opaque water vapor is allowed to build up in the night hemisphere and the nightside emits thermal radiation from the mid-troposphere instead of the surface (Yang and Abbot, 2014). The former one confirms the presence of water vapor and the associated phase transition, while the latter one precludes water vapor as a minor constituent in the atmosphere.

The simulation described above in Yang et al. (2013) is only designed for a specific kind of atmosphere that is warm and thick with surface temperature (T_s) of 320 K and background N_2 partial pressure of 1 bar. The corresponding saturation mass concentration is only $\sim 10\%$, thus the cold trap would still take effect if cold enough. Another reason that weakens the cold trap in their simulation is the high temperature at the cold trap ($\sim 270\,\mathrm{K}$) due to the strong near-infrared (NIR) absorption by water vapor. Then the mass concentration of water vapor at the cold trap reaches 3%, which is high enough to transport large amount of water vapor to the nightside. How raising the surface temperature and cold trap temperature affect the cold trapping mechanism have been illustrated in Figure 1.3. Figure 1.3 also shows that the cold trap could be greatly weakened by just removing the non-condensible constituent from the atmosphere, even when both the surface and the cold trap are cold. We have also seen this effect in both the 1D simulations in Chapter 2 and the 3D simulations in Chapter 4.

In this Chapter, we continue to use the Exo-FMS model to study the thin condensible-rich atmosphere with an ineffective cold trap on slowly and synchronously rotating planets. Whether such thin atmosphere could show similar climate features (e.g., the reversal of thermal emission between the dayside and nightside) as the warm and thick one simulated by Yang et al. (2013) will be addressed.

5.2 Simulation Design

Our simulation design is basically the same as the study of condensible-rich atmospheres in Chapter 4, except that the planet is now synchronously rotating with the orbital period of 50 Earth days. Recall that our gray-gas radiation scheme includes neither the shortwave absorption of the insolation nor the radiative effect of clouds since it is easier to isolate the dynamic effect by taking away the noncondensible inventory. The radiative effect of water vapor in NIR and clouds will be discussed later.

To weaken the cold trap of water vapor, the surface partial pressure of the non-condensible N_2 (hereafter denoted as p_{a0}) is chosen to be 3,000 Pa, which is close to the saturation water vapor pressure corresponding to the substellar surface air temperature (∼300 K). To reach similar H_2O mixing ratio at the surface in thicker atmospheres, the corresponding surface temperature is 373 K if p_{a0}= 1 bar; and 590 K if p_{a0}= 10 bar. Both are high enough to trigger the runaway greenhouse. To investigate how the cold trapping of water vapor affects the climate, another two simulations with $p_{a0} = 10^5, 10^6$ Pa are carried out. In all of the three simulations, the fixed insolation and background longwave optical opacity are employed to maintain similar surface temperature distribution. The results we present are averages over the last 600 days of 3000-day integrations.

5.3 Dynamic Effects of Water Vapor

Figure 5.1a shows the vertical distribution of water vapor mass concentration (hereafter denoted as q) over the planet in the non-dilute simulation when p_{a0}= 0.03 bar including the dayside deep convective region and the nightside large-scale subsidence region. First, in the dayside deep-convective region, the red curves in Figure 5.1a mostly follow the corresponding moist adiabats. Compared to the dilute simulation when p_{a0}=1 bar in Figure 5.1c, the vertical variation of q is much smaller. This weak vertical gradient of q shows that the weaker vertical temperature gradient on a nondilute moist adiabat has drastically reduced the cold trapping. This weak vertical variation in a thin atmosphere is similar to that simulated in the thick and warm atmosphere shown in the log-pressure coordinate, as a consequence of the nature of the moist adiabat. For moist adiabats, the vertical slope of q ($\mathrm{d}q/\mathrm{d}\ln p$) is a decreasing function of both $1/T$ and q, and thus has a weak temperature dependence, but strong moisture dependence (Pierrehumbert, 2010; Ding and Pierrehumbert, 2016). Since the slope of q does not directly depend on the background non-condensible partial pressure,

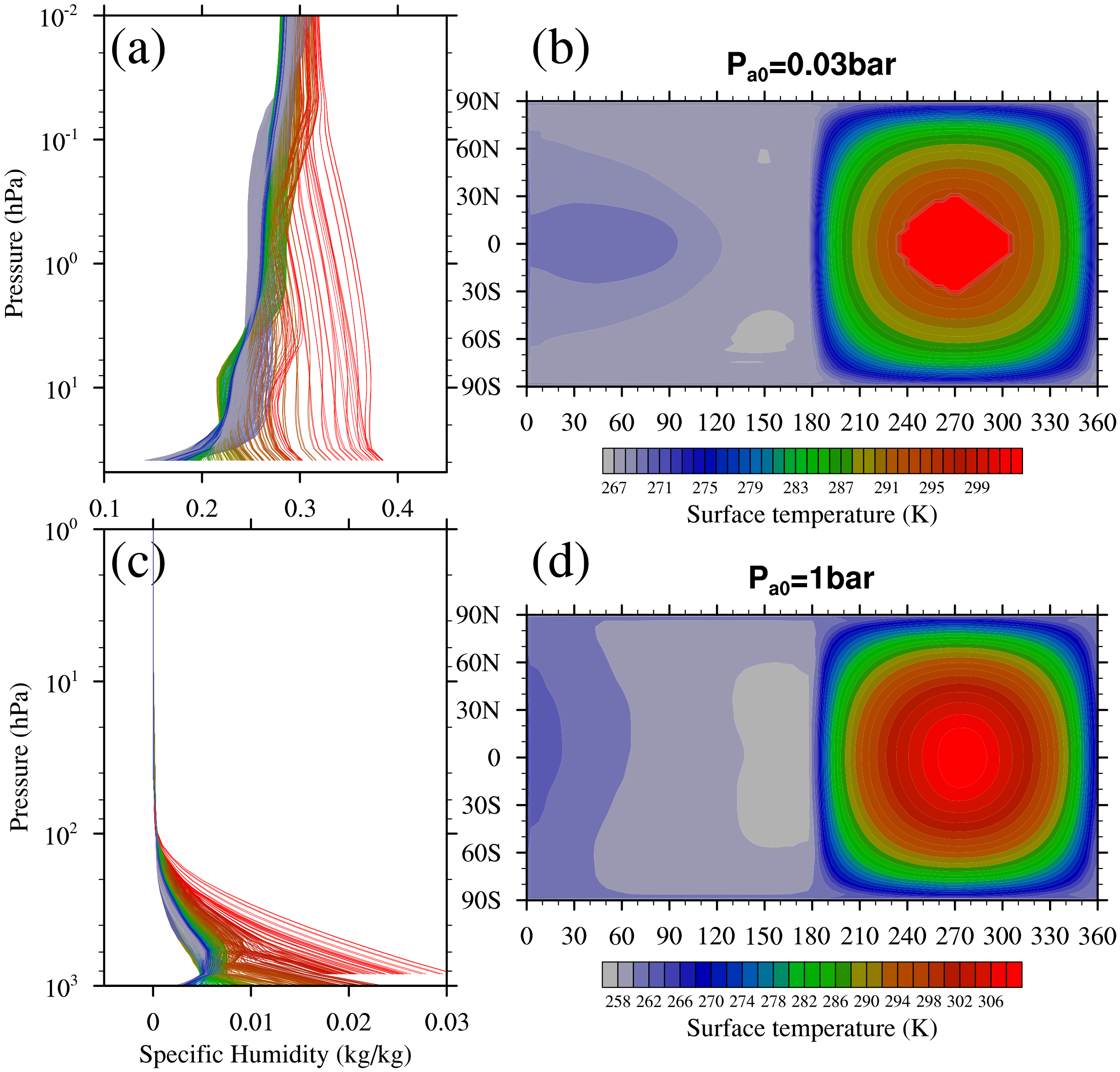

Figure 5.1: Upper panel: (a) the vertical profiles of the mass concentration of water vapor in the atmosphere and (b) the surface temperature distribution when p_{a0}=0.03 bar. Lower panel: same as the upper panel, but for p_{a0}=1 bar. The color of each profile in (a) and (c) is that of the corresponding surface temperature shown in (b) and (d), respectively. So red curves roughly represent the dayside deep convective region, while blue and gray curves represent the large-scale subsidence region.

the vertical distributions of q along moist adiabats with the same surface q are similar no matter the atmosphere is thick or thin.

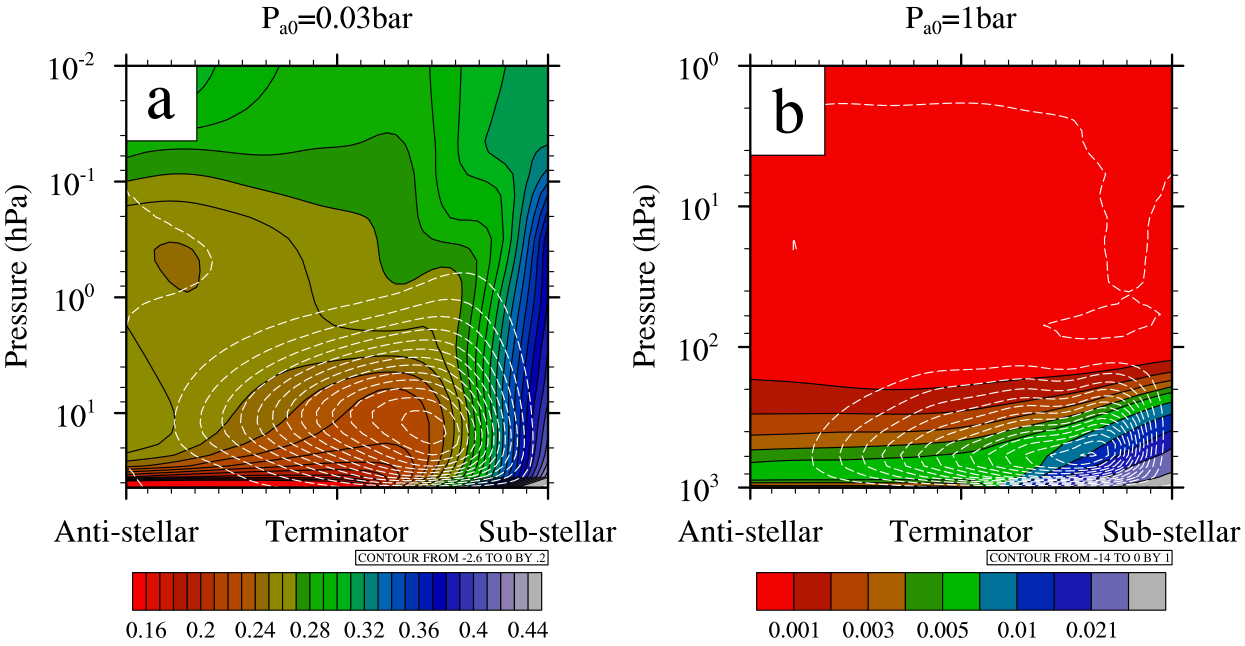

Figure 5.2: (a) Zonal-mean cross section of the specific humidity (color filled contours) and the meridional mass streamfunction (white dashed contours) in the tidally locked coordinate when p_{a0}=0.03 bar. (b) Same as (a), but for p_{a0}=1 bar. In both panels, a time-mean and zonal-mean counterclockwise circulation rising from the sub-stellar point is illustrated by the streamfunction.

Second, as the cold trapping of water vapor is weakened, the nightside atmosphere becomes water-rich. To better understand this distribution, the large-scale atmospheric circulation should be investigated. For slowly-rotating tidally-locked terrestrial planets, the atmospheric circulation is primarily dominated by a global thermally-direct overturning circulation that rises from the hot substellar region (white dashed contours in Figure 5.2), and superposed by perturbations due to large-scale planetary waves (Merlis and Schneider, 2010; Koll and Abbot, 2016), except for the condensible-dominated atmosphere. In addition, the weak Coriolis force usually leads to quite horizontally uniform temperatures in the free atmosphere (see discussion on WTG in Section 4.2.1). For the run with thinnest atmosphere (p_{a0}=0.03 bar), WTG still roughly applies with hemisphere-averaged air temperature difference less than 5 K in the troposphere between the day and night side. As a result of the overturning circulation, most of the air in night hemisphere has to pass through the substellar tropopause – the driest place in the free atmosphere due to the WTG approximation. So the substellar tropopause behaves as a cold trap of water vapor. After the air parcel leaves the cold trap, condensation never occurs until it approaches the strong temperature inversion layer near the nightside surface. In this case, water vapor is no different from a passive tracer, and its concentration in an air parcel is conserved along any segment of a trajectory assuming weak mixing with neighboring parcels. This concept of advection-condensation model was used to reconstruct the relative humidity in the Earth's subtropics by large-scale wind and temperature fields, and showed excellent agreement with satellite observations (Pierrehumbert and Roca, 1998). Similar reasoning explains the vertical q distribution on the nightside as the gray curves in Figure 5.1a shows: q roughly remains uniform between the top of the model and 10 hPa; as the air continues to subside and reaches the low-level temperature inversion layer, condensation occurs again and q starts to decrease resulting in the red relatively dry region in Figure 5.2a.

The advection-condensation model is also roughly illustrated in Figure 5.2 by overlaying the zonal-mean cross section of q with the meridional mass streamfunction in the tidally-locked coordinate (see Appendix B in Koll and Abbot (2015) for details about the tidally-locked coordinate). Within 30° around the substellar point, the contours of q intersect with the streamlines due to condensation. As the air parcel leaves the upwelling branch of the overturning circulation, the contours of q start to coincide with the streamlines. Note that the results in Figure 5.2 are for the time and zonal mean, so that the advection-condensation model does not apply perfectly in Figure 5.2 because of perturbations due to large-scale planetary waves. In fact, our simulation on the non-dilute atmosphere in Figure 5.2a shows many interesting dynamic features other than a simple overturning circulation. The large-scale planetary waves are highly variable in time and are likely convectively-coupled inertial-gravity waves, which makes it difficult to summarize the statistics of air parcel trajectories. In addition, upwelling motion associated with the inertia-gravity wave occurs on the nightside at times, which further cools and dehydrates the atmosphere. In this case, the nightside low-level temperature inversion layer serves as another cold trap of water vapor.

5.4 Broadband Thermal Phase Curves

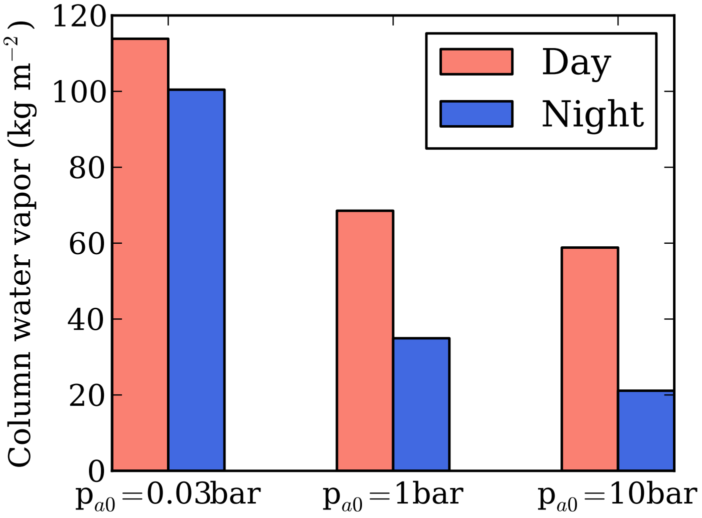

Figure 5.3: The vertically integrated mass of water vapor averaged over the day and nightside hemisphere, when p_{a0}= 0.03, 1, 10 bar, respectively.

To investigate the observational consequence of the climate with weak cold-trap, we focus on the broadband thermal phase curve around 10 μm where most energy of the terrestrial radiation is located. In this spectral region, the atmospheric absorption is mainly caused by water vapor self-induced continuum. Again, like the slope of the moist adiabat, self-induced continuum depends little on what the background air pressure is, but on the vertical integration of water vapor mass.

Figure 5.3 shows the column-integrated mass of water vapor averaged over the day and night hemisphere, respectively. First, the contrast of column water vapor mass between day and night hemisphere decreases as the atmosphere is thinner and the cold trap becomes less effective. This trend is linked to the change of the vertical slope of moist adiabat discussed in Section 5.3, and has direct impact on the contrast of thermal emission between day and night hemisphere, which will be discussed later. Next, the column water vapor mass on the dayside increases as the atmosphere is thinner. It may seem contour-intuitive, but in fact is also related with the fact that water vapor is a non-dilute component in the atmosphere. To show it in a simple way, we assume that the profile of the entire atmosphere is governed by moist adiabat. Then the column water vapor mass can be approximately written as

$$m_v \approx \int_0^{p_s} q \ \mathrm{d}p = \int_0^{T_s} f(r, 1/T) \ \mathrm{d}T, \qquad r = p_v/p_a \tag{5.1}$$

where q and r are the mass concentration and volume mixing ratio of water vapor, and $f(r, 1/T)$ is an increasing function of both r and $1/T$. The three runs in Figure 5.3 have similar temperature range, but volume mixing ratio varies over several orders of magnitude, which makes the thinner atmosphere in fact contain more water vapor.

As mentioned above, Exo-FMS model uses a two-stream gray gas radiation scheme because it is computationally cheap and meanwhile the simulation result is similar to that with realistic radiation schemes. The model is also cloud-free since we focus on the most basic dynamical implications without confronting all the issues of cloud microphysics in nondilute atmospheres. However, the cloud formation can be diagnosed by the condensation profile of water vapor in our numerical simulations. For example, the deep convection within 30° around the substellar point when p_{a0}=0.03 bar indicates the formation of high-level cirrus clouds there, and the near surface condensation in the night hemisphere indicates the formation of low-level stratus clouds. In this section, we will first investigate the radiative property of the weak cold-trap climate with a realistic radiative model and then take into account the radiative effect of clouds. This neglects the feedback of clouds on the circulation, but it is commonly done in exoplanet studies, such as the work on hot Jupiter clouds by Parmentier et al. (2016).

We calculate the broadband thermal phase curve in three bands which center at 1000, 850 and 600 cm^{-1} with bandwidth of 50 cm^{-1}, respectively. In these spectral ranges, the water

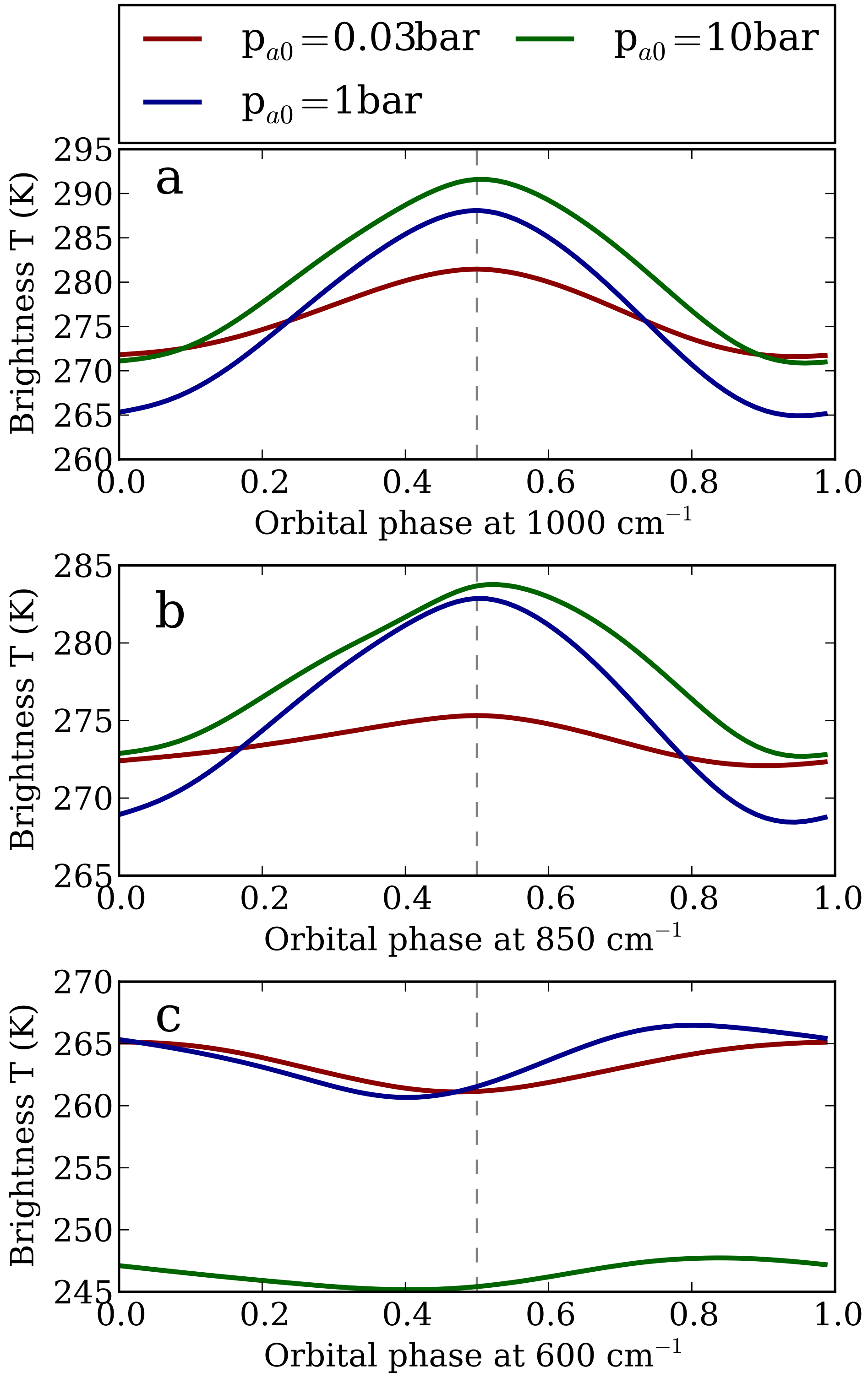

Figure 5.4: Broadband thermal phase curve expressed as the brightness air temperature at three spectral bands when p_{a0}=0.03 bar (red), 1 bar (blue), 10 bar (green), respectively: (a) at 1000 cm^{-1}; (b) at 850 cm^{-1}; (c) at 600 cm^{-1}. The bandwidth of each band is 50 cm^{-1}. The gray dashed line in each panel marks the superior conjunction.

vapor self-continuum absorption is used with polynomial fit given by Pierrehumbert (2010). We first compute the disk-averaged radiative flux based on the 3D simulated temperature and humidity field, and then translate it into the brightness temperature, as shown in Figure 5.4. For water vapor self-continuum, the equivalent path is quartic in water vapor partial pressure, which makes the contrast of thermal emission between day and night hemisphere sensitive to the contrast of column-integrated mass of water vapor shown in Figure 5.3. For the weak cold-trap climate with p_{a0}= 0.03 bar, optically-opaque water vapor atmosphere can build up in both day and night hemispheres associated with the small contrast of column-integrated water vapor mass, which explains the small brightness temperature variations of the thermal phase curve in all three bands. On the contrary, when the cold trap is effective, the nightside is still water-poor, and the optically-thin atmosphere can only emit energy out from the cold surface [1] except in a very strong absorption band. In fact, the water vapor absorption at $600\,\mathrm{cm}^{-1}$ is so strong that the nightside is optically opaque within this band in all the three runs . As a result, Figure 5.4c shows that all three runs have small brightness temperature variations with a small degree of reversal in thermal emission between day and night hemisphere.

If the radiative effects of clouds were taken into account in the model, the thermal phase curve integrated over all frequencies of the weak cold-trap climate with thin and moderate atmosphere should show similar feature as the one of the thick and warm atmosphere simulated by Yang et al. (2013) because the cloud distributions in the two climates with weak cold-trap are similar. The near surface stratus clouds on the nightside would contribute little to the thermal emission because the emission of water vapor is roughly at the same level, while the high-level convective cirrus clouds on the dayside would reduce the thermal emission significantly so that a reversal between day and night hemisphere is expected.

---

[1] In fact, the day and night surface temperature contrast also depends on the opacity of water vapor on the nightside. An optically opaque atmosphere on the nightside will enhance heat transport from dayside to nightside and therefore cooling the dayside surface (Yang and Abbot, 2014).

5.5 Summary

In this Chapter, we use Exo-FMS to simulate thin condensible-rich atmosphere with a weak cold trap on a tslowly and synchronously rotating planet. Compared to the simulations on the thick and warm atmosphere by Yang et al. (2013), our simulation also shows the atmosphere is dominated by an overturning circulation with formation of substellar cloud and build up of water vapor on the nightside to make it optically opaque. Therefore we propose if the signal of reversal in the broadband thermal phase curve is detected on potentially habitable exoplanets, it is likely that the atmosphere have a weak cold trap which could be induced either in the thick and warm atmosphere as Yang et al. (2013) shows or in a thin atmosphere in our study. This signal also implies the total atmospheric pressure should be below a certain threshold related to the saturation vapor pressure at the surface to weaken the cold trap. It provides an additional way to constrain the surface pressure in exoplanet atmosphere if the surface or the low-level air temperature could be detected by other techniques.

However, our simulation on the thin atmosphere is not exactly dynamically analogous to the thick and warm case in Yang et al. (2013) in terms of the nondiluteness. There is stronger nondilute effect of water vapor in our simulation, and the contribution of water vapor on the air density and the atmospheric pressure becomes more important. One major consequence of the nondilute effect is if we continue to decrease the non-condensible inventory in the atmosphere to certain extent, the overturning circulation may not be maintained anymore because it requires the surface pressure gradient force pointing towards the day hemisphere against the surface friction. In this case, the circulation should reduce to the evaporation-driven flow that is dominated by low-level atmospheric transport from the hot dayside to the cold nightside. Our model cannot simulate such an abrupt transition due to numerical issues, but this new flow regime is of great interest and such a transition has never been simulated before.

Finally, it would be intriguing to consider whether such a mechanism also works in atmosphere with other condensible components, i.e, a condensing CO_2 atmosphere or rocky vapor atmosphere. The arguments applied to water vapor in this Chapter would apply equally to other condensible substances in a suitable temperature range. The CO_2 case is a good example. For a condensing CO_2 atmosphere, substellar clouds could also block the thermal emission effectively but by reflecting it back instead of absorbing and re-emitting (Forget and Pierrehumbert, 1997). But the planet with condensing CH_4 or N_2 atmosphere should be quite far from star, and cannot be tidally-locked anymore. Even if tidally-locked, it is unrealistic to observe the thermal phase curve of such a planet over a very tlong time period. For the hot counterpart, the rocky vapor atmosphere would be a good example. It is possible to form nondilute condensing sulfur atmosphere at the temperatures of 400 K or 500 K if the background non-condensible is thin enough. However, there are several problems with extremely hot rocky vapor atmospheres if the condensible substance is carbon, iron or enstatite ($MgSiO_3$). The strong shortwave absorption will increase the temperature at the cold trap significantly and may push the cold trap of the condensible substance to the ground, which leads to the disappearance of dayside clouds. This phenomenon has been seen in simulations on hot Jupiters (Parmentier et al., 2016) and on TRAPPIST-1d experiencing the H_2O runaway greenhouse (Wolf, 2017). Another issue is that the radiative timescale in the hot atmosphere may be so short that the atmospheric dynamics cannot maintain small temperature variations (Koll and Abbot, 2015, 2016). Then the dayside would still emit more energy out than the nightside even if the dayside is covered by thick high clouds. To sum up, the reversal between day and nightside thermal emission is a common feature of nondilute condensible atmospheres on tidally locked planets if the planets are not extremely hot.

CHAPTER 6

REVISITING THE DISTRIBUTION OF PURE-CONDENSIBLE ATMOSPHERES

6.1 Introduction

In Chapter 5, we discussed the dramatic transition from the overturning circulation to the evaporation-driven type flow if the nondilute effect is strong enough in condensible-rich atmospheres. The tipping point remains a complicated issue and cannot be solved at current stage. But studying the pure condensible atmosphere could be a first step to understand this transition.

We introduced previous studies on pure condensible atmospheres in Section 1.2. It has long been recognized that the pure condensible atmosphere could be either global with fractional surface pressure variation much less than order of unity as N_2 on Triton, or local as SO_2 on Io. The fractional variation of surface pressure was attributed to thickness of atmosphere (Trafton and Stern, 1983; Trafton, 1984). In this Chapter, we revisit this problem by means of the horizontal atmospheric energy transport with the emphasis on the latent heat transport. A non-dimensional parameter that determines the variation of surface pressure is derived from the energy budget of the pure condensible atmosphere.

6.2 Energy Budget on Planets with Pure-Condensible Atmospheres

We start from the energy balance at the top of the atmosphere (TOA) in the steady-state of a moist climate system – the net radiative flux at TOA should be balanced by the divergence of horizontal energy transport in the climate system including both in the atmosphere and the ocean (if there was). To simplify the problem, we ignore oceanic heat transport. The atmospheric energy transport is usually referred to as "moist static energy" transport, and is composed of three terms: (1) potential energy flux that is usually negligible in pure condensible atmosphere because most of the transport is carried by the low-level flow as discussed above; (2) sensible heat flux and (3) latent heat flux (Peixoto and Oort, 1992). For most common materials that condense in a stable climate system before entering the runaway greenhouse, the specific latent heat is usually much greater than the sensible heat. Therefore the latent heat flux that carried by the low-level flow should dominate the atmospheric energy transport, and the energy budget of the pure condensible atmosphere can be approximately written as

$$F_{\odot}(1-A) - OLR(T_s) \simeq \boldsymbol{\nabla}_h \cdot (L\boldsymbol{M}) \tag{6.1}$$

where the left hand side is the TOA radiative imbalance, and $L\boldsymbol{M}$ the atmospheric horizontal latent heat transport.

In some of previous studies of pure condensible atmospheres, the latent heat flux is ignored, e.g., SO_2 atmosphere on Io (Ingersoll et al., 1985) and the hypothetical rocky vapor atmosphere on close-in hot rocky exoplanets (Castan and Menou, 2011). In particularly thin atmospheres it does not cause any problem because the atmospheric energy transport is negligible compared to the radiative fluxes. However, more generally, the latent heat flux often dominates and should not be ignored. Even in the hottest atmosphere – the hypothetical condensing sodium atmosphere on hot rocky exoplanets t– the latent heat flux is still comparable to the sensible heat flux.

For pure condensible atmospheres, the clear-sky outgoing longwave radiation (OLR) only depends on the surface temperature (T_s) [1] that is related with the surface pressure (p_s) by Clausius-Clapeyron relation. Then the energy budget equation (Eq. 6.1) could be simplified as an ordinary differential equation on the spatial distribution of the surface pressure (p_s) because the surface momentum equation provides additional relation between p_s and the horizontal mass transport. In the next two sections, we will consider two specific orbital

---

[1] This is good assumption for cloud-free atmospheres. If the atmosphere is optically thin, then the OLR is the blackbody emission from the surface. If not, the temperature jump between the surface and the surface air would be small so that the OLR is still a function of T_s.

configurations of the planet, and further simplify the energy budget equation (Eq. 6.1) in the two different climate regimes to find how the surface pressure variation is controlled by the latent heat transport.

6.3 Slowly and Synchronously Rotating Planets

For slowly and synchronously rotating planets, it is convenient to use the tidally locked coordinate system (see Appendix B in Koll and Abbot (2015) for details) with tidally locked latitude $\theta_{TL} = 0$ at the terminator and $\theta_{TL} = \pi/2$ at the substellar point, because slow planetary rotation leads to zonally symmetric flows in the tidally locked coordinate. Then the energy budget equation and surface momentum equation are

$$\frac{1}{a\cos\theta_{TL}}\frac{\mathrm{d}}{\mathrm{d}\theta_{TL}}(\cos\theta_{TL} L v_s p_s/g) \simeq \begin{cases} F_a \sin\theta_{TL} - OLR(T_s), & \theta \in [0, \pi/2] \text{ (dayside)} \\ -OLR(T_s). & \theta \in [-\pi/2, 0] \text{ (nightside)} \end{cases} \tag{6.2}$$

$$\frac{RT_s}{p_s}\frac{\mathrm{d}p_s}{a\mathrm{d}\theta_{TL}} \simeq -\frac{v_s}{\tau} \tag{6.3}$$

where a is the radius of the planet, g the surface gravity, F_a the absorbed stellar radiation at the substellar point, and R the specific gas constant of the condensible volatile. Here we assume the planetary albedo is uniform on the dayside and thus is included in the absorbed stellar radiation F_a at the substellar point. We also assume that the surface pressure gradient force is mainly balanced by the surface friction that is represented by a linear damping of surface wind velocity and ignore the metric terms and the advection derivative of the surface wind. The radiative effects of clouds is again neglected. Given the relation between T_s and p_s by Clausius-Clapeyron relation, the spatial distribution of either surface temperature or pressure can be solved numerically by the 4th-order Runge-Kutta method.

Figure 6.1 shows an example of the solutions for the pure condensible H_2O atmosphere. Solution in Figure 6.1a under a higher insolation represents a warm and global H_2O atmosphere in an ocean world with surface pressure variation less than 1%, while the one in

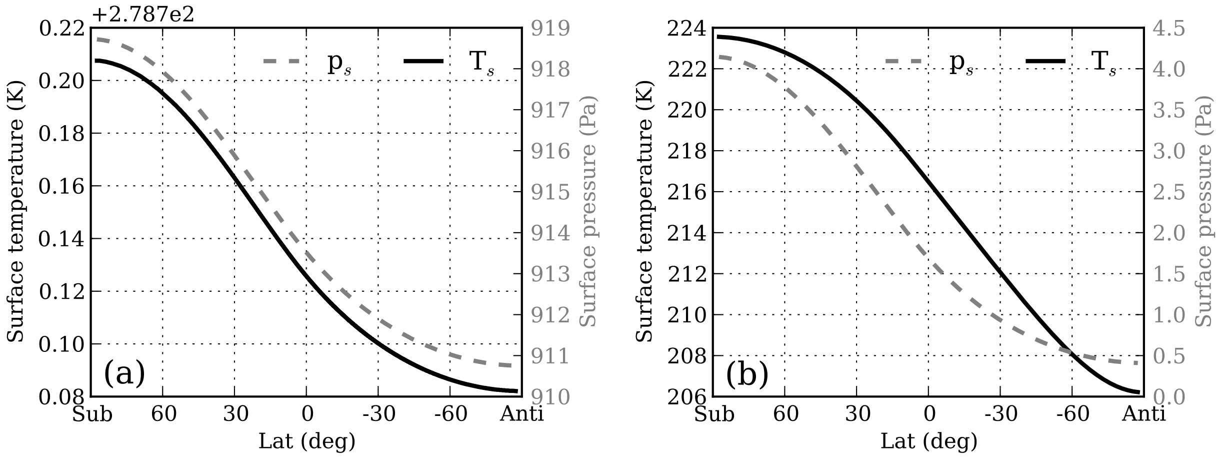

Figure 6.1: Meridional distribution of the surface temperature (solid black) and the surface pressure (gray dashed) in the tidally locked coordinate for the pure condensible H_2O atmosphere on a synchronously and slowly rotating planet, when (a) $F_a = 278\,\mathrm{W\,m^{-2}}$ and (b) $F_a = 125\,\mathrm{W\,m^{-2}}$, respectively. Other parameters chosen to solve the 1D differential equation are: $a = r_\oplus, g = g_\oplus, \tau = 1$ Earth day. The OLR of a pure condensible H_2O atmosphere is fit by a third degree polynomial based on the realistic H_2O radiative transfer calculation: $OLR(T_s) = 4704.16 - 61.957T_s + 0.26912T_s^2 - 3.7244 \times 10^{-4}T_s^3$.

Figure 6.1b represents a cold local atmosphere concentrated on the day side of an icy planet with surface pressure variation of $\sim$90%. These two solutions confirm that the atmospheric thickness dominates the latent heat transport that flattens the incoming differential radiative forcing, and plays an important role in the distribution of pure condensible atmospheres. The heat redistribution is still quite efficient when the substellar point is at the freezing point of water, which precludes the proposed 'Eyeball Earth' state (Pierrehumbert, 2011) on a slowly and synchronously rotating planet. In other words, the planet with pure condensible H_2O atmosphere should be either a global ocean worlds or a global icy worlds.

We will further explore the effect of atmospheric thickness by considering the limit of global atmosphere with weak temperature variations $\Delta T \ll T_s$. In this limit, the surface pressure gradient and the resulting horizontal heat transport could still be large enough to maintain the global atmosphere due to the Clausius-Clapeyron relation

$$\frac{1}{p_s}\frac{\mathrm{d}p_s}{\mathrm{d}\theta_{TL}} = \frac{L}{RT_s}\frac{1}{T_s}\frac{\mathrm{d}T_s}{\mathrm{d}\theta_{TL}} \tag{6.4}$$

because of the fact that $L/RT_s \gg 1$ for most condensing volatiles. Given the small surface temperature variation, $OLR \simeq F_a/4$, and then the fractional variation of p_s can be simplified as

$$\frac{1}{p_s}\frac{\mathrm{d}p_s}{\mathrm{d}\theta_{TL}} \simeq \begin{cases} \mathcal{M}\frac{\sin\theta_{TL}+\cos 2\theta_{TL}}{\cos\theta_{TL}}, & \theta \in [0, \pi/2] \text{ (dayside)} \\ \mathcal{M}\frac{\sin\theta_{TL}+1}{\cos\theta_{TL}}. & \theta \in [-\pi/2, 0] \text{ (nightside)} \end{cases} \tag{6.5}$$

where $\mathcal{M} = (F_a a^2 g)/(4LRT_s\tau p_s)$ is a non-dimensional parameter that can be used to distinguish whether the pure condensible atmosphere is global or local. Our assumption of global atmosphere here requires that $\mathcal{M} \ll 1$. On the contrary, if $\mathcal{M} \geq O(1)$, the pure condensible atmosphere should exhibit large pressure variations and become local around the mass source. Take the numerical solutions of the pure condensible H_2O atmosphere in Figure 6.1 as an example. For the global atmosphere solution in Figure 6.1a, $\mathcal{M} = 0.0044 \ll 1$; for the local atmosphere solution in Figure 6.1b, $\mathcal{M} = 1.218$.

The non-dimensional parameter $\mathcal{M}$ can be understood by being rearranged into the ratio of two timescales: $\mathcal{M} = t_{adv}/t_{evap}$, where $t_{evap} = (p_s/g)/(F_a/4L)$ is the characteristic time scale to build up the condensible atmosphere by evaporation under the global averaged insolation $F_a/4$, and $t_{adv} = a^2/(RT_s\tau)$ the characteristic time scale to transport the air mass from the dayside to the nightside. Small values of $\mathcal{M}$ means that the atmospheric transport is fast enough to redistribute air mass from the hot place to other region and thus results in a global atmosphere, and vice versa.

Ingersoll (1990) suggested a similar non-dimensional parameter to distinguish the pure condensible atmosphere, $\mathcal{M}_{\mathcal{I}} = (F_a g a/4p_s L)/c_s$, where the numerator is the velocity scale at the terminator estimated by assuming half of the evaporated mass on the dayside should be transported to the nightside in a global pure condensible atmosphere, and the denominator the speed of sound corresponding to the global surface temperature. Our proposed non-dimensional parameter can also be rearranged in a similar way, $\mathcal{M} = (F_a g a/4p_s L)/v_s$. The only difference is that the denominator here is the characteristic velocity scale if the atmosphere is local and the fractional variation of the surface pressure is $O(1)$ rather than the speed of sound, while the numerator is the same as the one defined in $\mathcal{M}_{\mathcal{I}}$ – the required mass transport to maintain a global pure condensible atmosphere .

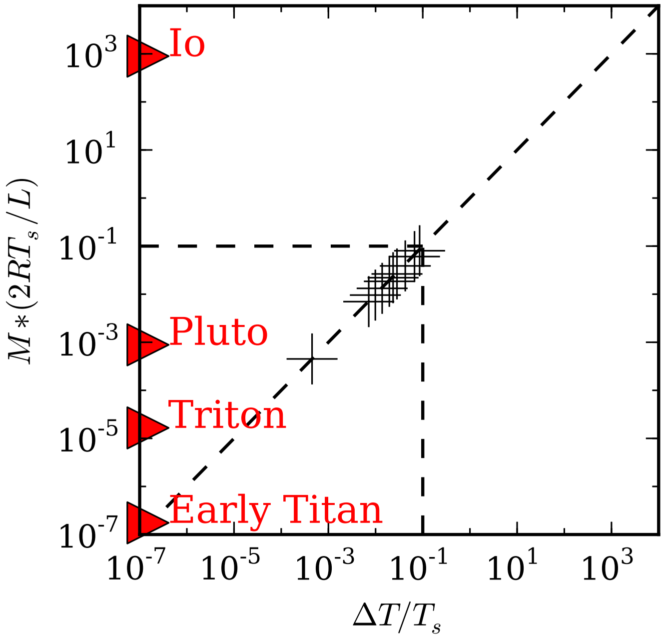

Figure 6.2: Fractional change of the surface temperature $\Delta T/T_s$ in the pure condensible H_2O atmosphere between the substellar point and the antistellar point under various values of insolation between 125 and 278 $\mathrm{W\,m^{-2}}$. The numerical solutions are marked by plus signs. The vertical axis is the non-dimensional parameter $\mathcal{M}(2RT_s/L)$ of each numerical solution, which should be close to $\Delta T/T_s$ for small values of $\mathcal{M}$. The non-dimensional parameter $\mathcal{M}(2RT_s/L)$ of several planetary bodies with pure condensible atmospheres are estimated and marked on the vertical axis.

The non-dimensional parameter $\mathcal{M}$ can also be used to estimate the surface temperature variation (ΔT_s) of the global pure condensible atmosphere by integrating Eq (6.5) from the substellar point to the antistellar point, $\Delta T/T_s \simeq \mathcal{M}(2RT_s/L)$. We calculate the numerical solutions of the fractional change of the surface temperature $\Delta T/T_s$ in the pure condensible H_2O atmosphere under various values of insolation between 125 and 278 $\mathrm{W\,m^{-2}}$, shown in Figure 6.2. It is interesting that the parameter $\mathcal{M}(2RT_s/L)$ gives an accurate estimate of surface temperature variation not only for small values of $\mathcal{M}$ but also when $\mathcal{M}$ approaches order of unity. We also tried to estimate the value of $\mathcal{M}(2RT_s/L)$ for several planetary bodies with pure condensible atmospheres. It is difficult to estimate the linear damping timescale of surface velocity on these planetary bodies because of the complexity of surface conditions (e.g., boundary layer turbulences). Here we simplify the problem by fixing it at 1 Earth day. Nevertheless, the estimate still coincides with either observations or numerical simulations: the condensing N_2 atmosphere on Triton, on Pluto (Zalucha, 2016), and possibly on Early Titan (Charnay et al., 2014) should have small surface temperature variations; the condensing SO_2 atmosphere on Io should have large surface temperature variation that is comparable to the magnitude of the substellar surface temperature as assumed in Ingersoll et al. (1985). The magnitude of $\mathcal{M}$ on these planetary bodies are primarily determined by that of p_s as discussed in Trafton and Stern (1983) and Trafton (1984), and therefore is ultimately determined by the absorbed stellar radiation. Other parameters in $\mathcal{M}$ on these planetary bodies do not vary too much.

The hot rocky atmospheres that should also have large surface temperature variations (Castan and Menou, 2011) are not shown in Figure 6.2 for two reasons. First, the parameter $\mathcal{M}(2RT_s/L)$ is extremely large due to the high insolation on the close-in rocky exoplanets; Second, the close-in exoplanets, although tidally locked, are fast rotators so that the flow features are more complicated and are not zonally symmetric in the tidally locked coordinate. We discussed the possible mechanism of the barotropic adjustment in the atmosphere that could damp out the surface pressure variation and hence results in a horizontal heat transport in Section 4.2.2.

6.4 Fast-Rotating Planets with Zonally Symmetric Radiative Forcing

On fast-rotating planets, the Coriolis force becomes important in the atmospheric dynamics. We further simplify the problem by assuming that the surface reservoir has a thermal inertia that is large enough to damp out the diurnal cycle, so the atmospheric flow is zonally symmetric in the geographic coordinate system. Then the meridional atmospheric transport that redistribute mass, momentum and energy is characterized by the Ekman transport in the frictional boundary layer. In the geographic coordinate system, the energy budget equation (Eq.6.1) becomes

$$\frac{1}{a\cos\theta}\frac{\mathrm{d}}{\mathrm{d}\theta}\left(\cos\theta L M_E(\theta)\right) \simeq F_a\cos\theta/\pi - OLR(T_s(\theta)). \tag{6.6}$$

where θ is the geographic latitude, $M_E(\theta)$ the meridional Ekman mass transport, and F_a still the absorbed stellar flux at the substellar point. Assuming that the frictional force in the Ekman layer is parameterized by a constant eddy viscosity A, the Ekman mass transport can be described by the product of the layer thickness and the zonal geostrophic wind speed (Vallis, 2006, p. 112), and thus is related to the meridional surface pressure gradient,

$$M_E \simeq -\frac{1}{4a\Omega}\sqrt{\frac{A}{\Omega}}(\sin^{-3/2}\theta)\frac{\mathrm{d}p_s}{\mathrm{d}\theta} \tag{6.7}$$

where Ω is the spin rate of the planet. Similar to the discussion about the synchronously and slowly rotating planets, the meridional distribution of either the surface temperature and the surface pressure can be solved numerically, and a non-dimensional parameter can be derived to distinguish whether the pure condensible atmosphere is global or local, $\mathcal{M}_{\mathcal{F}} = \sqrt{\Omega/A}(F_a a^2\Omega)/(4Lp_s)$. Compared to the non-dimensional parameter defined in the synchronously and slowly rotating case, $\mathcal{M}_{\mathcal{F}}$ has the same dependence on the insolation, the radius of the planet, the specific latent heat and the surface pressure. But $\mathcal{M}_{\mathcal{F}}$ is independent of the gravity because the Ekman transport has no dependence on the gravity. Similarly, $\mathcal{M}_{\mathcal{F}}$ can also be rearranged as the ratio of the mass transport to maintain a global pure condensible atmosphere to the one if the atmosphere is local and the fractional variation of the surface pressure is $O(1)$.

We showed the 3D Exo-FMS simulation of the pure condensible H_2O atmosphere on a rapidly-rotating planet in Chapter 4. The meridional distribution of T_s is given by the black dashed curve in Figure 6.3. We then solve the 1D energy budget equation using

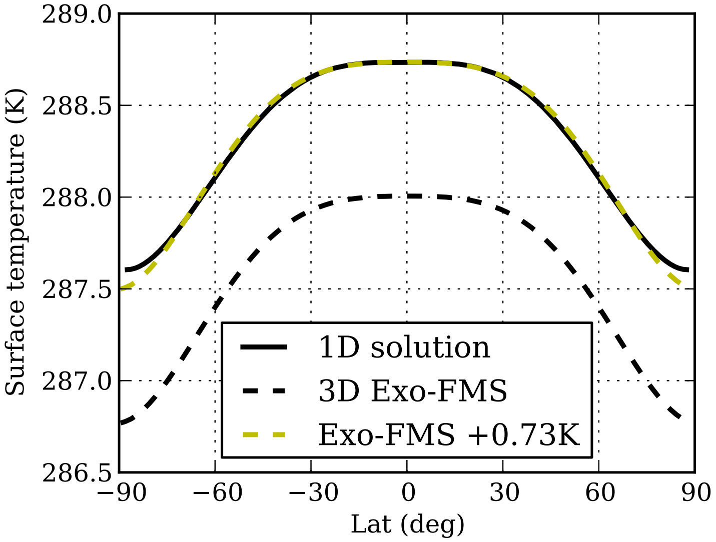

Figure 6.3: Meridional distribution of the surface temperature for the pure condensible H_2O atmosphere on an Earth-like fast-rotating planet. The black solid curve represents the solution of the 1D energy budget equation, and the black dashed one the solution given by 3D general circulation model in Pierrehumbert and Ding (2016). The 1D solution is generally 0.73 K higher than the 3D solution due to the energy imbalance of the GCM, which is marked by the yellow dashed curve. Parameters chosen to solve the 1D differential equation are: $a = r_{\oplus}, g = g_{\oplus}, F_a = 1260\,\mathrm{W\,m^{-2}}, A = 100\,\mathrm{m^2\,s^{-1}}$. The OLR of the pure condensible H_2O atmosphere is given by a linear fit based on the gray radiation scheme in the 3D GCM: $OLR(T_s) = 17.53 + 1.032T_s$.

the same input parameters and a typical value of the boundary layer eddy viscosity $A = 100\,\mathrm{m^2\,s^{-1}}$. The 1D solution (black solid curve in Figure 6.3) is generally 0.73 K higher than the 3D solution due to the energy imbalance of the GCM ($\sim 0.75\,\mathrm{W\,m^{-2}}$), but has the same curvature as the 3D solution. This result confirms that under certain circumstances, the simple 1D solution of the energy budget equation could reproduce the result given by more comprehensive 3D models, and the 1D energy budget equation is a useful tool to study pure condensible atmospheres.

6.5 Detection and Discrimination of Circulation Regime

The evaporation-driven flow is a totally different circulation regime compared to the overturning circulation described in Chapter 5, but may generate similar observed features. For example, our simulation on the global pure condensible H_2O atmosphere on potentially tidally-locked exoplanet should generate a flat thermal phase curve. A thick atmosphere with moderate amount of water vapor that is dominated by an overturning circulation could also generate the same signal (Yang et al., 2013).

However, if non-condensible radiatively-active substance exists as a minor constituent in the global pure-condensible atmosphere, a unique observational signal could be detected. As the consequence of the evaporation-driven flow in the pure condensible atmosphere, the non-condensible substance should accumulate near the antistellar point. This inhomogeneous distribution of the non-condensible substance induced by the atmospheric dynamics makes the thermal phase curve in the spectral region where the non-condensible substance absorbs reach the minimum at the antistellar point. In addition, the lack of absorption features of the non-condensible substance detected by high-resolution spectroscopy could also imply such an inhomogeneous distribution. We propose that these observation features very likely indicate a global pure condensible atmosphere, if detected in the future. In fact, the current technique is able to help us study the atmospheric circulation in condensible-dominated atmospheres by the distribution of non-condensible minor constituent. Sprague et al. (2007) studied the atmospheric argon (Ar) measurements in Mars' atmosphere from the gamma ray spectrometer on the Mars Odyssey spacecraft, and they found a significant enhancement of Ar over the south polar latitudes occurring near the onset of the southern winter and rapid seasonal variations in Ar from 60°S to 90°S that might be the evidence for wave activities.

The existence of the global pure condensible atmosphere can also be verified by the non-dimensional parameter $\mathcal{M} = (F_a a^2 g)/(4LRT_s \tau p_s)$ discussed in Section 6.3. Again, our arguments here applies to not only water vapor but also other condensible substances in a suitable temperature range.

CHAPTER 7

CONCLUSION

Our goal is to explore the climate dynamics of condensible-rich atmospheres in general. We develop a hierarchy of flexible, intermediate complexity models, with focus on the dynamical effect in nondilute atmospheres. Several simplifications are made in the models to suppress feedbacks we do not focus at this stage. First, we use a gray-gas radiation scheme with no shortwave absorption and pressure broadening. Second, the simplified moist convection scheme uses minimal number of free parameters. Third, the surface only behaves as a thermal and moisture reservoir and is a blackbody that absorbs all incoming radiative fluxes.

We began in Chapter 2 by developing a simple energy-conserving convection parameterization which works across atmospheres ranging from those in which the condensible substance is a dilute component of the atmosphere to those with strongly nondilute condensibles. The parameterization is currently limited to a single condensible substance in a noncondensible background mixture of gases, but it can be applied to any combination of the two classes of components, given suitable adjustment to thermodynamic parameters.

In Chapter 3 the performance of the parameterization has been tested within a single-column radiative-convective model. Although our parameterization on moist convection is not the first attempt to treat atmospheres with nondilute condensibles, we have endeavored to use the formulation of the parameterization as a vehicle to give a thorough discussion of the nature of energy conservation in nondilute atmospheres, and the various ways in which moist convection in such atmospheres differs from the more familiar dilute limit. Key features include transport of significant amounts of energy and mass by precipitation (especially in the course of the seasonal cycle when the atmosphere is out of equilibrium), the suppression of deep buoyant plumes in favor of a more gentle gradual ascent, and the feedback of precipitation and evaporation/sublimation on surface pressure (a feature already familiar from the current Martian atmosphere). The single-column simulations were conceived primarily as a test of the conservation properties of the scheme, but in addition to illustrating some general features of nondilute convection, demonstrated that nondilute atmospheres can have a very strong damping effect on seasonal cycles driven by even extreme seasonal variations in instellation. In principle, the large proportion of condensible substance present in nondilute atmospheres could lead the energy transport by condensate to dominate the behavior of the system. In all the cases we have examined, however, the energy carried by condensate, while a significant term needed to enforce energy conservation, is of fairly modest magnitude in the annual mean. This property arises from energetic limits on precipitation rate: in essence, one cannot release latent heat at a rate faster than it can be cooled down by emission of infrared radiation, and so the large latent heats of most condensible substances tend to yield limited mass of precipitation.

We then develop an idealized 3D general circulation model (Exo-FMS) incorporating the single column model, and use it to study condensible-rich atmospheres on rapidly rotating planets in Chapter 4. Given the vast amount of energy stored as latent heat in nondilute atmospheres, one might expect them to exhibit violent behavior, with extreme convective storms perhaps reducing pressures locally to a near vacuum as massive proportions of the atmosphere rain out. In fact, we have found strongly nondilute atmospheres to be rather quiescent places, with largely barotropic dynamics, weak temperature gradients, sluggish circulations, and rather gentle laminar ascent in convective regions instead of the boiling cumulus towers familiar from the Earth's tropics. All of these features can be understood in terms of well-established thermodynamic and GFD principles applied in a novel way. Ironically, it may be difficult or impossible for hurricanes to form in highly nondilute atmospheres. The quiescent nature of nondilute atmospheres is already suggested by the example of Titan, which has rather weak condensationally-driven activity in its troposphere despite the very considerable amount of energy stored in the form of latent heat of condensible methane – vast amounts of energy are there, but the dynamics can't get at it. Titan, however,is weakly illuminated and slowly rotating, which may also play a role in its quiescent (though nonetheless interesting) dynamics. We have shown that similar behavior emerges even in rapidly rotating cases with Earthlike instellation.

An important result obtained from our simulations is that atmospheres become increasingly saturated throughout a deepening layer as they become more nondilute. This has critical implications for the conditions which support a runaway greenhouse for water vapor or other condensible greenhouse gases, as dilute atmospheres can be inhibited from entering into a runaway by subsaturation. The increasing saturation with temperature we have found also confirms earlier speculations that the feedback of increasing relative humidity can potentially lead to multiple equilibria, in which atmospheres can have a metastable non-runaway state and a hot runaway state for the same instellation conditions (though our simulations do not themselves exhibit this multiplicity). An important implication of our results on saturation is that a substantial inventory of noncondensing background gas helps to protect a planet against a runaway greenhouse, through allowing significant subsaturation. This effect is of interest not just for water oceans, but also for the preservation of CO_2 oceans, which are of current interest as a possible alternative life-supporting environment.

Though in some sense sluggish, nondilute atmospheres nonetheless exhibit a variety of novel and challenging dynamical phenomena. Angular momentum carried by precipitation allows global or near-global surface westerlies to prevail. One can raise related questions about the way nondilute precipitation affects potential vorticity dynamics. Compositionally induced pressure gradients allow strong baroclinic jets even when horizontal temperature gradients are weak, but these jets appear to be stable against baroclinic instability. The width of the weak nondilute Hadley circulations remains to be understood, and the tropics of nondilute atmospheres exhibit a variety of large scale transient convective clusters whose dynamics remain to be elucidated; they are likely to have a strong influence on the cloud patterns of nondilute atmospheres.

We next use Exo-FMS to study condensible-rich atmospheres on slowly and synchronously rotating planets. Our simulation shows formation of high-level clouds near the substellar region and build up of the condensible on the nightside to make it optically opaque if the cold trap is weak enough. Such particular nondilute climate pattern leads to the reversal of thermal emission between the dayside and nightside that can be observed by the broadband thermal phase curve. This signal is also seen in previous simulations on thick and warm atmospheres approaching the H_2O runaway greenhouse by comprehensive GCMs (Yang et al., 2013; Wolf, 2017). Our study confirms that the reversal of thermal emission between the dayside and nightside indicates a moist climate with a weak cold trap; however, our simulation have a much stronger nondilute effect compared to other studies. One problem with the nondilute effect is that for even higher moisture concentration, the overturning circulation that governs the atmospheric circulation cannot be maintained and will be reduced to a completely different circulation regime, similar to the evaporation-driven flow in the pure condensible atmosphere. There is no simple theory on this tipping point. An easier approach to explore the transition may be from the other side of the pure condensible atmosphere.

In Chapter 6 we use 1D energy budget model to study pure condensible atmospheres. A non-dimensional parameter is derived from the 1D energy budget equation that determines whether the pure condensible atmosphere is global or local in two different climate regimes when the planet is slowly and synchronously rotating and fast rotating, respectively. In both cases, the non-dimensional parameter could be expressed as the ratio of the mass transport required to maintain a global atmosphere to the one if the atmosphere is local with fractional surface pressure variation $\sim O(1)$. The global pure condensible atmosphere with the non-dimensional parameter much less than order of unity is maintained by the strong horizontal latent heat transport from warm to cold places that flattens the incoming differential radiative forcing. We show that the simple 1D model can reproduce the 3D simulation on the pure condensible H_2O atmosphere by Exo-FMS shown in Chapter 4, and the 1D energy budget model proves to be a useful tool to study the evaporation-driven flow regime. So we propose that the transition of circulation regime could be explored by the simple 1D energy budget model by making the pure condensible atmosphere more dilute. We do not cover the complete calculation in Chapter 6. Instead, we discuss the limit of condensible-dominated atmosphere with minor non-condensible constituent. In a global condensible-dominated atmosphere, the non-condensible constituent is enriched near the antistellar region, and depleted on the dayside. If it is radiatively active such as CO_2 in a pure condensible H_2O atmosphere, the thermal phase curve and high-resolution spectroscopy around the $15\,\mu m$ absorption band should show some unique features. Combined with the study of nondilute atmosphere dominated by an overturning circulation in Chapter 5, the broadband thermal phase curve is a useful tool to discriminate circulation regimes in condensible-rich atmospheres.

In future work, many aspects of the numerical simulations we have done should be investigated in more detail. For example, for the series of simulations in Chapter 4, as the atmosphere becomes more nondilute, the expansion of the Hadley cell, the behavior of midlatitude eddies and the stronger meridional latent heat transport in a thinner atmosphere should be explored. For the nondilute simulation on tidally locked planet in Chapter 5, we will study the structure of the transient eddies – both diagnostically and in terms of barotropic and baroclinic instability theory. We will also incorporate real-gas radiation scheme in Exo-FMS so that some of the results we show in the thesis can be re-examined. More generally, there is considerable work that needs to be done in order to incorporate microphysical effects into the modeling of nondilute atmospheres. In the absence of suitable cloud condensation nuclei, atmospheres may become highly supersaturated before condensate forms, and this is bound to have dynamical effects. Further, the effect of retained condensate in the case where condensate particles remain small can significantly affect buoyancy and inhibit convection. The microphysics governing precipitation and re-evaporation also affect the vertical transport of chemical species in a planetary atmosphere, and therefore affect the vertical structure of atmospheric composition.

Exo-FMS model we develop to study condensible-rich atmospheres in the thesis is flexible and extensible, and can be used for simulations of the 3D climate dynamics of quite general exoplanet atmospheres. This model will be put to further use in future work, and it is our intention to develop it into an open-source platform for planetary circulation modeling. In fact, many climate regimes we discussed in the thesis but have not yet explored are of great interest, such as the abiotic oxygen buildup in H_2O-rich atmospheres, the climate when the condensible substance has a higher molecular weight than that of the non-condensible, whether the CO_2 runaway greenhouse could be delayed by subsaturation to allow the formation of CO_2 ocean, the hydrological cycle in the condensible-rich climate with the cold trap close to the surface by strong shortwave absorption, the tipping point between the overturning circulation and the evaporation-driven circulation in nondilute atmospheres, etc.

APPENDIX A

ENERGY CONSERVATION FOR NONDILUTE SYSTEMS

The following closely follows the derivation given in Trenberth (1997), but with close attention paid to retention of terms that are typically dropped in the dilute limit.

We begin with the momentum and mass continuity equations, and the First Law written in the form given in Eq. 2.8. In altitude (z) coordinates these take the form

$$\rho\frac{\mathrm{d}}{\mathrm{d}t}\boldsymbol{v} = -\boldsymbol{\nabla}p - \rho g\hat{\boldsymbol{z}} \tag{A.1}$$

$$\partial_t\rho + \boldsymbol{\nabla}\cdot\rho\boldsymbol{v} = 0 \tag{A.2}$$

$$\frac{\mathrm{d}}{\mathrm{d}t}(k - \frac{p}{\rho}) + p\frac{\mathrm{d}}{\mathrm{d}t}\frac{1}{\rho} = Q \tag{A.3}$$

where $\mathrm{d}/\mathrm{d}t$ is the material derivative. The density ρ includes both the gas phase and condensed phase mass; mass may exchange between gas and condensed phase, but it is presumed in this derivation that no mass leaves the air parcel in which it was originally found, and that the temperature of the condensate is the same as the temperature of the surrounding gas. The effect of relaxing these assumptions is discussed at the end of this Appendix. Q is the diabatic heating rate per unit mass.

Taking the dot product of the momentum equation (Eq. A.1) with $\boldsymbol{v}$ and using the mass continuity equation (Eq. A.2) yields

$$\partial_t\frac{1}{2}\rho\boldsymbol{v}\cdot\boldsymbol{v} + \boldsymbol{\nabla}\cdot(\frac{1}{2}\rho\boldsymbol{v}\cdot\boldsymbol{v})\boldsymbol{v} = -\boldsymbol{v}\cdot\boldsymbol{\nabla}p - \rho g w \tag{A.4}$$

where w is the vertical velocity. Using $w = \mathrm{d}z/\mathrm{d}t$ together with the continuity equation allows us to write the following expression for the evolution of kinetic plus potential energy

$$\partial_t(\frac{1}{2}\rho\boldsymbol{v}\cdot\boldsymbol{v} + \rho g z) + \boldsymbol{\nabla}\cdot(\frac{1}{2}\rho\boldsymbol{v}\cdot\boldsymbol{v} + \rho g z)\boldsymbol{v} = -\boldsymbol{v}\cdot\boldsymbol{\nabla}p \tag{A.5}$$

Using the mass continuity equation, the right hand side can be rewritten

$$-\boldsymbol{v}\cdot\boldsymbol{\nabla}p = -\boldsymbol{\nabla}\cdot p\boldsymbol{v} + \frac{p}{\rho}\rho\boldsymbol{\nabla}\cdot\boldsymbol{v} = -\boldsymbol{\nabla}\cdot p\boldsymbol{v} - \frac{p}{\rho}\frac{\mathrm{d}\rho}{\mathrm{d}t} \tag{A.6}$$

Now, upon multiplying by ρ the First Law in Eq. A.3 can be rewritten as

$$\partial_t\rho(k-\frac{p}{\rho}) + \boldsymbol{\nabla}\cdot\rho(k-\frac{p}{\rho})\boldsymbol{v} - \frac{p}{\rho}\frac{\mathrm{d}}{\mathrm{d}t}\rho = \rho Q \tag{A.7}$$

which can be combined with Eq. A.5 and A.6 to yield the conservation law

$$\partial_t\rho\mathcal{E} + \boldsymbol{\nabla}\cdot\rho\boldsymbol{\mathcal{F}} = \rho Q \tag{A.8}$$

where the energy density is

$$\mathcal{E} \equiv \frac{1}{2}\boldsymbol{v}\cdot\boldsymbol{v} + gz + (k-\frac{p}{\rho}) \tag{A.9}$$

and the energy flux is

$$\boldsymbol{\mathcal{F}} \equiv \left(\frac{1}{2}\boldsymbol{v}\cdot\boldsymbol{v} + gz + k\right)\boldsymbol{v} \tag{A.10}$$

If the kinetic energy is negligible, the conservation law in the form Eq 2.9 follows upon integrating over an isolated column of the atmosphere.

The above calculation suffices to demonstrate moist enthalpy conservation in the context of the convective adjustment protocol employed in the text, in which a layer is first mixed with condensate retained, followed by a separate step in which condensate is removed from the column, taking its enthalpy and potential energy with it. In a real atmosphere, condensate would be redistributed amongst air parcels continuously, with some particles eventually reaching the bottom where they are removed. A formal treatment of conservation in this situation would be very complex, given that each condensate particle has its own history-dependent velocity and each air parcel retains a mix of condensate particles each with their own characteristics. However, a simple physical argument suffices to justify conservation in the general case. Imagine a situation in which a single condensate droplet moves from one air parcel to an adjoining one. In that case, it simply carries its own enthalpy with it, so the enthalpy removed from one air parcel is added to the other, and similarly, potential and kinetic energy is moved, with some of the mechanical energy left behind in the source air parcel if there has been drag against the particle, and some interchange between potential and kinetic energy if the particle has changed altitude. Subsequent transformations of the condensate without leaving the destination parcel are within the scope of the preceding derivation. Since the energy transport for each droplet occurs independently of the others, if conservation applies for displacement of an individual droplet, it will also apply for an ensemble of droplets.

APPENDIX B

MODIFICATIONS OF THE FINITE-VOLUME DYNAMICAL CORE FOR NON-DILUTE ATMOSPHERES

The finite-volume dynamical core is able to simulate 3D atmospheric circulations while conserving the mass of the background component and other tracers to a certain extent. To implement an hydrological cycle in the model, we only need to add in an energy-conserving moist convection scheme, and take into account the density effect of the condensible component.

B.1 Explicit treatment of the mass loss effect as the condensate falls

Our moist convective adjustment scheme requires that once the condensate forms it falls to the ground immediately. In each time step, this scheme is repeated five times to make sure the final thermal structure follows the moist adiabat. The pressure thicknesses, air temperature and humidity profile are all changed by the removal of the condensate. We do not modify the continuity equation in the dynamical core, but deal with this mass loss effect explicitly:

1. When the condensate in one air layer falls, the pressure in layers below this layer will decrease hydrostatically. Meanwhile the temperature in these layer drops adiabatically and the concentration of the condensible component stays the same. This has already been utilized in the 1D single column model.

2. The horizontal wind velocities in these layers also stay the same as the humidity. In fact, for these layers there are also momentum and kinetic energy loss that is carried by the falling condensate due to this mass loss. But the kinetic energy is ignored in the Exo-FMS because it is usually small compared to the potential energy.

B.2 Surface energy budget

As the mass of the slab ocean (M_s) changes with surface precipitation minus evaporation ($P - E$), the energy budget at the surface should be

$$c_{pl}\frac{\mathrm{d}(M_sT_s)}{\mathrm{d}t} = c_{pl}(T_c \cdot P - T_s \cdot E) + F'_{other}, \quad \text{and} \quad \frac{\mathrm{d}M_s}{\mathrm{d}t} = P - E$$

Here F'_{other} includes the surface radiative fluxes, surface sensible and latent heat, and the kinetic energy and potential energy of the precipitation; T_s and T_c are temperatures of the slab ocean and the falling condensate, respectively. Then the changing rate of the surface temperature is slightly different from that of the thermal energy of the slab ocean since its mass varies:

$$c_{pl}M_s\frac{\mathrm{d}T_s}{\mathrm{d}t} = c_{pl}(T_c - T_s) \cdot P + F'_{other} \tag{B.1}$$

Eq.(B.1) points out two facts associated with surface evaporation and precipitation:

1. The slab ocean loses both mass and energy through evaporation, but this mass loss should not change the ocean temperature.

2. When the cold raindrops mix with the ocean water, the ocean should cool down, which is represented by the term $c_{pl}(T_c - T_s) \cdot P$.

There is a serious problem if allowing $P-E$ to change the slab ocean depth in 3D models. At some grid boxes in the model, $(P - E)$ may be always negative forced by atmospheric circulation. So after long-time of integration, these grid boxes will lose the slab ocean surface entirely.

To avoid this situation, we implement a simple energy correction scheme that resembles the ocean circulation. First, the energy correction scheme evens out the variation of the slab ocean depth without affecting T_s. Then to conserve energy of the slab ocean, a temperature correction term should be applied:

$$\Delta T_s = \overline{T_s(\mathbf{x}) \frac{(P-E)_{\mathbf{x}} - \overline{P-E}}{\overline{M_s}}}$$

where the overline operation denotes global horizontal average. The horizontal variation of $P - E$ is several orders of magnitude lower than the mass of the slab ocean, and so is the temperature correction term compared to T_s. By doing this correction, the global mean mixed layer depth varies with global mean $(P - E)$ and conserves energy, but the mixed layer depth stays constant horizontally.

B.3 Thermodynamic equation

The dynamical core conserves virtual potential temperature in the dilute limit

$$\theta_v(p) = T(p)\ p^{-\kappa}\ (1 + 0.608q), \qquad \kappa = 2/7$$

where q is the mass fraction of the condensible gas. The ratio 0.608 stems from the molecular weight difference between the condensible and non-condensible gases (i.e., water vapor and the N_2-O_2 mixture in the dynamical core).

The conserved quantity during dry adiabatic process is slightly different in condensible-rich atmosphere. If we start from the First Law of Thermodynamics,

$$\delta Q = \bar{c_p}\mathrm{d}T - \frac{1}{\bar{\rho}}\mathrm{d}p$$

where for water convection in the N_2-O_2 atmosphere,

$$\bar{c_p} = c_{pd}(1-q) + c_{pv}q = c_{pd}[1 + (c_{pv}/c_{pd} - 1)q] = c_{pd}(1 + 0.8396q)$$

$$\bar{\rho} = \frac{p}{\bar{R}T}, \qquad \bar{R} = R_d(1-q) + R_v q = R_d[1 + (R_v/R_d - 1)q] = R_d(1 + 0.608q)$$

then the conserved quantity for adiabatic flow is

$$\theta'(p) = Tp^{-\kappa'} = const., \qquad \kappa' = \frac{R_d(1-q)+R_v q}{c_{pd}(1-q)+c_{pv}q} = \frac{R_d}{c_{pd}}\frac{1+0.608q}{1+0.8396q}$$

The exponent κ' ranges from 1κ to 0.87κ. In the dilute limit, the conserved variable reduces to the conventional dry potential temperature θ_d.

B.4 Computing the geopotential

When calculating the horizontal gradient of geopotential, the dynamical core uses p^κ as the vertical coordinate:

$$\delta\phi = -\frac{\delta p}{\rho} = -c_{pd}\theta_v \ \delta(p^\kappa) = -A\delta(p^\kappa)$$

Note that the variable A is the conserved quantity that is used in the thermodynamic equation of the dynamical core. In such a way, the finite-volume dynamical core avoids redundant floating point operations and then is optimized for speed.

However, in the condensible-rich atmosphere, the above equation has a serious problem. Although it has taken the density effect of the condensible component on the specific gas constant $\bar{R}$ into account, it still treats the dry potential temperature θ_d as a conserved variable. As noted in Section B.3, the exponent κ' now depends on the concentration of condensible component and therefore varies with height. Using the generalized potential temperature θ' defined above, the geopotential should be calculated as

$$\begin{aligned}
\delta\phi &= -\frac{\delta p}{\bar{\rho}} = -\frac{\bar{R}T}{p}\delta p \\
&= -R_d(1+0.608q)\ \theta'\ p^{\kappa'}\frac{\delta p}{p} \\
&= -R_d(1+0.608q)\ \theta'\ \frac{1}{\kappa'}\delta(p^{\kappa'}) \\
&= -c_{pd}(1+0.8396q)\ \theta'\ \delta(p^{\kappa'}) \\
&= B\ \delta(p^{\kappa'})
\end{aligned}$$

and B is the modified conserved quantity that is used in the thermodynamic equation of Exo-FMS.

B.5 The total energy conserving mapping algorithm

The vertical discretization of the finite-volume dynamical core is Lagrangian. The Lagrangian surfaces that bound the finite-volume will deform as air flows. Therefore, an accurate and conservative algorithm for mapping the deformed Lagrangian coordinate back to a fixed reference Eulerian coordinate is required. In the mapping procedure, the piece-wise continuous vertical subgrid profiles are constructed and are used for obtaining the layer mean values in the Eulerian coordinate system while conserving the mass $(\delta p, q)$, wind velocity (u, v) and the total energy (Γ).

The layer mean total energy should be computed considering the density effect of the condensible component

$$\Gamma_k = c_{pd}(1+0.8396q)T_k + \frac{1}{\delta p}\delta(p\phi) + K_k$$

Then the layer mean temperature T_k in the Eulerian coordinate is retrieved from the reconstructed total energy Γ_k and u, v, q.

$$T_k = \frac{\Gamma_k - K_k - \phi_{k+1/2}}{c_p'\left[1 - \kappa' p_{k-1/2}\frac{\ln p_{k+1/2} - \ln p_{k-1/2}}{p_{k+1/2} - p_{k-1/2}}\right]}$$

This equation is similar to the one used in the original dynamical core. The only difference is that it takes the density effect of water vapor in c_p and κ into account.

B.6 Vertical differencing

The original dynamical core chooses hybrid vertical differencing. At very low surface pressure, the air pressure levels may not vary monotonically. To avoid this situation, we replace it with a pure "sigma" coordinate:

$$\sigma = p_s^{-(0.1\tilde{z}+0.9\tilde{z}^2)}, \qquad 0 \leq \tilde{z} < 1$$

It guarantees that the topmost pressure level is approximately 1 Pa, and it is high enough to resolve the radiative and convective process near the tropopause in this work.

REFERENCES

Betts, A. K. (1986). A new convective adjustment scheme. Part I: Observational and theoretical basis. *Quarterly Journal of the Royal Meteorological Society*, 112(473):677–691.

Betts, A. K. and Miller, M. J. (1986). A new convective adjustment scheme. Part II: Single column tests using GATE wave, BOMEX, ATEX and arctic air-mass data sets. *Quarterly Journal of the Royal Meteorological Society*, 112(473):693–709.

Castan, T. and Menou, K. (2011). Atmospheres of Hot Super-Earths. *ApJ*, 743(2):L36.

Catling, D. (2014). 6.7 - the great oxidation event transition. In Holland, H. D. and Turekian, K. K., editors, *Treatise on Geochemistry (Second Edition)*, pages 177 – 195. Elsevier, Oxford, second edition.

Catling, D. C., Glein, C. R., Zahnle, K. J., and McKay, C. P. (2005). Why O_2 Is Required by Complex Life on Habitable Planets and the Concept of Planetary "Oxygenation Time". *Astrobiology*, 5:415–438.

Charnay, B., Forget, F., Tobie, G., Sotin, C., and Wordsworth, R. (2014). Titan's past and future: 3D modeling of a pure nitrogen atmosphere and geological implications. *Icarus*, 241:269–279.

Claire, M. W., Catling, D. C., and Zahnle, K. J. (2006). Biogeochemical modelling of the rise in atmospheric oxygen. *Geobiology*, 4(4):239–269.

Colaprete, A. and Toon, O. B. (2003). Carbon dioxide clouds in an early dense Martian atmosphere. *Journal of Geophysical Research: Planets*, 108(E4). 5025.

Ding, F. and Pierrehumbert, R. T. (2016). Convection in condensible-rich atmospheres. *The Astrophysical Journal*, 822(1):24.

Emanuel, K. A. (1994). *Atmospheric Convection*. Oxford University Press.

Forget, F., Hourdin, F., and Talagrand, O. (1998). CO_2 Snowfall on Mars: Simulation with a General Circulation Model. *Icarus*, 131(2):302–316.

Forget, F. and Pierrehumbert, R. T. (1997). Warming Early Mars with Carbon Dioxide Clouds That Scatter Infrared Radiation. *Science*, 278(5341):1273–1276.

Forget, F., Wordsworth, R., Millour, E., Madeleine, J.-B., Kerber, L., Leconte, J., Marcq, E., and Haberle, R. (2013). 3D modelling of the early martian climate under a denser CO_2 atmosphere: Temperatures and CO_2 ice clouds. *Icarus*, 222(1):81–99.

Frierson, D. M. W. (2007). The Dynamics of Idealized Convection Schemes and Their Effect on the Zonally Averaged Tropical Circulation. *J. Atmos. Sci.*, 64(6):1959–1976.

Goldblatt, C. (2015). Habitability of Waterworlds: Runaway Greenhouses, Atmospheric Expansion, and Multiple Climate States of Pure Water Atmospheres. *Astrobiology*, 15(5):362–370.

Goldblatt, C., Claire, M. W., Lenton, T. M., Matthews, A. J., Watson, A. J., and Zahnle, K. J. (2009). Nitrogen-enhanced greenhouse warming on early Earth. *Nature Geosci*, 2(12):891–896.

Guillot, T. (1995). Condensation of methane, ammonia, and water and the inhibition of convection in giant planets. *Science*, 269(5231):1697–1699.

Haqq-Misra, J., Lee, S., and Frierson, D. M. W. (2011). Tropopause structure and the role of eddies. *Journal of the Atmospheric Sciences*, 68(12):2930–2944.

Harman, C. E., Schwieterman, E. W., Schottelkotte, J. C., and Kasting, J. F. (2015). Abiotic O_2 Levels on Planets around F, G, K, and M Stars: Possible False Positives for Life? *The Astrophysical Journal*, 812(2):137.

Hir, G. L., Donnadieu, Y., Goddris, Y., Pierrehumbert, R. T., Halverson, G. P., Macouin, M., Ndlec, A., and Ramstein, G. (2009). The snowball earth aftermath: Exploring the limits of continental weathering processes. *Earth and Planetary Science Letters*, 277(3):453 – 463.

Holton, J. R., Haynes, P. H., McIntyre, M. E., Douglass, A. R., Rood, R. B., and Pfister, L. (1995). Stratosphere-troposphere exchange. *Reviews of Geophysics*, 33(4):403–439.

Ingersoll, A. P. (1969). The Runaway Greenhouse: A History of Water on Venus. *Journal of the Atmospheric Sciences*, 26(6):1191–1198.

Ingersoll, A. P. (1990). Dynamics of Triton's atmosphere. *Nature*, 344(6264):315–317.

Ingersoll, A. P., Summers, M. E., and Schlipf, S. G. (1985). Supersonic meteorology of Io: Sublimation-driven flow of SO_2. *Icarus*, 64(3):375–390.

Ishiwatari, M., Takehiro, S.-i., Nakajima, K., and Hayashi, Y.-Y. (2002). A Numerical Study on Appearance of the Runaway Greenhouse State of a Three-Dimensional Gray Atmosphere. *Journal of the Atmospheric Sciences*, 59(22):3223–3238.

Kasting, J. and Ackerman, T. (1986). Climatic consequences of very high carbon dioxide levels in the earth's early atmosphere. *Science*, 234(4782):1383–1385.

Kasting, J. F. (1988). Runaway and moist greenhouse atmospheres and the evolution of Earth and Venus. *Icarus*, 74(3):472–494.

Kasting, J. F. (1991). CO_2 condensation and the climate of early Mars. *Icarus*, 94(1):1 – 13.

Kasting, J. F., Chen, H., and Kopparapu, R. K. (2015). Stratospheric temperatures and water loss from moist greenhouse atmospheres of earth-like planets. *The Astrophysical Journal Letters*, 813(1):L3.

Kasting, J. F., Whitmire, D. P., and Reynolds, R. T. (1993). Habitable Zones around Main Sequence Stars. *Icarus*, 101(1):108–128.

Koll, D. D. B. and Abbot, D. S. (2015). Deciphering thermal phase curves of dry, tidally locked terrestrial planets. *The Astrophysical Journal*, 802(1):21.

Koll, D. D. B. and Abbot, D. S. (2016). Temperature structure and atmospheric circulation of dry tidally locked rocky exoplanets. *The Astrophysical Journal*, 825(2):99.

Kopparapu, R. K., Ramirez, R., Kasting, J. F., Eymet, V., Robinson, T. D., Mahadevan, S., Terrien, R. C., Domagal-Goldman, S., Meadows, V., and Deshpande, R. (2013). Habitable Zones around Main-sequence Stars: New Estimates. *ApJ*, 765(2):131.

Leconte, J., Forget, F., Charnay, B., Wordsworth, R., and Pottier, A. (2013). Increased insolation threshold for runaway greenhouse processes on Earth-like planets. *Nature*, 504(7479):268–271.

Li, C. and Ingersoll, A. P. (2015). Moist convection in hydrogen atmospheres and the frequency of Saturn's giant storms. *Nature Geoscience*, 8:398–403.

Lin, S.-J. (2004). A Vertically Lagrangian Finite-Volume Dynamical Core for Global Models. *Mon. Wea. Rev.*, 132(10):2293–2307.

Luger, R. and Barnes, R. (2015). Extreme Water Loss and Abiotic O_2 Buildup on Planets Throughout the Habitable Zones of M Dwarfs. *Astrobiology*, 15:119–143.

Manabe, S., Smagorinsky, J., and Strickler, R. F. (1965). Simulated climatology of a general circulation model with a hydrologic cycle [1]. *Monthly Weather Review*, 93(12):769–798.

Manabe, S. and Strickler, R. F. (1964). Thermal Equilibrium of the Atmosphere with a Convective Adjustment. *Journal of the Atmospheric Sciences*, 21(4):361–385.

Manabe, S. and Wetherald, R. T. (1967). Thermal Equilibrium of the Atmosphere with a Given Distribution of Relative Humidity. *Journal of the Atmospheric Sciences*, 24(3):241–259.

Merlis, T. M. and Schneider, T. (2010). Atmospheric Dynamics of Earth-Like Tidally Locked Aquaplanets. *J. Adv. Model. Earth Syst.*, 2(4):13.

Nakajima, S., Hayashi, Y.-Y., and Abe, Y. (1992). A Study on the "Runaway Greenhouse Effect" with a One-Dimensional Radiative-Convective Equilibrium Model. *Journal of the Atmospheric Sciences*, 49(23):2256–2266.

O'Gorman, P. A. and Schneider, T. (2008). The Hydrological Cycle over a Wide Range of Climates Simulated with an Idealized GCM. *J. Climate*, 21(15):3815–3832.

Parmentier, V., Fortney, J. J., Showman, A. P., Morley, C., and Marley, M. S. (2016). Transitions in the Cloud Composition of Hot Jupiters. *The Astrophysical Journal*, 828(1):22.

Peixoto, J. P. and Oort, A. H. (1992). *Physics of Climate*. American Institute of Physics.

Perez-Becker, D. and Showman, A. P. (2013). Atmospheric Heat Redistribution on Hot Jupiters. *The Astrophysical Journal*, 776(2):134.

Pierrehumbert, R., Brogniez, H., and Roca, R. (2007). On the relative humidity of the atmosphere. In Schneider, T. and Sobel, A. H., editors, *The Global Circulation of the Atmosphere*, pages 143–185. Princeton University Press.

Pierrehumbert, R. and Gaidos, E. (2011). Hydrogen greenhouse planets beyond the habitable zone. *The Astrophysical Journal Letters*, 734(1):L13.

Pierrehumbert, R. T. (2002). The hydrologic cycle in deep-time climate problems. *Nature*, 419:191–198.

Pierrehumbert, R. T. (2010). *Principles of Planetary Climate*. Cambridge University Press. Google-Books-ID: bO_U8f5pVR8C.

Pierrehumbert, R. T. (2011). A Palette of Climates for Gliese 581g. *The Astrophysical Journal Letters*, 726(1):L8.

Pierrehumbert, R. T. and Ding, F. (2016). Dynamics of atmospheres with a non-dilute condensible component. *Proceedings of the Royal Society A: Mathematical, Physical and Engineering Science*, 472(2190):20160107.

Pierrehumbert, R. T. and Roca, R. (1998). Evidence for control of Atlantic subtropical humidity by large scale advection. *Geophysical Research Letters*, 25(24):4537–4540.

Renn, N. O., Stone, P. H., and Emanuel, K. A. (1994). Radiative-convective model with an explicit hydrologic cycle: 2. Sensitivity to large changes in solar forcing. *Journal of Geophysical Research: Atmospheres*, 99(D8):17001–17020.

Som, S. M., Catling, D. C., Harnmeijer, J. P., Polivka, P. M., and Buick, R. (2012). Air density 2.7 billion years ago limited to less than twice modern levels by fossil raindrop imprints. *Nature*, 484(7394):359–362.

Sprague, A. L., Boynton, W. V., Kerry, K. E., Janes, D. M., Kelly, N. J., Crombie, M. K., Nelli, S. M., Murphy, J. R., Reedy, R. C., and Metzger, A. E. (2007). Mars' atmospheric argon: Tracer for understanding martian atmospheric circulation and dynamics. *Journal of Geophysical Research: Planets*, 112(E3). E03S02.

Tian, F., France, K., Linsky, J. L., Mauas, P. J., and Vieytes, M. C. (2014). High stellar FUV/NUV ratio and oxygen contents in the atmospheres of potentially habitable planets. *Earth and Planetary Science Letters*, 385:22 – 27.

Trafton, L. (1984). Large seasonal variations in Triton's atmosphere. *Icarus*, 58(2):312–324.

Trafton, L. and Stern, S. A. (1983). On the global distribution of Pluto's atmosphere. *The Astrophysical Journal*, 267:872.

Trenberth, K. E. (1997). Using atmospheric budgets as a constraint on surface fluxes. *Journal of Climate*, 10(11):2796–2809.

Vallis, G. K. (2006). *Atmospheric and Oceanic Fluid Dynamics: Fundamentals and Large-scale Circulation*. Cambridge University Press.

Williams, I. N., Pierrehumbert, R. T., and Huber, M. (2009). Global warming, convective threshold and false thermostats. *Geophysical Research Letters*, 36(21). L21805.

Wolf, E. T. (2017). Assessing the Habitability of the TRAPPIST-1 System Using a 3D Climate Model. *The Astrophysical Journal Letters*, 839(1):L1.

Wolf, E. T. and Toon, O. B. (2015). The evolution of habitable climates under the brightening Sun. *Journal of Geophysical Research: Atmospheres*, 120(12):5775–5794. 2015JD023302.

Wordsworth, R. and Pierrehumbert, R. (2013a). Hydrogen-Nitrogen Greenhouse Warming in Earth's Early Atmosphere. *Science*, 339(6115):64–67.

Wordsworth, R. and Pierrehumbert, R. (2014). Abiotic oxygen-dominated atmospheres on terrestrial habitable zone planets. *The Astrophysical Journal Letters*, 785(2):L20.

Wordsworth, R. D., Forget, F., Selsis, F., Madeleine, J.-B., Millour, E., and Eymet, V. (2010). Is Gliese 581d habitable? Some constraints from radiative-convective climate modeling. *Astronomy & Astrophysics*, 522:A22.

Wordsworth, R. D., Forget, F., Selsis, F., Millour, E., Charnay, B., and Madeleine, J.-B. (2011). Gliese 581d is the first discovered terrestrial-mass exoplanet in the habitable zone. *The Astrophysical Journal Letters*, 733(2):L48.

Wordsworth, R. D. and Pierrehumbert, R. T. (2013b). Water Loss from Terrestrial Planets with CO_2-rich Atmospheres. *ApJ*, 778(2):154.

Yang, J. and Abbot, D. S. (2014). A low-order model of water vapor, clouds, and thermal emission for tidally locked terrestrial planets. *The Astrophysical Journal*, 784(2):155.

Yang, J., Cowan, N. B., and Abbot, D. S. (2013). Stabilizing Cloud Feedback Dramatically Expands the Habitable Zone of Tidally Locked Planets. *ApJ*, 771(2):L45.

Zalucha, A. M. (2016). An atmospheric general circulation model for Pluto with predictions for New Horizons temperature profiles. *Monthly Notices of the Royal Astronomical Society*, 459(1):902–923.